BEILSTEIN JOURNAL OF NANOTECHNOLOGY

Advanced functional nanomaterials for water remediation applications

Edited by Jagpreet Singh, Valeria De Matteis, Mikhael Bechelany and Akansha Mehta

Generated on 12 November 2026, 11:43

Imprint

Beilstein Journal of Nanotechnology
www.bjnano.org
ISSN 2190-4286
Email: journals-support@beilstein-institut.de

The *Beilstein Journal of Nanotechnology* is published by the Beilstein-Institut zur Förderung der Chemischen Wissenschaften.

Beilstein-Institut zur Förderung der Chemischen Wissenschaften
Trakehner Straße 7–9
60487 Frankfurt am Main
Germany
www.beilstein-institut.de

The copyright to this document as a whole, which is published in the *Beilstein Journal of Nanotechnology*, is held by the Beilstein-Institut zur Förderung der Chemischen Wissenschaften. The copyright to the individual articles in this document is held by the respective authors, subject to a Creative Commons Attribution license.

BEILSTEIN JOURNAL OF NANOTECHNOLOGY

Green synthesis of biomass-derived carbon quantum dots for photocatalytic degradation of methylene blue

Dalia Chávez-García*[1], Mario Guzman[1], Viridiana Sanchez[1] and Rubén D. Cadena-Nava[2]

Full Research Paper

Open Access

Address:
[1]Centro de Enseñanza Técnica y Superior (CETYS), Camino Microondas Trinidad KM 1, Las Palmas 3era. Sección., 22860, Ensenada, Baja California, Mexico and [2]Centro de Nanociencias y Nanotecnología (CNYN), Ensenada, Baja California, Mexico

Email:
Dalia Chávez-García* - dalia.chavez@cetys.mx.

* Corresponding author

Keywords:
biomass; carbon dots; catalysis; methylene blue; photoluminiscence

Beilstein J. Nanotechnol. **2024,** *15,* 755–766.
https://doi.org/10.3762/bjnano.15.63

Received: 20 February 2024
Accepted: 13 June 2024
Published: 25 June 2024

This article is part of the thematic issue "Advanced functional nanomaterials for water remediation applications".

Guest Editor: J. Singh

© 2024 Chávez-García et al.; licensee Beilstein-Institut.
License and terms: see end of document.

Abstract

Water pollution, significantly influenced by the discharge of synthetic dyes from industries, such as textiles, poses a persistent global threat to human health. Among these dyes, methylene blue, particularly prevalent in the textile sector, exacerbates this issue. This study introduces an innovative approach to mitigate water pollution through the synthesis of nanomaterials using biomass-derived carbon quantum dots (CQDs) from grape pomace and watermelon peel. Utilizing the hydrothermal method at temperatures between 80 and 160 °C over periods ranging from 1 to 24 h, CQDs were successfully synthesized. A comprehensive characterization of the CQDs was performed using UV–visible spectroscopy, Fourier-transform infrared spectroscopy, dynamic light scattering, Raman spectroscopy, and luminescence spectroscopy, confirming their high quality. The photocatalytic activity of the CQDs in degrading methylene blue was evaluated under both sunlight and incandescent light irradiation, with measurements taken at 20 min intervals over a 2 h period. The CQDs, with sizes ranging from 1–10 nm, demonstrated notable optical properties, including upconversion and down-conversion luminescence. The results revealed effective photocatalytic degradation of methylene blue under sunlight, highlighting the potential for scalable production of these cost-effective catalytic nanomaterials for synthetic dye degradation.

Introduction

The textile industry is known for its high consumption of water, energy, and chemical reagents. For example, manufacturing a pair of indigo-dyed pants requires at least 42 L of water, plus approximately 21 L each time they are washed at home. To ensure product quality, textile dyes are designed to be resistant to light, detergents, and cleaning products, making them diffi-

cult to remove. When these dyes are released into water bodies, they cause pollution problems such as chemical oxygen demand, toxicity, and reduced light penetration, which affects aquatic life. As a result, the textile industry is a major contributor to water pollution [1,2].

To address this issue, the textile industry must adopt more sustainable practices in water and energy use, develop environmentally friendly dyes, and implement wastewater treatment processes. Conventional wastewater treatment techniques are often ineffective against resistant dyes, necessitating more advanced and sustainable technologies [3-7]. Embracing more sustainable practices and developing eco-friendly technologies are key to achieving a balance between textile production and environmental preservation [8-14]. Researchers are exploring innovative approaches, such as advanced oxidation processes, nanotechnology-based methods, and biological treatment systems, which show promise in effectively removing pollutants from wastewater [14-16].

In this research, we focus on the synthesis of carbon quantum dots (CQDs) through a hydrothermal method using biomass from watermelon peels and grape pomace. This method is chosen for its ease of production, low cost, and scalability. We aim to evaluate the potential of CQDs as catalysts in the photocatalytic degradation of methylene blue (MB) dye in industrial wastewater.

Photocatalysis is an environmentally friendly water purification method that uses light-activated catalysts to destroy contaminants, offering an advantage over traditional methods that merely transfer contaminants between phases [17-19]. While some studies on CQDs involve costly equipment, our approach uses green synthesis with biomass, aligning with eco-friendly principles [19-21].

Carbon quantum dots are valued for their easy synthesis, good solubility, photostability, nontoxic properties, and versatile applications. They can be synthesized using various methods, including top-down approaches such as arc discharge and laser ablation, and bottom-up methods such as hydrothermal and microwave synthesis [7,22] Biomass sources for CQD synthesis include eggshells, papaya peel, and lemon peel [23-39].

Applications of CQDs range from sensing and cell imaging to drug delivery, photocatalysis, and energy conversion [26-29]. In this study, biomass from watermelon shell and grape pomace waste is used as the carbon source. The hydrothermal method employing urea, nitric acid, and water is utilized. Samples synthesized with nitric acid demonstrated superior catalytic activity in MB degradation.

Carbon quantum dots typically exhibit luminescence properties, with emission peaks in the blue region between 450 and 500 nm varying based on the solvent used [26-28]. In our research, CQDs showed upconversion emission when excited at 900 nm and down-conversion emission in the blue region. The photocatalytic activity of CQDs, under sunlight irradiation, in MB degradation has been confirmed by various studies [32-38].

In this research, samples synthesized with nitric acid exhibited the best catalytic activity in MB degradation, while those prepared with water as a solvent did not show significant catalytic activity. The samples were also characterized using UV–visible spectra, Fourier-transform infrared spectroscopy (FTIR), Raman spectroscopy, dynamic light scattering (DLS), and photoluminescence spectroscopy (PL). The utilization of biomass as a carbon source offers great opportunities due to its abundance in nature and the wide range of sources available, which exhibit good luminescent and catalytic properties.

Focusing on the hydrothermal synthesis method using biomass-derived precursors, this research aims to develop a more sustainable and cost-effective approach for producing CQDs as catalysts in the photocatalysis process. Utilizing watermelon peels and grape pomace as raw materials contributes to waste valorization and promotes a circular economy concept. The ultimate goal is to provide a greener and more efficient solution for wastewater treatment in the textile industry, reducing environmental impact and conserving clean water resources. This research represents a significant step towards addressing water pollution caused by the textile industry, and highlights the potential of nanotechnology in developing sustainable solutions.

Experimental

Materials/material synthesis

The synthesis of CQDs involved the utilization of biomass-derived precursors. The method employed was based on the hydrothermal approach reported by Yuan et al. [40] with modifications in terms of precursor selection and chemical conditions.

Two organic materials, watermelon rind and grape pomace, were used as the precursors and were obtained from waste generated by the local wine industry. Initially, small pieces of the biomass were cut and placed on metal trays, followed by drying in a convection oven at 60 °C. Subsequently, the dried precursors were individually crushed in a mortar until they formed a fine powder. Additionally, four different synthesis schemes were proposed, involving modifications in the chemical conditions of the precursor solution.

In a typical synthesis, 50 mL of deionized water was mixed with 0.5 g of biomass precursor powder (dispersion A) and stirred for 10 min. Then, 1.0 g of urea (hydrolizing agent under hydrothermal conditions) was diluted in 50 mL of deionized water to form a homogeneous solution (solution B) and then mixed with dispersion A. The final mixture was stirred for an additional 10 min. Subsequently, the mixture was transferred to a Teflon-lined stainless steel autoclave, which was sealed under pressure using a manual press. The autoclave was then placed in a convection oven and maintained at 100°C for 2 h. After the specified time had elapsed, the autoclave was allowed to cool and the solution was retrieved. After the synthesis, the solutions were filtered through a Büchner funnel equipped with a 200 nm nylon membrane (Whatman) [30] and centrifuged at 15000 rpm for 20 min.

The process previously described was repeated modifying the chemical condition by varying solution B as follows: i) 1.0 g of urea in 50 mL of deionized water (samples M1 and M5); ii) 1.0 g of urea and 5.0 mL of nitric acid (69% v/v) in 50 mL of deionized water (samples M2 and M6); iii) 2.5 mL of nitric acid (69% v/v) in 50 mL of deionized water (samples M3 and M7); and iv) 50 mL of deionized water (M4 and M8). Samples M1, M2, M3, and M4 were prepared using grape pomace peel as the biomass precursor, and samples M5, M6, M7, and M8 were prepared using watermelon peel as the biomass precursor. This information is sumarized in Table 1.

Characterizations

To determine the optoelectronic characteristics of the synthesized CQDs, UV–vis absorption spectra were measured using a Thermo Scientific Evolution 220 spectrophotometer. The CQDs were dissolved in deionized water at a ratio of 1:10 (0.3 mg of CQDs per mL) and the measurements were taken in the range of 200–800 nm. A 1 cm path length quartz cell was used for the measurements, and deionized water was used as the blank in the measurement to account for background signals. Fourier-transform infrared spectra were measured on a Spectrum Two FT-IR/Sp 10 S/W spectrometer (USA) with a $LiTaO_3$ type detector, the wavelength used ranged from 450 to 4000 cm^{-1}. The size distribution of the synthesized CQDs was determined via DLS, which relies on the measurement of the hydrodynamic radius of the particles. The CQDs were analyzed via a Malvern NanoSizer ZP instrument. The samples were diluted in deionized water to prevent signal saturation. Multiple measurements (at least three) were performed for each sample to ensure reliable and accurate measurements. A quartz cell with a 1 cm path length was used for the DLS measurements using a Malvern Zeta-sizer equipment model 7.2. Raman spectroscopy for all samples was performed in a Horiba Jobin Yvon Xplora Raman microscope using a 532 nm laser excitation as the power source. The photoluminescence spectra of the samples were obtained with an Agilent Cary Eclipse fluorescence spectrophotometer. It consists of two Czerny–Turner slits (excitation and emission) with a double monochromator and a continuous emission xenon light source (190–900 nm). All the samples were dispersed in deionized water and analyzed with an excitation wavelength of 350 and 900 nm in aqueous medium.

Photocatalytic evaluation

The photocatalytic activity of the synthesized CQDs was studied for the photodegradation of MB in aqueous media. The tests were separately conducted using sunlight and incandescent light (tungsten halogen lamp, 40 W). Previous to exposure, the reaction mixture was kept under vigorous stirring in the absence of light for 20 min to discard any adsorption effect. On the other hand, the pH value of the reaction mixture was kept constant during the test (pH 7). To initiate the catalytic process, each CQD sample was individually applied to the degradation of the MB dye. The UV–vis absorption spectrum of the dye was monitored using a spectrophotometer (Thermo Scientific Evolution model 220) with a 1 cm path length quartz cell.

To evaluate the photocatalytic activity of the CQDs, a suspension containing CQDs and MB (10 ppm initial concentration of MB) was placed in a baker under constant stirring. Before initi-

Table 1: Synthesis conditions for CQDs.

Sample	Carbon source	Chemical treatment	Hydrothermal conditions
M1	watermelon peel	urea	90 °C/2 h
M2	watermelon peel	nitric acid	90 °C/2 h
M3	watermelon peel	nitric acid + urea	90 °C/2 h
M4	watermelon peel	pure water	90 °C/2 h
M5	grape pomace	urea	90 °C/2 h
M6	grape pomace	nitric acid	90 °C/2 h
M7	grape pomace	nitric acid + urea	90 °C/2 h
M8	grape pomace	pure water	90 °C/2 h

ating the light irradiation, the suspension was stirred for 20 min at 400 rpm in a dark environment to ensure proper dispersion of the CQDs in aqueous media and the adsorption of the dye on the CQD surface. After the stirring period of 20 min, the solution absorbance was measured using a spectrophotometer in the wavelength range of 250–800 nm. This measurement marked the start of the photodegradation reaction under light radiation. In the case of tests conducted with incandescent light, a lamp was used as the light source, placed approximately 10 cm away from the solution, and the reaction was allowed to proceed for 100 min.

During the degradation tests, both sunlight and incandescent light were used, and the solution was continuously agitated. The absorbance of the solution was measured at 20 min intervals to monitor the progress of the degradation reaction. All samples were evaluated under both light sources.

Results and Discussion

UV–vis spectroscopy

UV–vis spectroscopy was used to analyze the optoelectronic properties of eight CQD samples synthesized by the hydrothermal method. All samples were diluted in deionized water to adjust the CQDs concentration to 0.3 mg/mL. Figure 1 shows the CQDs synthesized from grape pomace peel (Figure 1a) and watermelon peel (Figure 1b). It is observed that for each of the samples, its maximum absorption peak is approximately at 350 nm, which corresponds to n–π^* transitions present in unsaturated compounds with heteroatoms (carbonyl groups). An absorbance tail is also noticed in the visible range [31,32]. The samples M6 and M7 (Figure 1b and Figure 1c) present a relatively symmetrical band also centered at 350 nm with a higher intensity for sample M6. Both samples were prepared using an oxidation process with nitric acid prior to the hydrothermal treatment to break the structure of the carbohydrate used. On

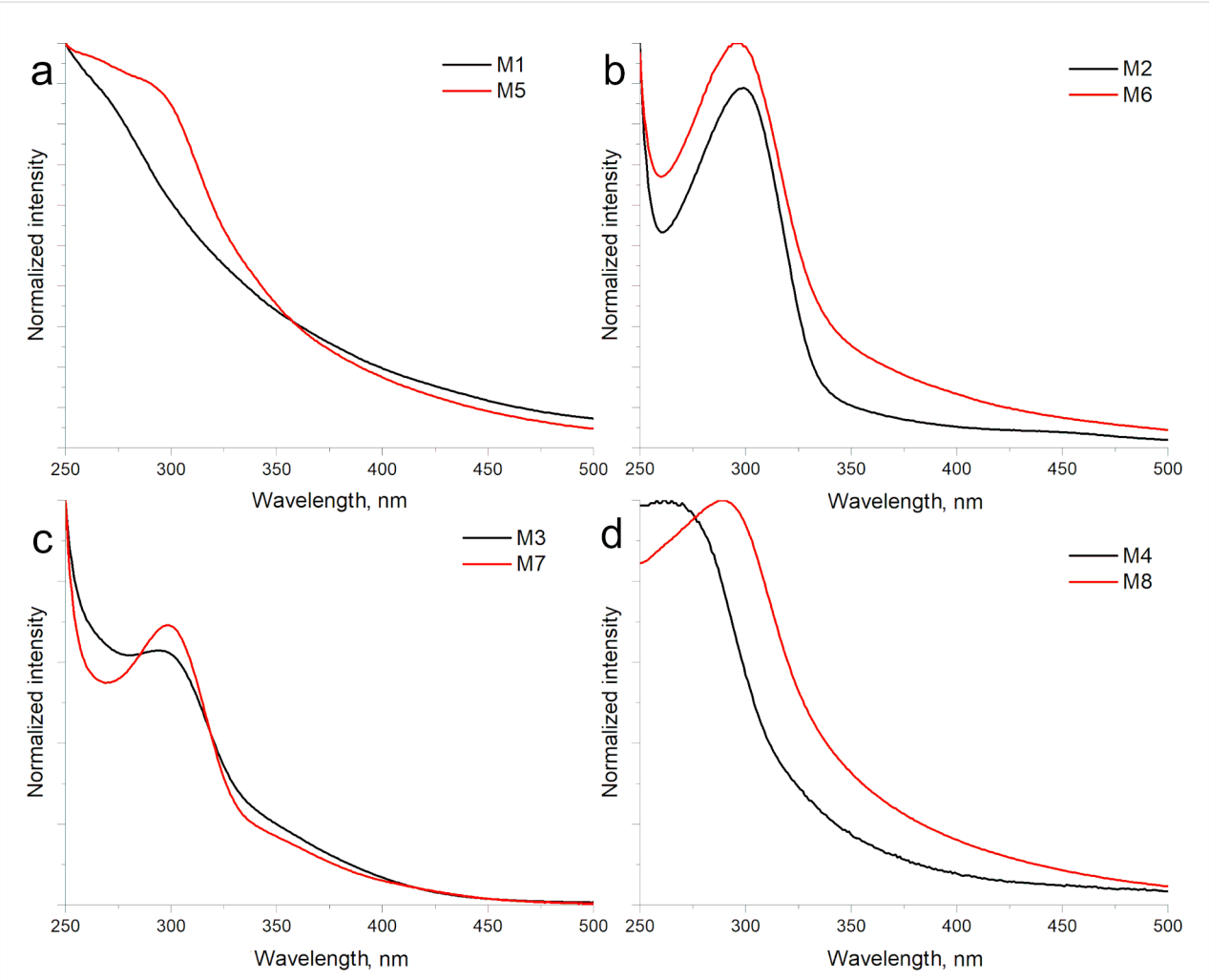


Figure 1: UV–vis absorbance spectra of CQD samples synthesized with a) urea (M1 grape and M5 watermelon); b) urea and nitric acid (M2 grape and M6 watermelon); c) nitric acid (M3 grape and M7 watermelon); and d) deionized water (M4 grape and M8 watermelon).

the other hand, samples M5 and M8 exhibit an asymmetric behavior in their absorption band centered around 340 nm. The difference can be associated with the polydispersity of the CQDs due to the absence of acid oxidation processes. In this case, the hydrothermal treatment is solely responsible for the formation of CQDs. This same condition was observed when modifying the type of precursor (grape pomace). However, in the case of the samples prepared from grape pomace, a considerably less intense band is observed for the systems prepared with urea (M1 and M5). This is possibly associated with a low production of CQDs (Figure 1a). Samples M1 and M5 exhibit a barely noticeable band between 250 and 300 nm, a typical peak was not observed for both samples probably due to the presence of some carbon impurity that hinder the detection of the π–π^* transition around 270 nm.

Dynamic light scattering

Figure 2 shows the size distribution of the CQDs by DLS. Notably, samples M2, M3, M6, and M7, synthesized with acid, exhibit characteristic sizes of quantum dots within the range of 1 to 10 nm. In contrast, samples M1 and M5, synthesized with urea, display larger sizes ranging from 10 to 100 nm, while samples M4 and M8, synthesized only using water, have sizes close to 100 nm. It is important to note that the samples prepared using grape pomace peel as the biomass source produced smaller particle sizes compared to those prepared with watermelon peel under identical synthesis conditions. The size distribution determined by DLS underlines the influence of biomass source and synthesis parameters on the resulting CQD dimensions.

Fourier-transform infrared spectroscopy

The surface chemical groups of the samples were analyzed using FTIR spectroscopy. Figure 3a displays the FTIR spectrum of the CQDs synthesized with grape pomace. Since the systems were prepared in water, some of the signals may have been shielded. In the spectrum, the absorption bands at 3350 cm^{-1} correspond to OH vibrations and N–H bonds, likely originating from water derived from the oxidation process. These bands are characteristic of the hydroxyl groups present in the acid structure. The peaks around 1600 cm^{-1} fall within the C–O range. The samples synthesized with nitric acid oxidation exhibit an additional peak at 1400 cm^{-1}, associated with C–H and C–N bending vibrations, indicating the introduction of nitrogen atoms and oxygen-containing groups. The oxidation process enhances the solubility of CQDs in water. The spectrum also shows low-intensity signals in the range of 1800 to 2500 cm^{-1}, which are characteristic of aromatic compounds [22,27].

In Figure 3b, the FTIR spectrum of the CQDs synthesized from watermelon peel is shown. Similar characteristics to the grape pomace CQDs samples can be observed, especially for sample M7, which was also synthesized using nitric acid (similar conditions as sample M3). However, the characteristic carbon/nitrogen groups of the acid, are not observed in sample M7. This could be attributed to the complete consumption of these groups during the treatment, resulting in their signals not being detected in this analysis.

Raman spectroscopy

Figure 4 shows the Raman spectra for all synthesized samples. On the left side, the spectra of the samples prepared from grape pomace are shown. Two broad bands appear in all samples, one centered around 1300 cm^{-1} and another one centered around 1550 cm^{-1}. These features can be related with the D and G bands, respectively [41]. The D band, usually centered around 1385 cm^{-1}, corresponds to C with an sp^3 hybridization and is commonly associated with disordered surfaces. On the other hand, the G band is typically located around 1575 cm^{-1}, and corresponds to C with an sp^2 hybridization which is related with the graphitic structure [41]. Nevertheless, all of our

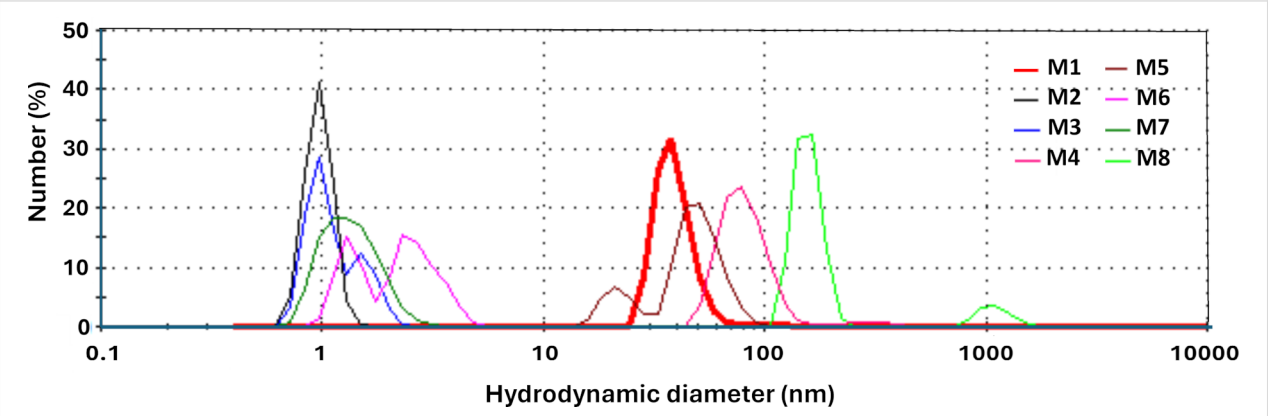


Figure 2: Size distribution of CQDs by dynamic light scattering.

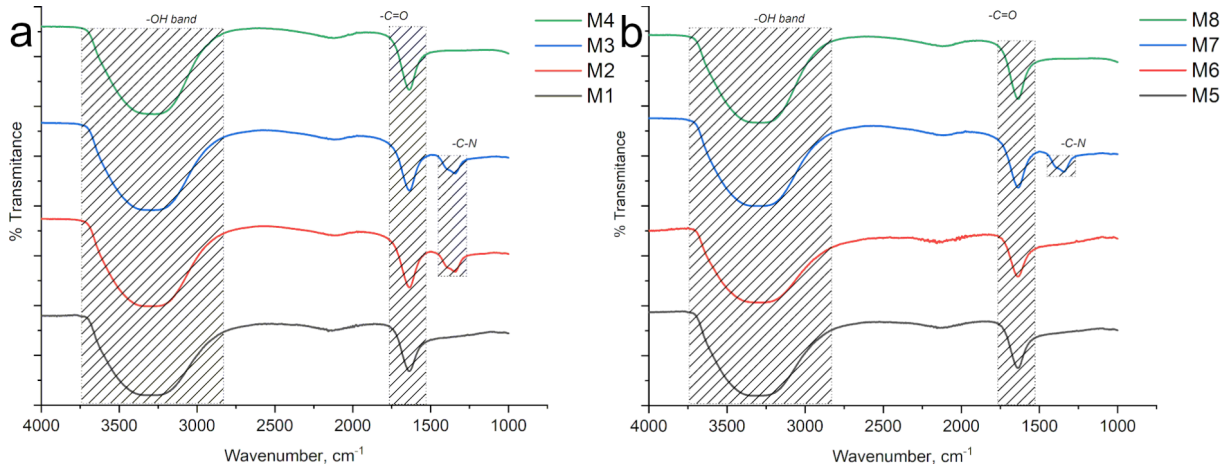


Figure 3: FTIR of a) grape pomace peel with carbonyl peaks, carbon/nitrogen bonds, OH vibrations and some overtones of the benzene ring can be observed, and b) watermelon peel shows characteristics similar to grape pomace samples.

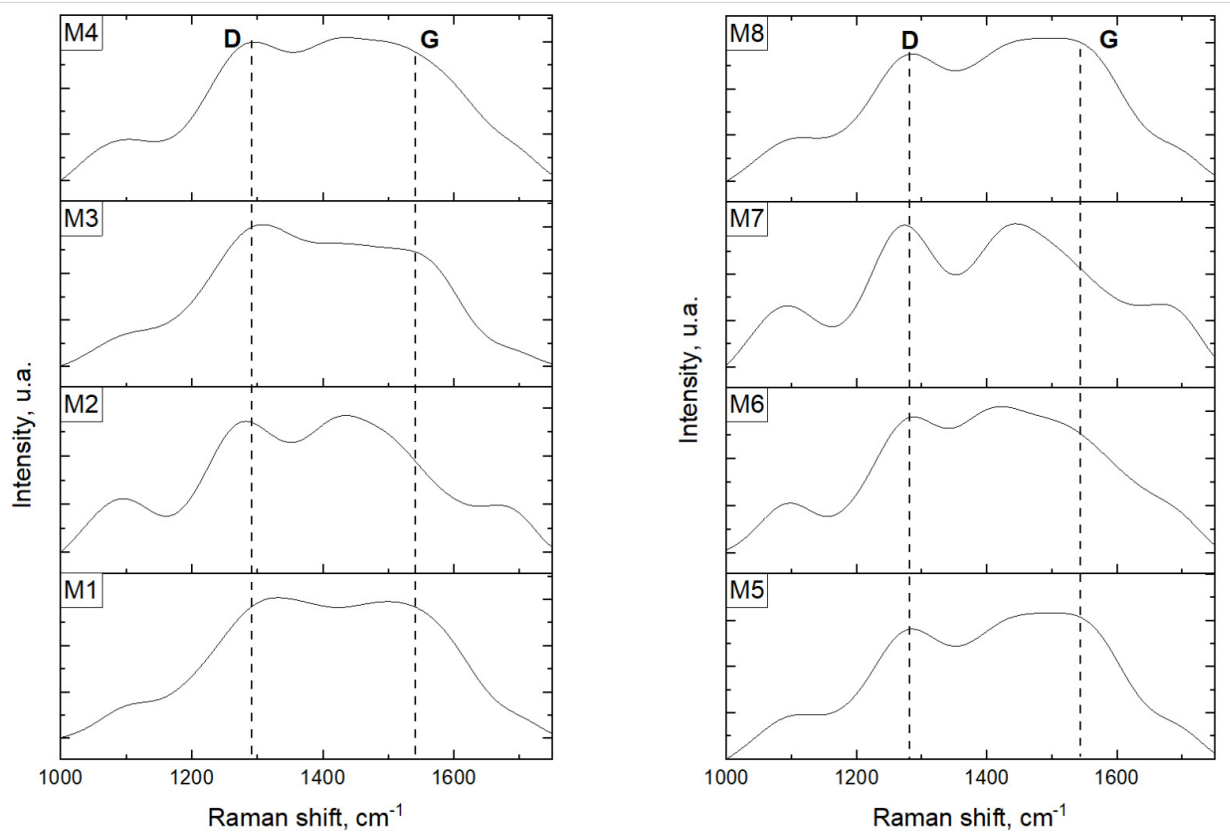


Figure 4: Raman spectra recorded for CQDs prepared from grape pomace (left) and watermelon peel (right) as carbon sources.

samples presents a noticeable broadening of the peak and a shift in the position of the D and G bands, similarly to what has been previously reported [18,42]. In both cases, such modification in the D and G bands was correlated with the presence of heteroatoms in the CQD structure. The synthesis method reported in this work involves chemical (nitric acid treatment) and physical conditions (hydrothermal treatment) which promotes the inclusion of heteroatoms into the CQDs. All the prepared CQDs samples presented an intensity ratio (I_D/I_G) around 1.0, which corresponds to a poor crystallinity in the CQDs and, as a consequence, a high relative content of defects.

Photoluminescence spectra

Investigating the underlying origin and mechanisms governing the multi-fluorescence behavior of carbon dots has garnered significant interest in recent times. Diverse research groups have delved into the fluorescence characteristics of CQDs, presenting varied mechanistic explanations. These encompass phenomena such as recombination of electron–hole pairs, quantum effects, surface functional groups, surface states, molecular states, and fluorophores exhibiting differing degrees of π-conjugation. Generally, CQDs comprise a carbon-core domain and surface domains [29].

In the context of PL processes in CQDs, the emission of fluorescence is intriguing and often associated with the presence of surface defects. Various researchers have highlighted the role of radiative recombination of electron–hole pairs and the influence of functional groups within the carbon network in driving the fluorescence phenomenon [24,30,31]. Furthermore, carbon nanomaterials exhibiting fluorescence, such as carbon oxide dots, exhibit a diverse array of structural elements, including sp^2 carbon hybridization or partial hybridization commonly observed in carbon oxide dots [30,31].

The PL down-conversion spectra of the CQDs synthesized from grape pomace and watermelon peel are shown in Figure 5a and Figure 5b, respectively. All samples were excited at a wavelength of 350 nm, and the emission was observed in the range of 440-450 nm. The samples prepared with urea, namely M1 and M5, exhibited higher intensity in the PL spectra. The PL emission of CQDs can also be influenced by the surrounding acidic conditions, potentially leading to fluorescence quenching. Notably, the sample M3 synthesized using nitric acid demonstrated lower PL intensity, possibly due to such quenching effects under acidic conditions [32].

The upconversion luminescence observed in Figure 7 shows a phenomenon where the emitted fluorescence has a shorter wavelength than the excitation wavelength. This is different from the down-conversion luminescence, where the excitation occurs in the UV region and the emission takes place in the visible spectrum. Unlike down-conversion luminescence, upconversion luminescence does not require high photon density and can occur under normal excitation conditions [31]. Several authors have reported the existence of upconversion carbon dots (CDs). For example, Zhu et al. [43] demonstrated upconversion CDs, while Zhuo et al. [44] reported graphene CDs with upconversion luminescence. The theoretical framework proposed for upconversion photoluminescence centers on the concept of quantum confinement effect (QCE). In this scenario, electrons migrate from the lowest unoccupied molecular orbital (LUMO) to the highest occupied molecular orbital (HOMO) when the excitation wavelength surpasses 600 nm. This process is elucidated in Figure 6 [23,34].

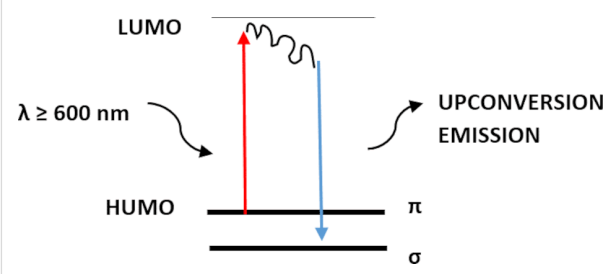


Figure 6: Upconversion process of the quantum confinement effect.

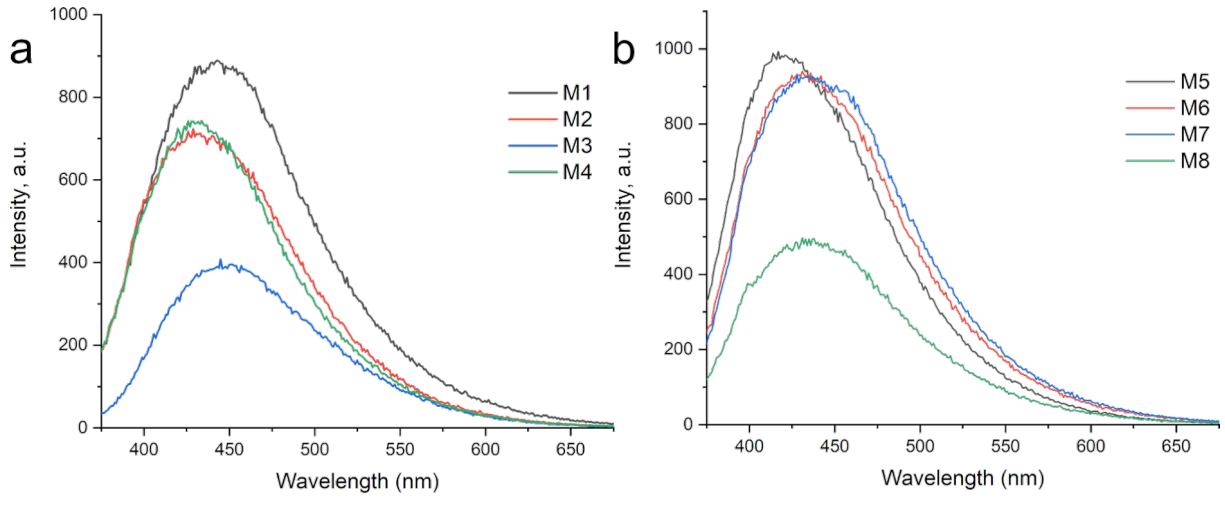


Figure 5: PL spectra, the samples were excited at 350 nm. The graphics corresponds to a) grape pomace peel and b) watermelon peel.

In Figure 7 is observed the upconversion PL of all samples, with excitation at 900 nm and emission in the visible spectra at 720–730 nm. The samples from grape pomace were the ones with more emission than the samples from watermelon, showing similar behavior as the down-conversion process. Besides the main emission band centered around 720–730 nm, all samples exhibited a second band around 840 nm. Considering the upconversion PL mechanism, the authors consider that the presence of heteroatoms in the CQD structure promotes the formation of intermediary states, which may give place to a new emission band. A similar upconversion PL was reported by Wang et al., for CQDs obtained by the hydrothermal method and decorated with $BiVO_4$ [45].

Photocatalytic activity

To carry out the evaluation of the catalytic activity with each of the obtained samples, the curves were first fitted using the calculation of the reaction rate with the pseudo-first-order method. The calculation of the reaction rate constant can be performed using the first-order kinetic model. The first-order rate equation is given by:

$$\ln\left(\frac{C_0}{C}\right) = kt,$$

where C_0 is the initial concentration of the reactant (MB dye), C is the concentration of the reactant at time t, k is the first-order rate constant, and t is the reaction time.

The value of the kinetic rate constant (k) was estimated based on the slope of the linear fit of the $\ln(C_0/C)$ as a function of t (Figure 8). The concentration of MB was estimated based on the absorbance of the peak centered at 664 nm, using the Lambert–Beer law. As expected, the synthesized CQDs were catalytically active for the photodegradation of MB. All samples displayed a linear behavior and exhibited R^2 values around 0.98 for the degradation of the MB dye (Figure 8), except for the sample M4 under a tungsten 40 W lamp (W lamp), which did not show significant changes on the concentration of the MB. Besides, sample M8 displayed the second lowest rate constant, given that samples M4 and M8 were synthesized in the absence of any hydrolyzing agent (urea) or acidic compound (nitric acid). This led to poor degradation of organic matter, resulting in relatively large carbon structures (over 100 nm) as it was shown in Figure 4, which does not correspond to the size range of a CQD. Nevertheless, when these samples were exposed to sunlight, both exhibited a remarkable increment on their catalytic activity. This indicates that, even when the size on these carbon structures does not correspond to that of the CQDs, the photodegradation can be activated possibly due to an electron–hole pair on the surface of the carbon structure. Due to its size, the crystal structure effects can be enhanced.

The expected mechanism for the photodegradation of MB is related with the formation of electron–hole pairs that, due to their oxidizing properties, promotes the formation of OH^- radicals. These species are responsible for the mineralization of the MB molecule [38]. Other aspects that contribute to the MB degradation are the adsorption capacity of MB on the photocatalyst surface (i.e., CQD) and the specific surface area of the CQDs.

All samples (but M3 and M7) presented a similar behavior, increasing their photocatalytic activity when exposed to the

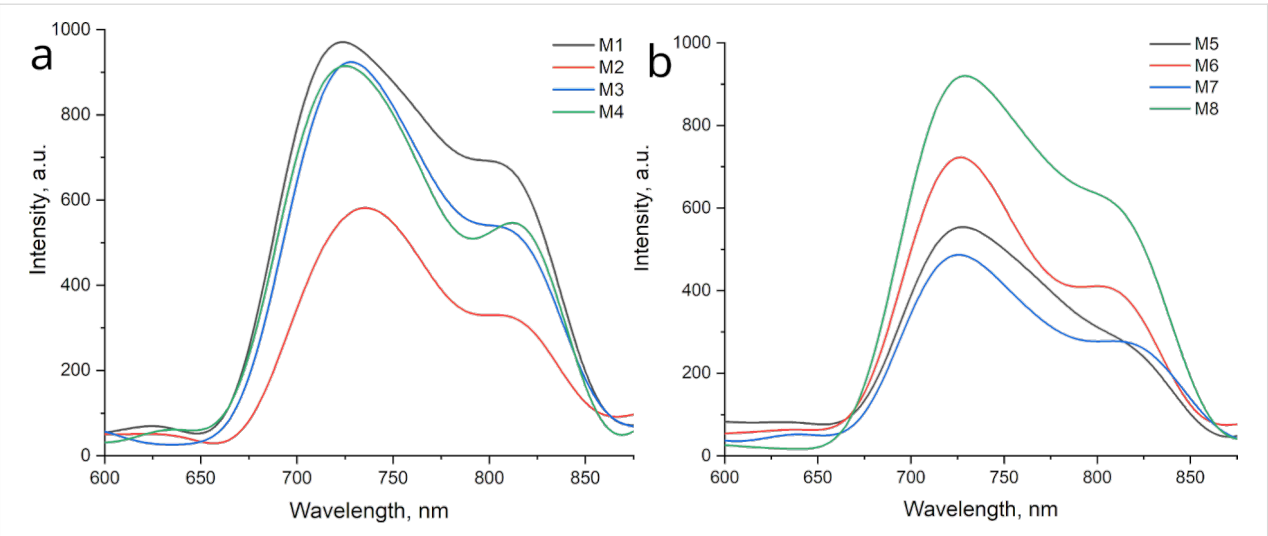


Figure 7: Upconversion PL of the samples, the graphics corresponds to grape pomace peel (M1 to M4) and watermelon peel (M5 to M8). Excitation wavelength: 900 nm.

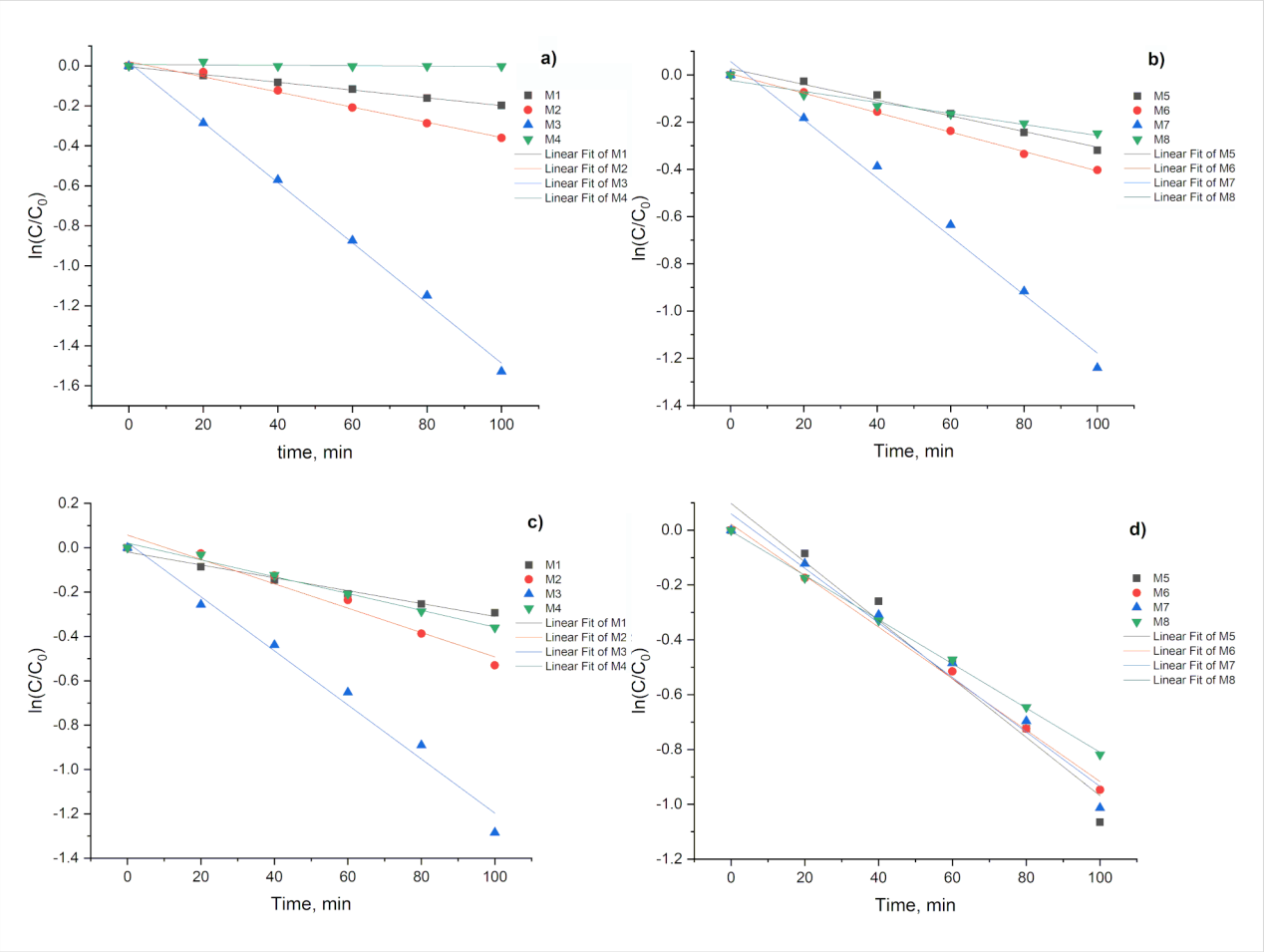


Figure 8: First order adjustment for MB photodegradation for a) grape pomace, W lamp; b) grape pomace, sunlight; c) watermelon peel, W lamp; and d) watermelon peel, sunlight.

sunlight in comparison with their performance under incandescent lamp. It is commonly known that the sunlight emission spectrum presents a higher intensity at the ultraviolet range if compared to that of the tungsten lamp. Considering the band gap of the CQDs, we can affirm that sunlight does create electron–hole pairs more efficiently than the incandescent lamp, which increases the photocatalytic activity of the CQDs.

On the other hand, samples M3 and M7 displayed an opposed behavior, decreasing their photocatalytic activity when exposed to sunlight in comparison to the W lamp. Both samples were prepared under the same conditions but using two different sources of biomass. As nitric acid was used during the synthesis, the presence of C–N groups on the as-synthesized CQDs is expected, which was confirmed by FTIR spectroscopy (Figure 3). According to the report by Rani in 2018 [46], the presence of heteroatoms into the CQDs, such as oxygen, sulfur, and nitrogen, leads to interband states, which decreases the recombination speed of electron–hole pairs. Such delay enhances the photodegradation rate, which was observed for both samples (M3 and M7) independently from the nature of the biomass source.

Considering that the MB molecule contains azo bonds consisting of double bonds (–N=N–), it is possible to foresee a strong interaction with C–N groups on the surface of species M3 and M7. On the other hand, such C–N groups could cause a shift in the electronic energy states [43], which facilitates the formation of electron–hole pairs when irradiated with a W lamp, resulting in a higher photocatalytic activity in comparison to that with sunlight irradiation.

Even when samples M2 and M6 were synthesized using also nitric acid, the formation of C–N groups on their surfaces could be attenuated by the urea (also used during this synthesis), given that above 90ºC urea decomposes forming basic species that can partially neutralize nitric acid acidity.

Additionally, the samples with smaller sizes (ranging from 1 to 10 nm) as determined by DLS, display higher catalytic activity.

Specifically, samples M4 and M8 synthesized from grape pomace and watermelon, respectively, show considerable catalytic activity under sunlight irradiation. However, when analyzed under incandescent light, these samples exhibit very low activity, likely due to their specific chemical composition and the variations in light intensity between the two light sources. The comparison of the kinetic rate constant (k) showing the catalytic activity is shown in Figure 9.

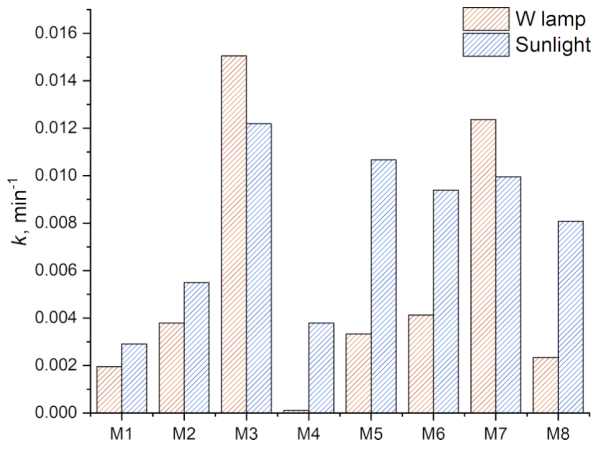


Figure 9: Rate constant values for the photocatalytic activity of CQDs synthesized from grape pomace and watermelon peel. (a) Sunlight radiation in blue, b) light radiation with W lamp in red.

Finally, in Figure 10, the percentages of degradation achieved for each of the catalysts under the irradiation of the two types of light are presented. These results confirm that sample M3 synthesized from grape pomace exhibits the highest level of degradation, reaching 78% under incandescent light and 72% under sunlight. Thus, it demonstrates superior activity compared to other reported CQDs used as catalysts, such as the nanomaterials obtained from uchuva and luminol.

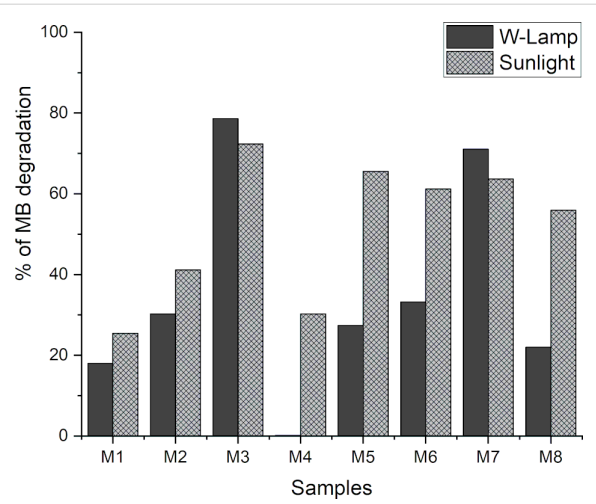


Figure 10: Percentage of MB degradation presented by CQDs to be used as catalysts in the degradation of MB dye. a) Solid bars: incandescent light, b) Hatched bars: solar light.

The comparison of MB degradation from CQDs shows that most samples effectively degraded MB. Notably, samples M4 and M8, synthesized without certain compounds, exhibit limited activity under incandescent light but improve significantly under sunlight. Additionally, smaller-sized samples demonstrate higher catalytic activity, with sample M3 from grape pomace exhibiting superior performance compared to that of other reported CQDs.

Conclusion

The successful synthesis of luminescent and stable carbon quantum dots (CQDs) via the hydrothermal method using biomass as a precursor was achieved. We found that optimized synthesis parameters led to CQDs with diverse chemical characteristics. Notably, samples derived from grape pomace and watermelon peels synthesized with nitric acid, exhibited superior catalytic activity in methylene blue degradation, along with enhanced luminescence and stability compared to those synthesized with urea. It was also found that heteroatoms in the CQDs structure play an important role in the photocatalytic activity of the CQDs as well as in the upconversion photoluminescent behavior.

Our investigation also revealed that solar light was more effective than incandescent light in catalyzing reactions, and smaller-sized CQDs (1–10 nm) displayed higher catalytic activity, particularly evident in grape-pomace-derived samples. The superior performance of certain samples highlights the critical role of synthesis parameters and biomass sources in tailoring CQD properties for advanced photocatalytic applications. Furthermore, the assessment of luminescence activity unveiled the potential of CQDs for biomedical imaging, particularly with upconversion luminescence. This presents opportunities for targeted cell identification and drug delivery.

This study underscores the efficacy of the top-down hydrothermal method for CQD production, offering insights for tailored applications and emphasizing the potential of biomass-derived nanomaterials in environmental remediation and biomedicine, paving the way for the development of sustainable and effective technologies.

Acknowledgements

The authors wish to acknowledge CETYS University and the Centro de Nanociencias y Nanotecnologia (CNyN) of UNAM for the technical support. Special thanks to JND De León for RAMAN analysis of the samples.

Conflicts of Interest

The authors declare no conflict of interest.

Author Contributions

Dalia Chávez-García: conceptualization; data curation; formal analysis; funding acquisition; investigation; methodology; project administration; resources; supervision; validation; visualization; writing – original draft; writing – review & editing. Mario Guzman: conceptualization; data curation; formal analysis; investigation; methodology; project administration; resources; software; supervision; validation; writing – review & editing. Viridiana Sanchez: data curation; formal analysis; investigation; validation. Rubén D. Cadena-Nava: formal analysis; investigation; resources; writing – review & editing.

ORCID® iDs

Dalia Chávez-García - https://orcid.org/0000-0002-1258-7238
Mario Guzman - https://orcid.org/0000-0002-0873-4936
Viridiana Sanchez - https://orcid.org/0009-0002-4517-3856
Rubén D. Cadena-Nava - https://orcid.org/0000-0001-8428-6701

Data Availability Statement

The data that supports the findings of this study is available from the corresponding author upon reasonable request.

Preprint

A non-peer-reviewed version of this article has been previously published as a preprint: https://doi.org/10.3762/bxiv.2024.12.v1

References

1. Sun, X.; Lei, Y. *TrAC, Trends Anal. Chem.* **2017,** *89,* 163–180. doi:10.1016/j.trac.2017.02.001
2. Khattab, T. A.; Abdelrahman, M. S.; Rehan, M. *Environ. Sci. Pollut. Res.* **2020,** *27,* 3803–3818. doi:10.1007/s11356-019-07137-z
3. Holkar, C. R.; Jadhav, A. J.; Pinjari, D. V.; Mahamuni, N. M.; Pandit, A. B. *J. Environ. Manage.* **2016,** *182,* 351–366. doi:10.1016/j.jenvman.2016.07.090
4. Verma, A. K.; Dash, R. R.; Bhunia, P. *J. Environ. Manage.* **2012,** *93,* 154–168. doi:10.1016/j.jenvman.2011.09.012
5. Ibupoto, A. S.; Qureshi, U. A.; Ahmed, F.; Khatri, Z.; Khatri, M.; Maqsood, M.; Brohi, R. Z.; Kim, I. S. *Chem. Eng. Res. Des.* **2018,** *136,* 744–752. doi:10.1016/j.cherd.2018.06.035
6. Asencios, Y. J. O.; Lourenço, V. S.; Carvalho, W. A. *Catal. Today* **2022,** *388–389,* 247–258. doi:10.1016/j.cattod.2020.06.064
7. Tang, L.; Ji, R.; Cao, X.; Lin, J.; Jiang, H.; Li, X.; Teng, K. S.; Luk, C. M.; Zeng, S.; Hao, J.; Lau, S. P. *ACS Nano* **2012,** *6,* 5102–5110. doi:10.1021/nn300760g
8. Fu, F.; Wang, Q. *J. Environ. Manage.* **2011,** *92,* 407–418. doi:10.1016/j.jenvman.2010.11.011
9. Sivakumar, R.; Lee, N. Y. *Chemosphere* **2022,** *286,* 131890. doi:10.1016/j.chemosphere.2021.131890
10. Khan, M.; Assal, M. E.; Tahir, M. N.; Khan, M.; Ashraf, M.; Hatshan, M. R.; Khan, M.; Varala, R.; Badawi, N. M.; Adil, S. F. *J. Saudi Chem. Soc.* **2022,** *26,* 101544. doi:10.1016/j.jscs.2022.101544
11. Wu, D.; Xie, X.; Zhang, Y.; Zhang, D.; Du, W.; Zhang, X.; Wang, B. *Front. Mater.* **2020,** *7,* 2. doi:10.3389/fmats.2020.00002
12. Shafique, M.; Mahr, M. S.; Yaseen, M.; Bhatti, H. N. *Mater. Chem. Phys.* **2022,** *278,* 125583. doi:10.1016/j.matchemphys.2021.125583
13. Frasco, M. F.; Chaniotakis, N. *Sensors* **2009,** *9,* 7266–7286. doi:10.3390/s90907266
14. SalmanOgli, A. *Cancer Nanotechnol.* **2011,** *2,* 1–19. doi:10.1007/s12645-011-0015-7
15. Wu, H.-F.; Gopal, J.; Abdelhamid, H. N.; Hasan, N. *Proteomics* **2012,** *12,* 2949–2961. doi:10.1002/pmic.201200295
16. Demchenko, A. P.; Dekaliuk, M. O. *Methods Appl. Fluoresc.* **2013,** *1,* 042001. doi:10.1088/2050-6120/1/4/042001
17. Li, H.; Kang, Z.; Liu, Y.; Lee, S.-T. *J. Mater. Chem.* **2012,** *22,* 24230–24253. doi:10.1039/c2jm34690g
18. Dong, Y.; Pang, H.; Yang, H. B.; Guo, C.; Shao, J.; Chi, Y.; Li, C. M.; Yu, T. *Angew. Chem., Int. Ed.* **2013,** *52,* 7800–7804. doi:10.1002/anie.201301114
19. Ehtesabi, H.; Nasri, R. *Adv. Nat. Sci.: Nanosci. Nanotechnol.* **2021,** *12,* 025006. doi:10.1088/2043-6262/abffc9
20. Miao, X.; Yan, X.; Qu, D.; Li, D.; Tao, F. F.; Sun, Z. *ACS Appl. Mater. Interfaces* **2017,** *9,* 18549–18556. doi:10.1021/acsami.7b04514
21. Ozyurt, D.; Kobaisi, M. A.; Hocking, R. K.; Fox, B. *Carbon Trends* **2023,** *12,* 100276. doi:10.1016/j.cartre.2023.100276
22. Wang, Y.; Hu, A. *J. Mater. Chem. C* **2014,** *2,* 6921–6939. doi:10.1039/c4tc00988f
23. Kang, C.; Huang, Y.; Yang, H.; Yan, X. F.; Chen, Z. P. *Nanomaterials* **2020,** *10,* 2316. doi:10.3390/nano10112316
24. Jusuf, B. N.; Sambudi, N. S.; Isnaeni; Samsuri, S. *J. Environ. Chem. Eng.* **2018,** *6,* 7426–7433. doi:10.1016/j.jece.2018.10.032
25. Wang, Q.; Liu, X.; Zhang, L.; Lv, Y. *Analyst* **2012,** *137,* 5392–5397. doi:10.1039/c2an36059d
26. Shahraki, H. S.; Bushra, R.; Shakeel, N.; Ahmad, A.; Quratulen; Ahmad, M.; Ritzoulis, C. *J. Bioresour. Bioprod.* **2023,** *8,* 162–175. doi:10.1016/j.jobab.2023.01.009
27. Tyagi, A.; Tripathi, K. M.; Singh, N.; Choudhary, S.; Gupta, R. K. *RSC Adv.* **2016,** *6,* 72423–72432. doi:10.1039/c6ra10488f
28. De, B.; Karak, N. *RSC Adv.* **2013,** *3,* 8286–8290. doi:10.1039/c3ra00088e
29. Sahu, S.; Behera, B.; Maiti, T. K.; Mohapatra, S. *Chem. Commun.* **2012,** *48,* 8835–8837. doi:10.1039/c2cc33796g
30. Sanchez-Sanchez, A.; Izquierdo, M. T.; Mathieu, S.; González-Álvarez, J.; Celzard, A.; Fierro, V. *Green Chem.* **2017,** *19,* 2653–2665. doi:10.1039/c7gc00491e
31. Liu, H.; Ye, T.; Mao, C. *Angew. Chem., Int. Ed.* **2007,** *46,* 6473–6475. doi:10.1002/anie.200701271
32. Prasannan, A.; Imae, T. *Ind. Eng. Chem. Res.* **2013,** *52,* 15673–15678. doi:10.1021/ie402421s
33. Kailasa, S. K. V.; Mehta, N.; Hasan, N.; Wu, H.-F. Applications of carbon dots in biosensing and cellular imaging. In *Nanobiomaterials in Medical Imaging Applications of Nanobiomaterials;* Grumezescu, A. M., Ed.; William Andrew Publishing: Oxford, UK, 2016; Vol. 8, pp 339–364. doi:10.1016/b978-0-323-41736-5.00011-x
34. Shen, J.; Zhu, Y.; Yang, X.; Li, C. *Chem. Commun.* **2012,** *48,* 3686–3699. doi:10.1039/c2cc00110a

35. Hu, C.; Li, M.; Qiu, J.; Sun, Y.-P. *Chem. Soc. Rev.* **2019,** *48,* 2315–2337. doi:10.1039/c8cs00750k
36. Singh, P.; Rani, N.; Kumar, S.; Kumar, P.; Mohan, B.; Pallavi; Bhankar, V.; Kataria, N.; Kumar, R.; Kumar, K. *J. Cleaner Prod.* **2023,** *413,* 137474. doi:10.1016/j.jclepro.2023.137474
37. Zhang, R.; Liu, Y.; Yu, L.; Li, Z.; Sun, S. *Nanotechnology* **2013,** *24,* 225601. doi:10.1088/0957-4484/24/22/225601
38. Cheng, C.; Shi, Y.; Li, M.; Xing, M.; Wu, Q. *Mater. Sci. Eng., C* **2017,** *79,* 473–480. doi:10.1016/j.msec.2017.05.094
39. Houas, A.; Lachheb, H.; Ksibi, M.; Elaloui, E.; Guillard, C.; Herrmann, J.-M. *Appl. Catal., B* **2001,** *31,* 145–157. doi:10.1016/s0926-3373(00)00276-9
40. Yuan, M.; Zhong, R.; Gao, H.; Li, W.; Yun, X.; Liu, J.; Zhao, X.; Zhao, G.; Zhang, F. *Appl. Surf. Sci.* **2015,** *355,* 1136–1144. doi:10.1016/j.apsusc.2015.07.095
41. Mathew, S. A.; Praveena, P.; Dhanavel, S.; Manikandan, R.; Senthilkumar, S.; Stephen, A. *RSC Adv.* **2020,** *10,* 24386–24396. doi:10.1039/d0ra04599c
42. Gao, D.; Zhang, Y.; Liu, A.; Zhu, Y.; Chen, S.; Wei, D.; Sun, J.; Guo, Z.; Fan, H. *Chem. Eng. J.* **2020,** *388,* 124199. doi:10.1016/j.cej.2020.124199
43. Zhu, S.; Song, Y.; Wang, J.; Wan, H.; Zhang, Y.; Ning, Y.; Yang, B. *Nano Today* **2017,** *13,* 10–14. doi:10.1016/j.nantod.2016.12.006
44. Zhuo, S.; Shao, M.; Lee, S.-T. *ACS Nano* **2012,** *6,* 1059–1064. doi:10.1021/nn2040395
45. Wang, G.; Zhang, W.; Li, J.; Dong, X.; Zhang, X. *J. Mater. Sci.* **2019,** *54,* 6488–6499. doi:10.1007/s10853-019-03316-y
46. Rani, U. A.; Ng, L. Y.; Ng, C. Y.; Mahmoudi, E.; Ng, Y.-S.; Mohammad, A. W. *J. Water Process Eng.* **2021,** *40,* 101816. doi:10.1016/j.jwpe.2020.101816

License and Terms

This is an open access article licensed under the terms of the Beilstein-Institut Open Access License Agreement (https://www.beilstein-journals.org/bjnano/terms), which is identical to the Creative Commons Attribution 4.0 International License (https://creativecommons.org/licenses/by/4.0). The reuse of material under this license requires that the author(s), source and license are credited. Third-party material in this article could be subject to other licenses (typically indicated in the credit line), and in this case, users are required to obtain permission from the license holder to reuse the material.

The definitive version of this article is the electronic one which can be found at:
https://doi.org/10.3762/bjnano.15.63

BEILSTEIN JOURNAL OF NANOTECHNOLOGY

Nanoarchitectonics with cetrimonium bromide on metal nanoparticles for linker-free detection of toxic metal ions and catalytic degradation of 4-nitrophenol

Akash Kumar[1,2] and Raja Gopal Rayavarapu[*1,2]

Full Research Paper

Open Access

Address:
[1]Nanomaterial Toxicology Laboratory, Drug and Chemical Toxicology Group, Food, Drug and Chemical, Environment and Systems Toxicology (FEST) Divison, CSIR-Indian Institute of Toxicology Research (CSIR-IITR), Vishvigyan Bhawan, 31 Mahatma Gandhi Marg, Lucknow 226001, India and [2]Academy of Scientific and Innovative Research (AcSIR), Ghaziabad 201002, India

Email:
Raja Gopal Rayavarapu[*] - rajagopal@iitr.res.in

* Corresponding author

Keywords:
catalysis; CTAB; heavy metal; nanoparticles; 4-nitrophenol; sensing

Beilstein J. Nanotechnol. **2024,** *15,* 1312–1332.
https://doi.org/10.3762/bjnano.15.106

Received: 06 June 2024
Accepted: 25 September 2024
Published: 04 November 2024

This article is part of the thematic issue "Advanced functional nanomaterials for water remediation applications".

Guest Editor: J. Singh

© 2024 Kumar and Rayavarapu; licensee Beilstein-Institut.
License and terms: see end of document.

Abstract

Heavy metal ions and organic pollutants, such as 4-nitrophenol (4-NP), pose significant environmental and human health threats. Addressing these challenges necessitates using advanced nanoparticle-based systems capable of efficient detection and degradation. However, conventional approaches utilizing strong capping agents like cetrimonium bromide (CTAB) on nanoparticles lead to limitations due to the rigid nature of CTAB. This restricts its utility in heavy metal detection and 4-NP degradation, requiring additional surface modifications using linker molecules, thereby increasing process complexity and cost. To overcome these limitations, there is a critical need for the development of an easy-to-use, dual-functional, linker-free nanosystem capable of simultaneous detection of heavy metals and efficient degradation of 4-NP. For enabling linker-free/ligand-free detection of heavy metal ions and catalytic degradation of 4-NP, CTAB was engineered as a versatile capping agent on gold and silver nanoparticles. Various factors, including nanoparticle characteristics such as shape, size, metal composition, centrifugation, and NaOH amount, were investigated for their impact on the performance of CTAB-capped nanoparticles in heavy metal detection and 4-NP degradation. CTAB-Au nanospheres demonstrated limited heavy metal ion detection capability but exhibited remarkable efficiency in degrading 94.37% of 4-NP within 1 min. In contrast, silver nanospheres effectively detected Hg^{2+}, Cu^{2+}, and Fe^{3+} at concentrations as low as 1 ppm and degraded 90.78% of 4-NP within 30 min. Moreover, anisotropic gold nanorods (CTAB-AuNR1 and CTAB-AuNR2) showed promising sensing capabilities towards Cu^{2+}, Cr^{3+}, and Hg^{2+} at 0.5 OD, while efficiently degrading 4-NP within 5 min at 1 OD. This study emphasizes the importance of tailoring parameters of CTAB-capped nanoparticles for specific sensing and catalytic applications, offering potential solutions for environmental remediation and human health protection.

Introduction

Metal nanoparticles are widely used for a great number of applications owing to their excellent optochemical properties and high surface-to-volume ratio in comparison to bulk materials. Noble metal (gold and silver) nanoprobes are emerging as versatile colorimetric and spectrophotometric nanosensors for rapid detection/degradation of heavy metal ions and toxic pollutants that pose a serious challenge to environment and human health.

Globally, acceleration of industrial growth and urbanization led to the increased release of pollutants into the environment, causing health concerns to humans. Untreated industrial effluents are released, and most heavy metal ions accumulate in water higher than the permissible limits, pollute drinking water, and are non-biodegradable. Heavy metal ions are potentially carcinogenic, and it is hard to predict their toxicity at early stages of exposure. In addition, industrial wastewater may contain toxic compounds such as the widely used 4-nitrophenol [1]. Hence, one need is to develop a dual-functional and flexible linker-free metal nanoparticle-based sensor that is rapid and affordable for the detection of heavy metal ions as well as for the degradation of organic pollutants such as 4-nitrophenol.

Developing a robust sensing platform based on metal nanoparticles requires a modulation of the surface chemistry, which is governed by the choice of capping agents on the metal surface and further dominates functionalization. Various capping agents such as citrate, PVP, and surfactants have been the choice for metal nanoparticles. Controlled size, shape, and surface properties have been achieved using strong capping and reducing agents. Capping agents maintain size, shape, and stability of the nanoparticles, and suitable capping agents can modulate the nanoarchitectonics of the nanoparticles from atomic to molecular levels [2]. The surface capping can also influence the surface properties of the nanoparticles, making them compatible with specific environments or functional groups [3].

Surfactants bind to metal surfaces and create a stable colloidal solution by preventing the nanoparticles from aggregation or clustering [4]. CTAB is a widely used cationic surfactant that provides nanoparticle ionic stability and anisotropy [5]. Although CTAB delivers high strength to nanoparticles, the use of such nanoparticles is limited in sensing, catalysis, and biomedical applications because of post-synthesis functionalization, morphology, and toxicity [6-8]. CTAB is a resilient molecule on the nanoparticle surface because of its micellar structure and does not allow for interactions with ligands via ion–ion interactions. Therefore, multiple surface modifications or linkers must be used for selective interaction between ligand and CTAB-capped gold and silver nanoparticles [7,9].

Contaminants in form of heavy metals and pollutant such as 4-nitrophenol are both dangerous to humans [10,11]. Contamination with toxic heavy metal ions, including zinc, arsenic, aluminium, chromium, iron, cobalt, copper, nickel, mercury, cadmium, and lead, causes significant chronic damage to organ systems, beginning at the cellular level [12]. Toxic heavy metal ions such as Hg^{2+} are poisonous environmental pollutants that cause damage at the DNA level by inhibiting DNA replication and DNA polymerase activity, ultimately affecting normal cell synthesis [13]. The less toxic Fe^{3+} is an essential nutrient for human health in a lower dose, while increasing the dose also leads to undesirable side effects such as iron overload (hemochromatosis) and acute iron poisoning [14]. Similarly, other metals, including copper and cobalt, significantly damage different body parts above a threshold limit. Heavy metal ions pose a severe risk to human and environmental health [15]. Besides heavy metals, 4-nitrophenol is widely used for dye synthesis, insecticides and pesticides, indicators, and photographic chemicals [16]. Regarding the use of 4-nitrophenol, there are several toxicity concerns via different exposure routes, including dermal, oral, and inhalation [17]. Therefore, developing methods to detect heavy metals at the low concentrations usually found in environmental samples is crucial. Similarly, the removal of 4-nitrophenol from exposed site requires necessary steps.

Heavy metals are detected using high-throughput techniques, such as atomic absorption spectroscopy, atomic emission spectroscopy, surface-enhanced Raman scattering, electrochemical, fluorescence, and colorimetric methods [18,19]. Catalytic hydrogenation is the preferred method for the conversion of 4-nitrophenol to 4-aminophenol, which is less toxic [20]. However, the conversion process is laborious and requires precious metals such as palladium and platinum as catalysts [20]. Colorimetric detection methods have attracted attention because of their advantages, including simplicity, sensitivity, visualization, and real-time detection, while other methods often require expensive instrumentation and complex operational procedures [21]. Colorimetric detection of heavy metals and catalytic conversion of 4-nitrophenol can be achieved using CTAB-capped gold or silver nanoparticles because of their unique surface plasmon resonance (SPR) properties, allowing for a colorimetric analysis through a change in absorption wavelength. The color of gold and silver nanoparticles highly depends on shape, size, and pH value, which are directly influenced by the ligand–metal interaction [22]. Another essential factor is surface capping, which provides colloidal stability and the surface for ionic interaction with ligands [23]. Previously, post-synthesis surface-modified CTAB-capped gold and silver nanoparticles were used to detect various compounds, including heavy

metals [9,24]. Moudgil et al. showed that that poly-L-lysine-coated CTAB-AgNPs are selective and sensitive for detecting Hg^{2+} [9]. GSH-modified isotropic and anisotropic CTAB-AgNPs were used to detect cobalt ions. The author found that only rod-shaped particles enabled visual detection of cobalt [25]. Yagyu et al. showed the efficient removal of radioactive cesium using Prussian blue [26]. Also, 4-nitrophenol was degraded using CTAB-capped gold nanoparticles within 60 min of the reaction in the presence of thiosulfate [27]. The study concluded that nanoparticles of 13 nm can efficiently catalyze the reaction from 4-nitrophenol to 4-aminophenol [27].

A number of studies confirmed that linker-dependent detection and catalytic performance were available using CTAB-capped gold or silver nanoparticles. Unfortunately, only very few studies described CTAB-capped nanoparticles as detection and catalytic systems without surface modifications, linkers, or buffers because of the strong binding of CTAB on the nanoparticle surface. Designing CTAB-capped gold and silver nanoparticles without linker/buffer for catalysis and detection heavy metals is a current need. In this work, we have developed a linker-free nanosensor with CTAB as capping agent on both isotropic and anisotropic gold and silver nanoparticles. The CTAB-capped metal nanoparticles could sense heavy metal ions and also helped in the rapid catalytic degradation of 4-nitrophenol.

Materials and Methods

Materials

Cetrimonium bromide (CTAB) (Cat No. 52370), sodium borohydride ($NaBH_4$) (Cat No. 480886), and ascorbic acid (AA) (Cat No. A7506) were purchased from Sigma-Aldrich. Silver nitrate ($AgNO_3$) (Cat No. 1.93200.0027) and hydrochloric acid (HCl) (Cat No. 1.93001.2521) were obtained from Merck. Sodium hydroxide (NaOH) (Cat No. TC1460), chloroauric acid trihydrate ($HAuCl_4{\cdot}3H_2O$) (Cat No.10724SG001) and 4-nitrophenol (4-NP) (Cat No. 144956) were purchased from CDH fine chemicals, Finar and SRL chemicals, respectively. National Institute of Standard and Technology grade metal standards (1000 ppm) of arsenic (As^{3+}), aluminum (Al^{3+}), cadmium (Cd^{2+}), zinc (Zn^{2+}), mercury (Hg^{2+}), nickel (Ni^{2+}), copper (Cu^{2+}), chromium (Cr^{3+}), lead (Pb^{2+}), iron (Fe^{3+}), and cobalt (Co^{2+}) were purchased from CDH Fine Chemicals, India. The chemicals obtained were used without further purification. All glassware was cleaned with aqua regia and rinsed with double distilled (DD) water before use.

Cetrimonium bromide as capping agent

CTAB-AgNS (silver nanospheres) and CTAB-AuNS (gold nanospheres) were synthesized via wet chemical synthesis using slightly modified protocols [28,29]. In a typical synthesis carried out at 80 °C, 0.5 mL of $AgNO_3$ (100 mM) was reduced using 1 mL of 100 mM $NaBH_4$ in the presence of 5 mL DD water premixed with 1 mL of 100 mM cetrimonium bromide (CTAB) under stirring at 800 rpm. Similarly, gold nanospheres were synthesized by adding 0.5 mL of 25 mM gold chloride solution to 5 mL of cetrimonium bromide (100 mM) followed with the addition of 0.5 mL $NaBH_4$ (100 mM) under stirring at 800 rpm. The silver and gold nanospheres were centrifuged at 18000*g* and 20000*g* for 20 min and 60 min, respectively, to remove impurities. The supernatants were discarded and the pellets were dispersed in DD water and stored at room temperature.

Tunable aspect ratio of gold nanorods capped with CTAB

Gold nanorods of different lengths were synthesized using a two-step protocol as described in previous reports with slight modifications [30]. Briefly, in the first step, gold seeds were prepared by mixing CTAB, $HAuCl_4{\cdot}3H_2O$ and $NaBH_4$. The seed solution acts as an initiator for synthesizing gold nanorods. In the second step, the growth solution was prepared, consisting of CTAB, $AgNO_3$, $HAuCl_4{\cdot}3H_2O$, HCl, and ascorbic acid. A typical synthesis involved the synthesis of CTAB-capped Au seeds of less than 4 nm. Addition to the growth solution in step 2 resulted in the formation of gold nanorods. The seeds were prepared using 200 µL of $HAuCl_4{\cdot}3H_2O$ (25 mM) with 2 mL of 0.1 M CTAB at 80 °C, followed by 800 µL freshly prepared ice-cold $NaBH_4$ (10 mM) added under continuous stirring (800 rpm). The Growth solution of 5 mL of CTAB (100 mM) was placed on a hot plate (80 °C), 500 µL of $HAuCl_4{\cdot}3H_2O$ (10 mM), 50 µL/120 µL (for shorter and longer nanorods, respectively) $AgNO_3$ (10 mM), 200 µL of HCl (1 M), and 80 µL of AA (100 mM) were sequentially added to the reaction mixture. Finally, 50 µL of freshly prepared seed solution was added to the growth solution to initiate the synthesis of gold nanorods. The different sizes of gold nanorods were obtained by varying the volume of $AgNO_3$ solution. Finally, anisotropic AuNR1 (shorter length) and AuNR2 (longer length) were centrifuged at 16,000*g* and 12,000*g* for 20 min, respectively, to remove excess of surfactant and any impurities.

Characterization of CTAB-capped isotropic and anisotropic metal nanoparticles

The plasmonic properties of the synthesized isotropic and anisotropic metal nanostructures were measured using an Epoch2 spectrophotometer (BioTek, USA). Hydrodynamic radius and polydispersity index (PDI) were measured using dynamic light scattering (Zetasizer Nano ZS, Malvern, UK). The zeta potential measurements were conducted to determine the surface charge for both isotropic and anisotropic metal nanoparticles using zeta cuvettes (DTS0012). The precise size

and morphology of CTAB-AgNS, CTAB-AuNS, CTAB-AuNR1, and CTAB-AuNR2 were observed under a transmission electron microscope (TEM, 120 kV; FEI Tecnai). The nanoparticles were placed onto 200-mesh carbon-coated copper grids. The average size of the nanoparticles was calculated using ImageJ software (USA). The crystal structure of CTAB-capped gold and silver nanoparticles was determined using XRD (Rigaku Smartlab, Japan) in a 2θ range of 35° to 80°. The nanoparticle solutions were air-dried, and the obtained powders (20 mg) were used for measurement. The functionalization of AgNS, AuNS, AuNR1, and AuNR2 with CTAB was validated through Fourier-transform infrared spectroscopy (Thermo Scientific, Nicolet iS5, USA). 10 mg of the air-dried nanoparticles were placed over a diamond and measured in the range of 400–4000 cm^{-1}.

Quantification of CTAB through UHPLC

The quantification of bound CTAB on the nanoparticles' surface was analyzed using ultrahigh-performance liquid chromatography (UHPLC; Shimadzu, Nexera, Tokyo, Japan). The chromatography system equipped with an SPD-M20A photodiode array (PDA) detector with a wavelength range of 190–800 nm, a degreaser (DGU-20A_{5R}), autosampler (SIL-30AD), and quaternary pump (LC-30AD). The separation peak for CTAB was analyzed using HpersilGold™ C18 (100 × 2.1 mm, 10 µm) with a pore diameter of 1.9 µm. The injection volume was 5 µL, and the wavelength was 208 nm for CTAB quantification. The mobile phase included a mixture of acetonitrile and water (40:60 v/v) at a 0.2 mL/min flow rate. The method was developed using CTAB powder as standard at different concentrations of 0.625, 1.2, 2.5, 5, 10, and 20 µg/mL in water. The blank sample (which consisted only of solvent) was also analyzed to confirm the peak value of the compound. The supernatants of centrifuged CTAB-capped nanoparticles were used for CTAB quantification.

Stability of CTAB-capped metal nanoparticles in NaCl and NaOH solutions

In order to determine the ability and functionality of CTAB on metal nanoparticle surfaces, we have studied their stability in commonly used 1 M solutions of sodium chloride and sodium hydroxide. The stability of as-prepared and centrifuged nanoparticles of CTAB-AgNS, CTAB-AuNS, CTAB-AuNR1, and CTAB-AuNR2 were evaluated. The optical density (OD) of all CTAB-capped nanoparticles was kept in the vicinity of 0.5 ± 0.1 and 1.0 ± 0.1. Aliquots of 1 M NaOH (volumes ranging between 5–50 µL) was added to the nanoparticle solutions. Also, CTAB-AgNS, CTAB-AuNS, CTAB-AuNR1, and CTAB-AuNR2 were added to 1 M NaCl solution while keeping the optical density of the nanoparticles constant at 0.5 and 1.

Linker-free sensing of heavy metal ions

National Institute of Standard and Technology grade metal standards (1000 ppm) of As^{3+}, Al^{3+}, Cd^{2+}, Zn^{2+}, Hg^{2+}, Ni^{2+}, Cu^{2+}, Cr^{3+}, Pb^{2+}, Fe^{3+}, and Co^{2+} were diluted to a concentration of 10 ppm. A uniform concentration of nanoparticles in terms of optical density (OD) was maintained throughout the experiment. The concentration of CTAB-AgNS, CTAB-AuNS, CTAB-AuNR1, and CTAB-AuNR2 was kept at constant values of 0.5 ± 0.1 OD and 1.0 ± 0.1 OD per milliliter of water during the test. In a typical sensing experiment, the corresponding metal ions were spiked in water. Then, CTAB-AgNS, CTAB-AuNS, CTAB-AuNR1, and CTAB-AuNR2 were dispersed and examined regarding colorimetric/spectrophotometric changes. CTAB-AgNS, CTAB-AuNS, CTAB-AuNR1, and CTAB-AuNR2 were used with aliquots of NaOH (1 M) in a volume range of 5–50 µL. The pH of a sample was not measured because a volume of 5 µL NaOH already yielded pH 12. Consequently, we chose the volume of NaOH as a parameter instead of the pH value.

Catalytic degradation of 4-nitrophenol

The catalytic activity of CTAB-AgNS, CTAB-AuNS, CTAB-AuNR1, and CTAB-AuNR2 was determined by reducing 4-nitrophenol (4-NP) to 4-aminophenol (4-AP) in the presence of $NaBH_4$. All reactions were carried out at room temperature in a 3.5 mL quartz cuvette. The reagent for catalysis was added in a sequence of 2 mL of 4-nitrophenol (0.1 mM), 1 mL of $NaBH_4$ (100 mM), and 50 µL (0.5 ± 0.1 OD and 1.0 ± 0.1 OD) of CTAB-AgNS, CTAB-AuNS, CTAB-AuNR1, and CTAB-AuNR2, centrifuged and as-prepared, respectively. The catalytic conversion of 4-NP to 4-AP was measured using a UV–vis spectrophotometer at 300–900 nm. The disappearance of the color upon adding nanoparticles was measured and further, the change in the plasmon band was recorded. As controls, we chose bare nanospheres of gold/silver and compared them to the CTAB-capped metal nanoparticles [31].

Results and Discussion

Figure 1a shows the synthesis of isotropic and anisotropic metal nanoparticles using CTAB as surfactant. Silver and gold nanospheres, along with nanorods of different lengths were synthesized using wet chemical reduction, as shown in Figure 1a. A unique feature of CTAB is its robust and selective binding to certain crystal facets of metal surfaces that define the growth and nucleation of nanoparticles. CTAB on metal surfaces plays a key role in nanoparticle stabilization but hinders many applications, which in some instances require an external linker or ligand for usable applications. It was reported that for CTAB-capped nanoparticles to enable sensing, the use of a linker on CTAB was mandatory for heavy metal ion detection. Linker-free detection of heavy metals using CTAB is a challenge and

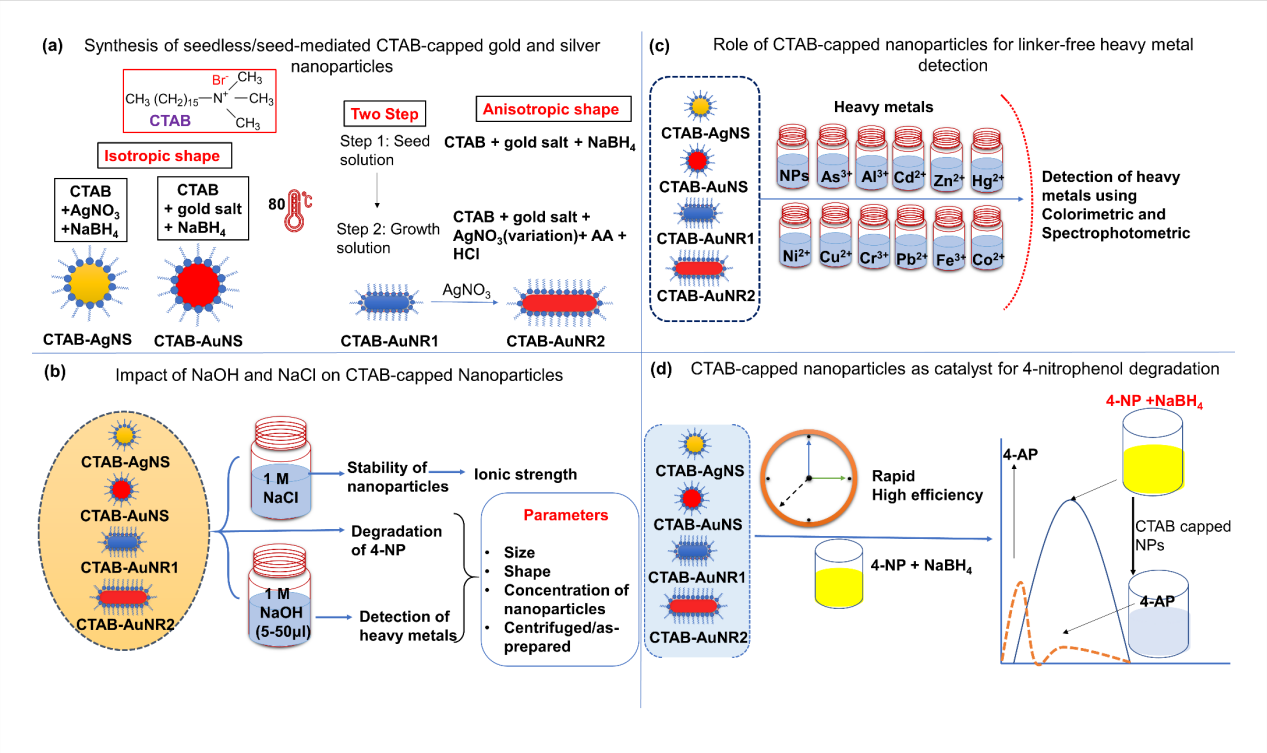


Figure 1: (a) Wet chemical synthesis of CTAB-capped isotropic gold and silver as well as anisotropic gold nanoparticles through seedless and seed-mediated approaches. (b) Assessment of nanoparticle stability in 1 M NaCl and NaOH for sensing applications. Evaluation of linker-free CTAB-capped metal nanoparticles for (c) sensing heavy metal ions and (d) the catalytic degradation of 4-nitrophenol.

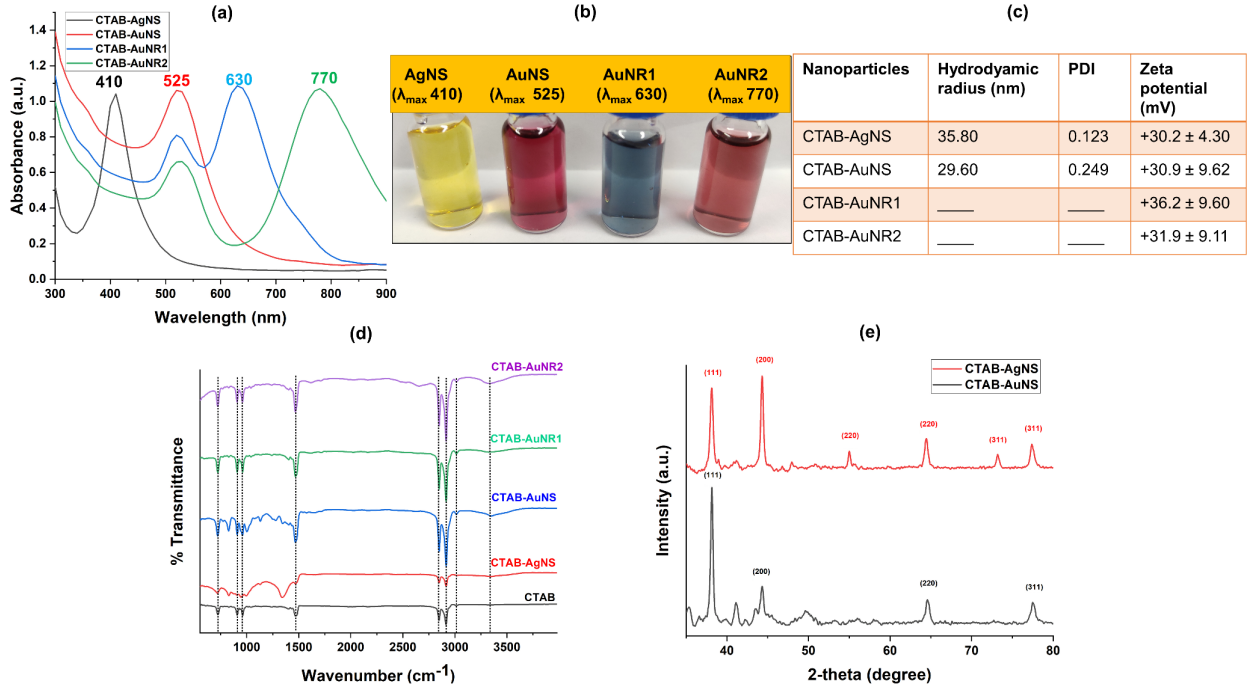
pre-requisite for enabling faster and facile approaches. In this work, we designed several strategies involving the desorption of CTAB from the metal surface in the presence of solvents such as NaOH, which can tune the amount of CTAB on the surface. A recent study showed that sodium borohydride removed CTAB from metal surfaces for ligand exchange, which helped in the detection of heavy metal ions [32]. The impact of NaOH and NaCl was assessed regarding the stability of the synthesized metal nanoparticles at extreme concentrations (Figure 1b). The addition of 1 M NaOH at various volumes (5–50 µL) results in the controlled desorption of CTAB from the metal surface. A recent study demonstrated the ability of NaOH to interfere with CTAB micelles, where the pH value played a key role [33]. Optimized conditions enabled the linker-free sensing of heavy metal ions (Figure 1c). Nanoparticles dispersed in DD water were chosen as control (represented as NPs in Figure 1c). Additionally, CTAB-capped gold and silver nanoparticles have been reported for their enhanced catalytic activity. The simplest and fastest method for degradation or catalytic conversion of 4-nitrophenol is using a strong reducing agent (such as $NaBH_4$) in the presence of a catalytic agent (i.e., the nanoparticles) [27]. In the current study, we also examined the catalytic properties of CTAB-capped nanoparticles in the degradation of 4-nitrophenol (Figure 1d). The catalytic properties of CTAB-capped nanoparticles highly depend on various factors, including size, shape, and reaction parameters [34]. However, there was a gap in the literature regarding which factor is most crucial to the efficient degradation of 4-nitrophenol using nanoparticles. Some studies suggest size is essential, while others suggest pH, surface capping, and linker molecules are required to degrade 4-nitrophenol. Therefore, this study analyzed the impact of size, shape, metal type, and nanoparticle concentration on converting 4-nitrophenol to 4-aminophenol.

Characterization of CTAB-capped nanoparticles

UV–vis, DLS, Zeta, FTIR, XRD, and TEM analyses

Physicochemical characterization was performed using optical spectroscopy, DLS, FTIR, XRD, and TEM analyses. Figure 2a shows the synthesized isotropic silver and gold nanospheres with plasmon bands at 410 nm (AgNS) and 525 nm (AuNS). The anisotropic tunable gold nanorods with longitudinal plasmon bands at 630 nm (AuNR1) and 770 nm (AuNR2) indicate the formation of different lengths of nanorods.

The colloidal solutions of the metal nanoparticles having different sizes and shapes resulted in different colors (Figure 2b), a characteristic feature of gold and silver nanoparticles involving the change in surface plasmon resonance of the metal nanostructures. A single absorbance peak correlates to the symmetri-



Nanoparticles	Hydrodyamic radius (nm)	PDI	Zeta potential (mV)
CTAB-AgNS	35.80	0.123	+30.2 ± 4.30
CTAB-AuNS	29.60	0.249	+30.9 ± 9.62
CTAB-AuNR1	____	____	+36.2 ± 9.60
CTAB-AuNR2	____	____	+31.9 ± 9.11

Figure 2: (a) Optical absorbance of CTAB-AgNS, CTAB-AuNS, CTAB-AuNR1, and CTAB-AuNR2 with maximum absorption wavelengths (λ_{max}) of 410, 525, 630, and 770 nm, respectively. (b) Colloidal solution of CTAB-capped nanoparticles. (c) Hydrodynamic size and zeta potential. (d) FTIR spectra and (e) XRD patterns of CTAB-capped silver and gold nanoparticles.

cal shape and collective oscillation of free electrons on the nanoparticle surface. This phenomenon is known as localized surface plasmon resonance (LSPR), a characteristic feature of metallic nanoparticles such as gold and silver [35]. The length of the gold nanorods influences the LSPR [36]. The CTAB molecules on the shorter gold nanorods (20.8 ± 9.5 nm) are densely packed compared to longer nanorods (36.5 ± 7.3 nm). The high curvature of the nanorods leads to enhanced stabilization due to the larger inter-micellar channels generated on the flat side facets of the gold nanorods [37]. In comparison, the CTAB molecules on the longer nanorods are scattered over the side faces of the nanorods, which may lead to aggregation. Changes in pH or ionic strength are also capable of decreasing the CTAB binding to surfaces of longer gold nanorods. Therefore, longer nanorods are more prone to aggregation than shorter rods. The packing density of CTAB is also reported to be a factor that controls the size of metal nanoparticles [38]. The isotropic gold nanospheres exhibit an equal distribution of CTAB on the surfaces due to the isotropic geometry. The amount of CTAB is critical in determining the functional aspects of the metal nanospheres or nanorods.

Hydrodynamic radius, polydispersity, and surface charge of the synthesized CTAB-capped nanoparticles were measured as shown in Figure 2c. The DLS measurement indicated average hydrodynamic radii of 35.80 and 29.60 nm for isotropic silver and gold nanospheres, respectively. DLS measurements of anisotropic nanorods (AuNR1 and AuNR2) could not be carried out because of limitations of the instrument [39]. The nanospheres of silver and gold showed good PDI values of 0.123 and 0.249 for silver and gold nanospheres, respectively (Figure 2c). The very low PDIs prove that the nanospheres are monodisperse and non-aggregated. A PDI of less than 0.3 typically indicates a relatively narrow and well-controlled size distribution [40]. CTAB forms a monolayer around the nanoparticles, providing a consistent and uniform surface coverage. This uniformity in surface passivation contributes to the narrow size distribution of the particles. The long hydrocarbon tails of the CTAB molecules extending from the nanoparticle surface create steric repulsive forces between the particles. This repulsion prevents particles from getting too close to each other, thus minimizing aggregation.

The CTAB-capped AgNS, AuNS, AuNR1, and AuNR2 showed positive zeta potential values of 30.2 ± 4.3, 30.9 ± 9.6, 36.2 ± 9.6, and 31.9 ± 9.1 mV, respectively (Figure 2c). Zeta potential values beyond −30 mV and +30 mV indicate excellent colloidal stability due to strong repulsive forces among the nanoparticles [41]. The positive zeta potential values are caused by the having positively charged head groups of CTAB mole-

cules, which are attracted to the negatively charged surfaces of the metal nanoparticles and form a cationic layer around them [28].

CTAB-AgNS, CTAB-AuNS, CTAB-AuNR1, and CTAB-AuNR2 were analyzed for functional group identification using FTIR (Figure 2d). CTAB contains a long alkyl chain that typically results in peaks at 2920 and 2850 cm^{-1} in the FTIR spectrum. These peaks correspond to the symmetric and antisymmetric stretching vibrations of alkyl C–H bonds [28]. CTAB-capped gold and silver nanoparticles exhibit peaks at the same wavenumber as the parent compound, but with different intensities (Figure 2d). The doublet at 1462 and 1472 cm^{-1} obtained from CTAB is attributed to the CH_2 scissoring mode and indicates close-packing of the methylene chains [42]. However, for CTAB-AgNS, CTAB-AuNS, CTAB-AuNR1, and CTAB-AuNR2, the peak splits into two parts with different intensities because of crystallinity loss in the hydrocarbon regions or the morphology of the nanoparticles. The singlets at 962 cm^{-1} for parent CTAB and 946 cm^{-1} for CTAB-AgNS correspond to $C–N^+$ stretching bands, and the shift in wavenumber might be due to the interaction between the N-containing amino group and the silver metal surface [28]. However, the peak did not shift in the case of gold nanoparticles (AuNS, AuNR1, and AuNR2). The characteristic [C–H–Ag] vibration was missing, indicating the absence of C–H binding to the metal surface. The new minor peaks of CTAB-capped AgNS and AuNS at 828, 1004, and 1130 cm^{-1}, which are not present in parent CTAB molecules, are also considered as stretching of $C–N^+$ affected by the metal surface, as described by Nikoobakht and El-Sayed for CTAB-capped gold nanoparticles [43]. The singlet at 730 cm^{-1} for parent (powder) CTAB and CTAB-capped nanoparticles is due to CH_2 rocking. The broad band at 3390 cm^{-1} in parent CTAB corresponds to N–H stretching, which is shifted to 3315 cm^{-1} after binding to the gold and silver nanoparticles. The overlap between peaks of parent CTAB with those of CTAB-capped metal nanoparticles indicates the successful capping of the nanoparticle surface without compromising their structural property.

To determine the crystalline structure of the synthesized silver and gold nanoparticles, silver and gold nanospheres capped with CTAB were measured with XRD (Figure 2e). The most common crystal structure of gold and silver in nanoparticles is face-centered cubic (FCC). In the XRD pattern of FCC CTAB-AuNS, we observe major diffraction peaks at around 38.2°, 44.1°, 64.5°, and 77.4°, corresponding to the (111), (200), (220), and (311) planes, respectively [42]. In the case of CTAB-AgNS, we observe major peaks at 38.1°, 44.3°, 64.4°, and 77.5°, corresponding to the (111), (200), (220), and (311) planes [44]. However, we also observed two minor peaks at 55.04° and 73.14°, which correspond to the (220) and (311) planes; these were also observed in other studies with CTAB-capped silver nanoparticles [44]. These peaks might be related to the formation of AgO in the nanoparticles, which is reported elsewhere [44].

Transmission electron microscopy (TEM) enables precise nanoparticle size and shape measurements. TEM images show that AuNR1 and AuNR2 have a rod-like shape with different sizes, whereas AuNS and AgNS are spherical (Figure 3a–d). The mean sizes of CTAB-AgNS and CTAB-AuNS are 27.4 ± 4.6

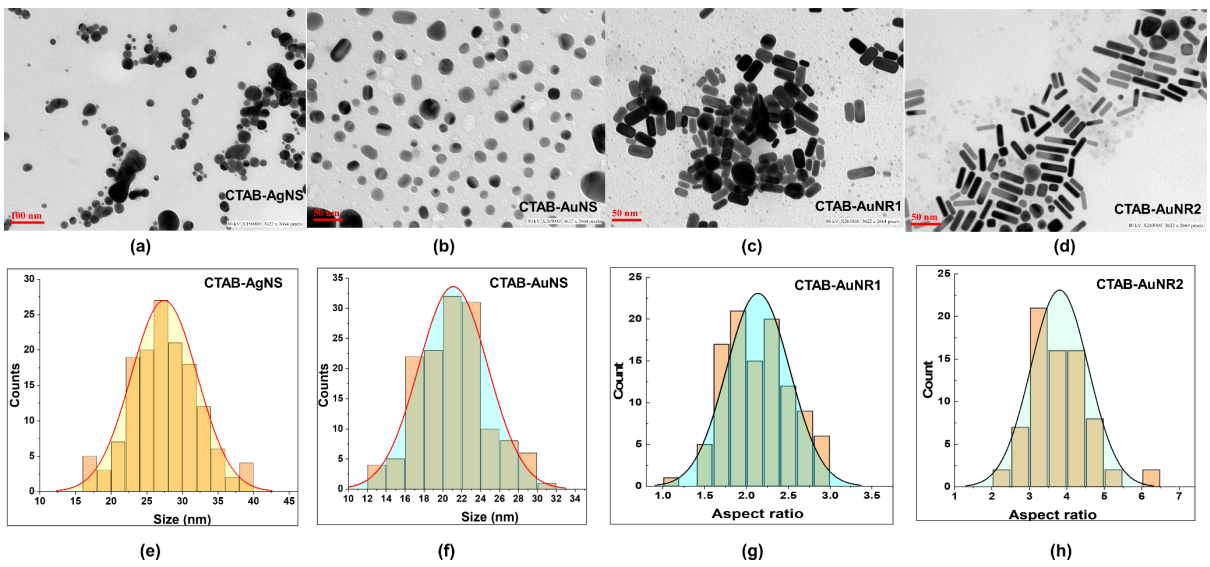


Figure 3: TEM images and mean size distribution of (a, e) CTAB-AgNS, (b, f) CTAB-AuNS. TEM images and aspect ratio histograms of (c, g) CTAB-AuNR1 and (d, h) CTAB-AuNR2. The average size for each sample was calculated from 100 individual nanoparticles.

and 21.1 ± 3.6 nm, respectively (Figure 3e and 3f). The mean average lengths of CTAB-AuNR1 and CTAB-AuNR2 were 20.76 ± 9.5 and 36.54 ± 7.3 nm, respectively. Also, there was a change in aspect ratio from 2.1 ± 0.3 to 3.8 ± 0.7 for AuNR1 and AuNR2, respectively (Figure 3g,h). Figure 3c and 3d show different sizes of nanorods for both AuNR1 and AuNR2 with 81.4% and 82.0% population, respectively. A total of 100 nanoparticles from each sample was considered for the measurements of average size.

Quantification of CTAB using UHPLC on nanoparticle surface

The quantity of CTAB on the nanoparticle surface was determined through an indirect approach wherein CTAB-capped metal nanoparticles underwent centrifugation, and the resulting supernatant was collected. The CTAB content in the supernatant was quantified using the developed UHPLC method. Subsequently, the remaining CTAB on the nanoparticles' surface was calculated by subtracting the collected CTAB amount from the initial quantity provided to the reaction mixture. In UHPLC, a peak at 208 nm, with a retention time of 0.8–0.9 min, was observed in the CTAB standard, utilizing a PDA detector within a linear range of 0.625–20 µg/mL. This standard was further applied to confirm and quantify CTAB in the nanoparticle supernatant (Supporting Information File 1, Figure S1). During sample analysis, a similar peak was consistently observed in all CTAB-capped nanoparticle supernatants, appropriately diluted within the linear range. The final concentrations of CTAB in CTAB-capped AgNS, AuNS, AuNR1, and AuNR2 were found to be 5612, 30400, 31020, and 30655 µg/mL. After centrifugation, the CTAB content in the obtained supernatant was 4756, 15940, 17200, and 18340 µg/mL, as indicated in Table 1. Consequently, the CTAB remaining on CTAB-AgNS, CTAB-AuNS, CTAB-AuNR1, and CTAB-AuNR2 surfaces was determined to be 856.30, 14460, 13820, and 12315 µg/mL, respectively. Gold nanoparticles exhibit a higher amount of bound CTAB than silver nanoparticles.

Impact of NaCl and NaOH on CTAB-capped nanoparticles

The stability and dispersibility of the CTAB-capped metal nanoparticles were assessed in 1 M NaOH and NaCl. NaOH or NaCl may lead to the desorption of CTAB from the metal surface, which plays a key role in detecting heavy metal ions. The addition of various volumes of NaOH to the metal nanoparticles of different concentrations (OD of 0.5 ± 0.1 and 1.0 ± 0.1) resulted in both colorimetric and spectrophotometric detection of heavy metal ions. The different sets 1–8 represent CTAB-AgNS, CTAB-AuNS, CTAB-AuNR1 and CTAB-AuNR2, each with 0.5 ± 0.1 and 1.0 ± 0.1 OD. As-prepared and centrifuged nanoparticles were tested to assess their stability in NaOH (5–50 µL) and NaCl. Centrifuged CTAB-$AgNS_{0.5}$ (set 1) shows NaOH volume-dependent aggregation of the silver nanospheres (Figure 4a). The peak flattening of centrifuged $AgNS_{0.5}$ from 20 µL NaOH (set 1, C–F) onward confirmed nanoparticle aggregation, leading to colorimetric differences compared to the control (Figure 4a).

In contrast, centrifuged $AgNS_{1.0}$ (set 2) was highly stable in NaOH up to 50 µL (A–F) compared to $AgNS_{0.5}$ (Figure 4a). This stability is attributed to the increased nanoparticle concentration and the amount of CTAB. A similar trend was observed in the case of as-prepared $AgNS_{0.5}$ (set 1) and $AgNS_{1.0}$ (set 2) (Figure 4b). However, the intensity of as-prepared $AgNS_{0.5}$ decreases with 50 µL NaOH, evident by a color change (Figure 4b). The stability of centrifuged and as-prepared $AgNS_{1.0}$ give a clear indication that nanoparticles with higher concentrations are stable in NaOH, which is not observed in the case of centrifuged and as-prepared $AgNS_{0.5}$. In a study by Yadav et al., NaOH (0.1 N) induced a hyperchromic effect in silver nanoparticles, which was not observed in our case [45]. In our study, no plasmonic shift was observed, but a slight decrease in intensity at lower concentrations of silver nanoparticles might be due to the strong capping of CTAB on the nanoparticles' surface. Apart from nanoparticle concentration, the amount of the capping agent on the surface of nanoparticles plays a significant role in providing stability, as reported elsewhere [3]. The concentration of CTAB that remained on silver nanoparticles after centrifugation was significantly reduced (Table 1). However, the role of the capping agent is not limited to stability; it also enhances the application potential of nanoparticles in the presence of NaOH. Gold nanoparticles are highly stable compared to silver nanoparticles, as silver nanoparticles are prone to oxidation [46].

Table 1: Quantification of CTAB using the UHPLC method.

Sample	CTAB added (µg/mL)	CTAB obtained (µg/mL)	CTAB bound on nanoparticles (µg/mL)	Binding efficiency (%)
CTAB-AgNS	5612	4756 ± 34	856.30	15.25%
CTAB-AuNS	30400	15940 ± 124	14460	47.56%
CTAB-AuNR1	31020	17200 ± 100	13820	44.55%
CTAB-AuNR2	30655	18340 ± 61	12315	40.17%

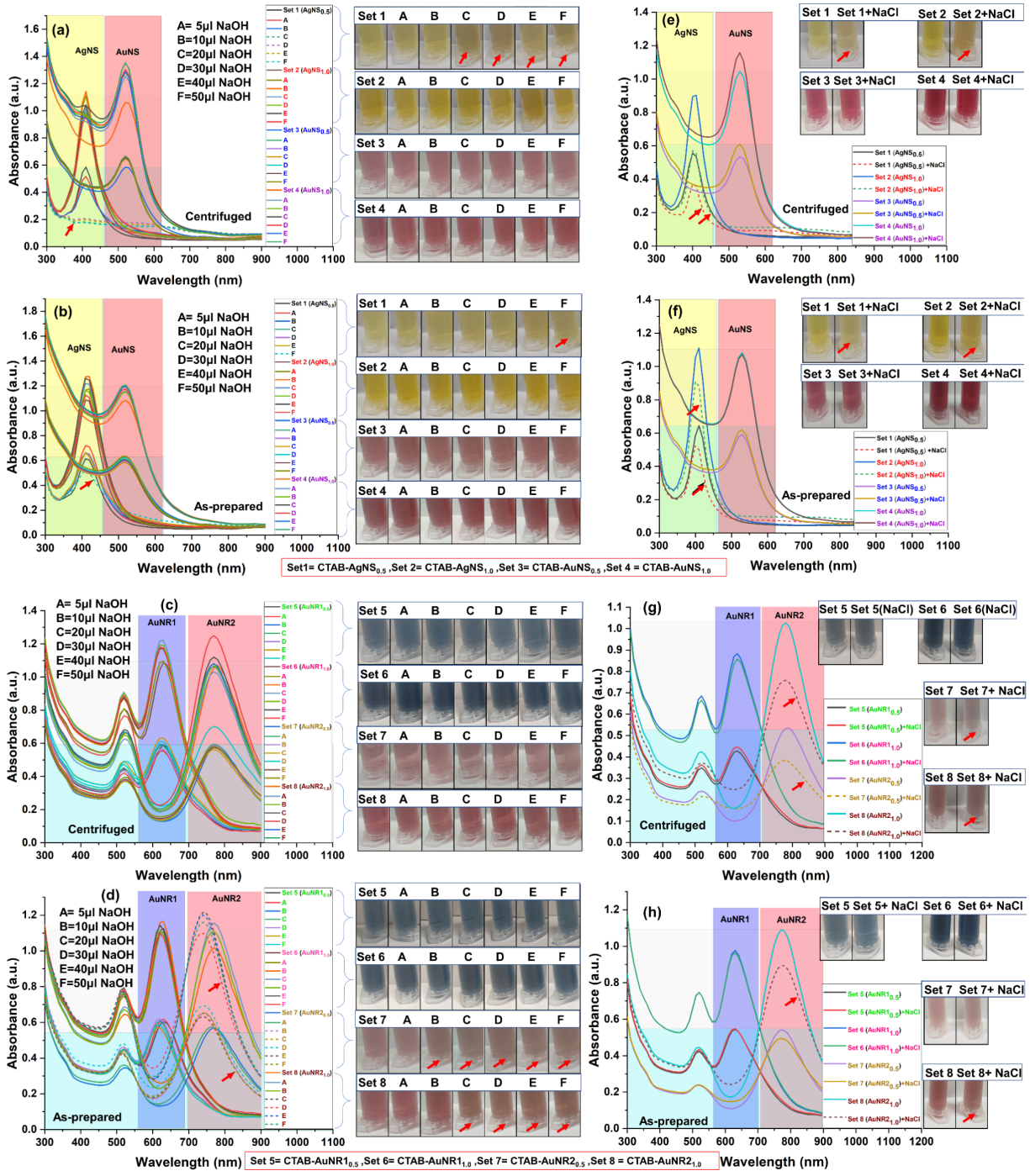


Figure 4: Impact of NaOH and NaCl on as-prepared/centrifuged CTAB-capped nanoparticles. (a, b) NaOH impact on centrifuged and as-prepared isotropic CTAB-capped nanoparticles ($AgNS_{0.5}$, $AgNS_{1.0}$, $AuNS_{0.5}$, and $AuNS_{1.0}$). (c, d) NaOH impact on centrifuged and as-prepared anisotropic CTAB-capped nanoparticles ($AuNR1_{0.5}$, $AuNR1_{1.0}$, $AuNR2_{0.5}$ and $AuNR2_{1.0}$). (e, f) NaCl impact on centrifuged and as-prepared isotropic CTAB-capped nanoparticles ($AgNS_{0.5}$, $AgNS_{1.0}$, $AuNS_{0.5}$ and $AuNS_{1.0}$). (g, h) NaCl impact on centrifuged and as-prepared anisotropic CTAB-capped nanoparticles ($AuNR1_{0.5}$, $AuNR1_{1.0}$, $AuNR2_{0.5}$ and $AuNR2_{1.0}$). The images attached with spectral absorbance show the color change upon adding NaOH and NaCl. The subscripts 0.5 and 1.0 represent the nanoparticle concentration in OD. Sets 1–8 correspond to nanoparticles $AgNS_{0.5}$, $AgNS_{1.0}$, $AuNS_{0.5}$, $AuNS_{1.0}$, $AuNR1_{0.5}$, $AuNR1_{1.0}$, $AuNR2_{0.5}$, and $AuNR2_{1.0}$ respectively. A, B, C, D, E, and F mean NaOH volumes of 5, 10, 20, 30, 40, and 50 µL, respectively, added to the nanoparticles. The short dashed line shows the change in the sample compared to the control (marked by an arrow). The first centrifuge tube in each colorimetric panel represented as control for that panel.

Interestingly, the centrifuged/as-prepared CTAB-$AuNS_{0.5}$ (set 3) and $AuNS_{1.0}$ (set 4) showed no plasmonic change upon the addition of different volumes of NaOH (Figure 4a,b). Also, no significant difference in the color of AuNS was observed (Figure 4a,b). This might be because the amount of CTAB on the gold nanospheres is significantly higher than on silver nanoparticles in both centrifuged and as-prepared samples (Table 1). This suggests that the nature of the metal and the strong capping in nanoparticles are also crucial for their enhanced stability in NaOH. In addition, the shape-dependent impact of nanoparticle stability in NaOH was evaluated using gold nanorods (AuNRs) of two different lengths.

$AuNR1_{0.5}$ (set 5), $AuNR1_{1.0}$ (set 6), $AuNR2_{0.5}$ (set 7), and $AuNR2_{1.0}$ (set 8) showed no plasmonic and colorimetric changes in the presence of NaOH (Figure 4c). The as-prepared $AuNR2_{0.5}$ and $AuNR2_{1.0}$ showed a blueshift of plasmons along with a color change in the presence of more than 10 µL and 20 µL NaOH, respectively. In contrast, AuNR1 at both OD did not show any significant changes (Figure 4d). These results revealed that longer gold rods in the as-prepared state show a blueshift of plasmons due to the easy desorption of CTAB in the presence of NaOH, which is not observed in the case of small gold nanorods and nanospheres. The CTAB is tightly packed on short nanorods and nanospheres [43]. It was reported that NaOH significantly alters the micelles of quaternary ammonium surfactants [47]. This ultimately affects the capping ability of CTAB, thus providing a platform for interaction with the ligand. Furthermore, the nanoparticles designed for sensing applications should have higher ionic strength, which provides them the capability for heavy metal sensing in real scenarios. To determine the ionic strength of the synthesized nanoparticles, their stability in ionic salts, such as NaCl, must be evaluated. Centrifuged/as-prepared CTAB-$AgNS_{0.5}$ and $AgNS_{1.0}$ show a decrease in the plasmonic intensity of nanoparticles and a change in color in the presence of NaCl (Figure 4e,f). However, no flattening or aggregation of silver nanoparticles was noticed (Figure 4e,f). The decrease in the intensity of silver nanoparticles might be due to less CTAB on the nanoparticles' surface or a decrease in CTAB CMC value. As reported elsewhere, the reduction in CTAB CMC is associated with NaCl concentration [48]. Centrifuged and as-prepared $AuNS_{0.5}$ and $AuNS_{1.0}$ showed no absorbance or colorimetric change in the presence of NaCl (Figure 4e,f).

Similarly, centrifuged and as-prepared AuNR1s ($AuNR1_{0.5}$ and $AuNR1_{1.0}$) showed no changes in plasmon frequency or color of the nanoparticles in the presence of NaCl (Figure 4g,h). Although centrifuged and as-prepared $AuNR2_{0.5}$ and $AuNR2_{1.0}$ showed a noticeable difference in the absorption spectrum compared to the control (Figure 4g,h). Previously, several reports confirmed the use of NaOH and NaCl in nanoparticle synthesis or surface modification for different applications. This experimental study demonstrated that CTAB-capped isotropic and anisotropic nanoparticles are stable in NaOH and NaCl and will be used for further sensing applications. In comparison with other studies, the synthesized nanoparticles are stable at higher concentrations of NaCl and NaOH. The colloidal stability of nanoparticles represents the initial step towards designing them as environmental heavy metal detection probes.

Detection of heavy metals

Isotropic CTAB-capped AgNS and AuNS

A range of heavy metals, specifically As^{3+}, Al^{3+}, Cd^{2+}, Zn^{2+}, Hg^{2+}, Ni^{2+}, Cu^{2+}, Cr^{3+}, Pb^{2+}, Fe^{3+}, and Co^{2+}, each with a concentration of 1 ppm, was examined. The isotropic CTAB-capped AgNS and AuNS were used to detect heavy metals without NaOH. Centrifuged CTAB-$AgNS_{0.5}$ detected Hg^{2+} and Fe^{3+} based on changes in color and spectral absorbance compared to the control (Figure 5a).

Surprisingly, no metal detection was observed with centrifuged $AgNS_{1.0}$ (Figure 5a). This might be due to the non-availability of binding sites for metals on the surface of silver nanoparticles, as CTAB is tightly bound to the isotropic nanoparticles as discussed earlier. However, as-prepared CTAB-$AgNS_{0.5}$ and $AgNS_{1.0}$ sensed Hg^{2+} and Cu^{2+} without NaOH (Figure 5b). The decrease in plasmonic intensity of as-prepared $AgNS_{0.5}$ and $AgNS_{1.0}$ in the presence of Hg^{2+} and Cu^{2+} leads to a colorimetric change (Figure 5b). This suggests the interaction of as-prepared CTAB-capped silver nanoparticles with Cu^{2+} and Hg^{2+}, regardless of their concentration. The capping provides metal selectivity, whereas bare $AgNS_{1.0}$ (without capping) showed unspecific metal detection such as Cd^{2+}, Zn^{2+}, Hg^{2+}, Ni^{2+}, Cu^{2+}, Cr^{3+}, Pb^{2+}, Fe^{3+}, and Co^{2+} (Figure 5d). However, in another study, only Hg^{2+} was detected with silver nanoparticles capped with poly(allylamine) hydrochloride but stabilized using CTAB [49]. Also, no prominent metal detection was achieved after adding NaOH to as-prepared CTAB-$AgNS_{0.5}$ and $AgNS_{1.0}$, confirming no interaction between metal and nanoparticles (Supporting Information File 1, Figure S2 and Figure S3). The as-prepared CTAB-AgNS contains 5612 µg/mL CTAB, which changes in the case of centrifuged CTAB-AgNS to 856 µg/mL. Despite less CTAB on the silver nanoparticle surface, they showed excellent sensing capability even at lower nanoparticle concentration. The addition of NaOH (5–50 µL) to centrifuged CTAB-AgNS led to no selectivity toward metal detection with centrifuged $AgNS_{1.0}$, while aggregation of the particles was observed for $AgNS_{0.5}$ starting from 20 µL of NaOH (Figure S4 and Figure S5, Supporting Information File 1). These results reveal that the as-prepared CTAB $AgNS_{0.5}$ and $AgNS_{1.0}$ and centrifuged $AgNS_{0.5}$ selec-

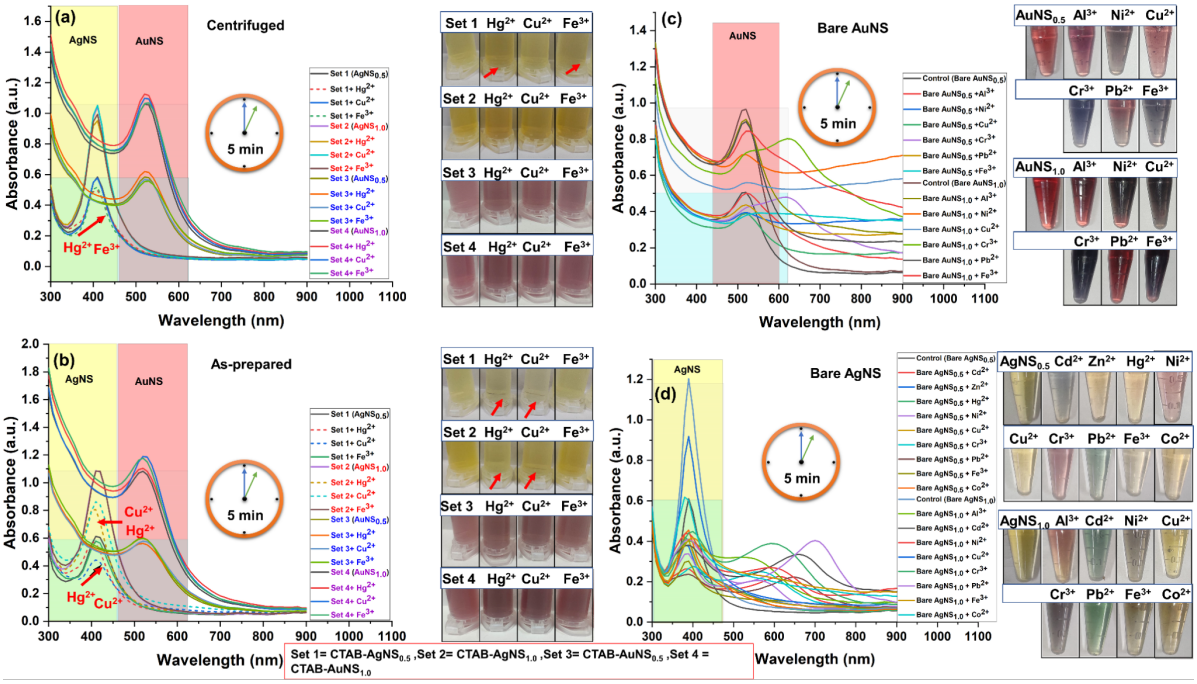


Figure 5: Spectrophotometric and colorimetric detection of heavy metals using centrifuged/as-prepared isotropic metal nanoparticles in the absence of NaOH. (a) Detection of Hg^{2+} and Fe^{3+} using centrifuged $AgNS_{0.5}$, while $AgNS_{1.0}$, $AuNS_{0.5}$, and $AuNS_{1.0}$ did not detect the metals. (b) Detection of Hg^{2+} and Cu^{2+} using as-prepared $AgNS_{0.5}$ and $AgNS_{1.0}$, while $AuNS_{0.5}$, and $AuNS_{1.0}$ did not detect the metals. (c) Detection of Al^{3+}, Ni^{2+}, Cu^{2+}, Cr^{3+}, Pb^{2+}, and Fe^{3+} using bare AuNS. (d) Detection of Al^{3+}, Cd^{2+}, Zn^{2+}, Hg^{2+}, Ni^{2+}, Cu^{2+}, Cr^{3+}, Pb^{2+}, Fe^{3+}, and Co^{2+} using silver nanospheres ($AgNS_{0.5}$ and $AgNS_{1.0}$). The subscripts 0.5 and 1.0 represent the nanoparticles concentration in terms of optical density. Sets 1–4 correspond to nanoparticles $AgNS_{0.5}$, $AgNS_{1.0}$, $AuNS_{0.5}$, and $AuNS_{1.0}$ respectively. The short dashed line shows the change in the sample compared to the control (marked by an arrow). The first centrifuge tube in each colorimetric panel represented as control for that panel.

tively detect heavy metals in the absence of NaOH, while centrifuged $AgNS_{1.0}$ showed interaction with multiple metals because of more particles with less CTAB than as-prepared particles. The bare/uncapped $AgNS_{0.5}$ and $AgNS_{1.0}$ detected various metals (Figure S10, Supporting Information File 1).

Gold nanoparticles with similar capping and size were considered to determine the role of surface capping in heavy metal detection. Interestingly, as-prepared and centrifuged CTAB-$AuNS_{0.5}$ and $AuNS_{1.0}$ showed no interaction with heavy metals without NaOH (Figure 5a,b). No metal ions were detected with as-prepared/centrifuged $AuNS_{0.5}$ and $AuNS_{1.0}$ in the absence and presence of NaOH (Figures S6–S9, Supporting Information File 1). However, bare AuNS detected various metals including Al^{3+}, Ni^{2+}, Cu^{2+}, Cr^{3+}, Pb^{2+}, and Fe^{3+} (Figure 4c and Figure S10, Supporting Information File 1). The concentrations of CTAB in as-prepared and centrifuged AuNS are 30400 and 14460 µg/mL, respectively, which is far more than in silver nanoparticles. Silver nanoparticles interact with other metals because of their strong redox potential and the lower amount of CTAB [9]. The nanoparticle shape is also a criterion for designing nanoparticles as sensing probes. Therefore, we also assessed the potential of CTAB-capped gold nanorods (AuNR) as sensing probes for detecting heavy metals.

Anisotropic CTAB-capped gold nanorods

CTAB-$AuNR1_{0.5}$ interacted with three metal ions, namely Ni^{2+}, Cr^{3+}, and Co^{2+}, as evident through spectrophotometric and colorimetric differences compared to the control in the presence of 5–10 µL NaOH (Figure 6a,b).

The interaction of $AuNR1_{0.5}$ with Hg^{2+} leads to a slight blueshift (no prominent color change), while redshifts were observed with other metals compared to the control (Supporting Information File 1, Figure S11). As discussed in previous sections, NaOH plays a significant role in decreasing the amount of CTAB on the nanoparticles, thus providing binding sites to the metal ions. The interaction with Hg^{2+} was also evident in as-prepared and centrifuged CTAB-AgNS. Placido et al. demonstrated Hg^{2+} detection using L-cysteine-functionalized CTAB-AuNR [50]. However, multiple metals were detected, including Hg^{2+}, without surface functionalization using NaOH (5–10 µL). After increasing the added amount of NaOH to 20–50 µL, centrifuged $AuNR1_{0.5}$ selectively inter-

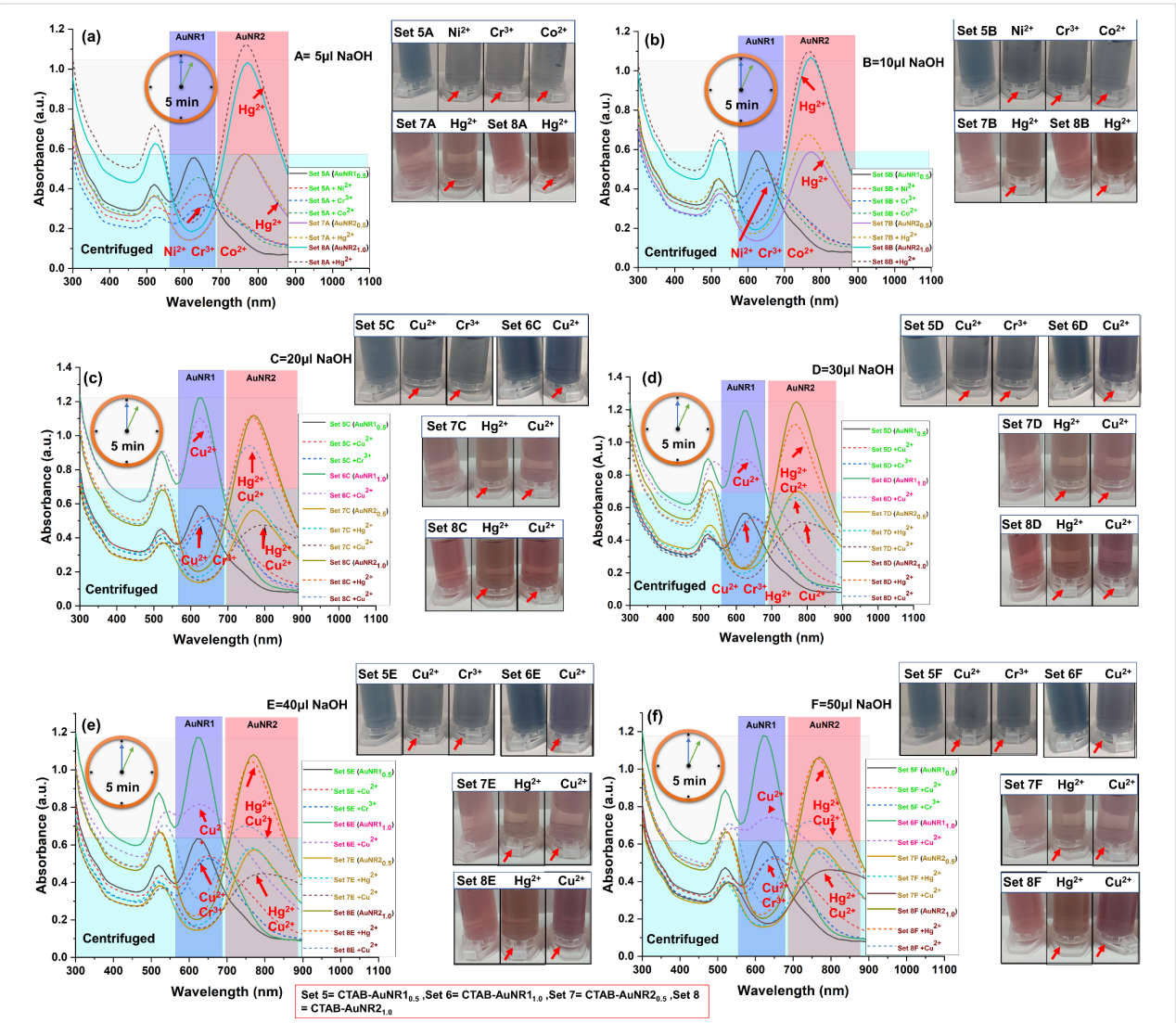


Figure 6: Spectrophotometric and colorimetric detection of heavy metals using centrifuged CTAB-AuNR1 and AuNR2 in the presence of NaOH. (a) AuNR1$_{0.5}$ (set 5) and AuNR2$_{0.5/1.0}$ (set 7 and set 8) detect Ni^{2+}, $Cr^{3+}$and Co^{2+}, and Hg^{2+} in the presence of 5 µL NaOH (A). (b) AuNR1$_{0.5}$ (set 5) and AuNR2$_{0.5/1.0}$ (set 7 and set 8) detect Ni^{2+}, $Cr^{3+}$and Co^{2+}, and Hg^{2+} in the presence of 5 µL NaOH (B); (c–f) AuNR1$_{0.5/1.0}$ (set 5 and set 6) and AuNR2$_{0.5/1.0}$ (set 7 and set 8) detect Cu^{2+}, Cr^{3+}, and Hg^{2+} in the presence of 20, 30, 40, and 50 µL of NaOH (C–F). The subscripts 0.5 and 1.0 represent the nanoparticle concentration in terms of optical density. Sets 5–8 correspond to nanoparticles AuNR1$_{0.5}$, AuNR1$_{1.0}$, AuNR2$_{0.5}$ and AuNR2$_{1.0}$, respectively. A, B, C, D, E, and F mean added NaOH volumes of 5, 10, 20, 30, 40, and 50 µL, respectively. The short-dashed line shows the change in the sample compared to the control (marked by an arrow). The first centrifuge tube in each colorimetric panel represented as control for that panel.

acted with Cu^{2+} and Cr^{3+} with prominent color and spectral changes (Figure 6c–f). The metal selectivity switched upon increasing the volume of NaOH, confirming the significant role of NaOH in designing the nanoparticle-based sensor. Selective metal detection using centrifuged AuNR1$_{0.5}$ was achieved among all metals in the presence of NaOH only (Supporting Information File 1, Figure S11). Centrifuged CTAB-AuNR1$_{0.5}$ without NaOH showed no metal detection (Supporting Information File 1, Figure S11). Apart from the amount of added NaOH, the nanoparticle concentration in terms of OD also plays a significant role in the nanoparticle–metal interactions. Increasing the nanoparticle concentration, centrifuged AuNR1$_{1.0}$ detected only copper (Cu^{2+}) upon adding NaOH (30–50 µL) to the nanoparticles of 1 OD (Figure 6d–f). The colorimetric changes could be observed by the naked eye (Figure 6d–f). There were no visual differences in the centrifuged AuNR1$_{1.0}$ plasmonic absorbance in the absence and presence of NaOH (5–20 µL) (Supporting Information File 1, Figure S12). Color or plasmon band changes can be attributed to nanoparticle–metal interactions [51]. Other researchers also explored the role of NaOH; they found that NaOH is a potent molecule that helps to remove CTAB from nanoparticles by reducing the CMC [33]. Indeed, the lower nanoparticle concentration (0.5 OD) provides high interaction due to the availability of

fewer particles and less amount of CTAB on their surface compared to 1 OD with the same metal concentration (1 ppm). The concentrations of CTAB in as-prepared and centrifuged AuNR1 are 31020 and 13820 μg/mL, respectively. Thus, nanoparticle concentration also played a significant role in designing the detection system for heavy metals.

Centrifuged CTAB-AuNR2$_{0.5}$ and AuNR2$_{1.0}$ spectrophotometrically detected Hg^{2+} with 5–10 μL NaOH (Figure 6a,b). The results obtained with centrifuged CTAB-AuNR2$_{0.5}$ and AuNR2$_{1.0}$ were nearly the same as for centrifuged CTAB-AuNR1$_{0.5}$ with Hg^{2+}. However, in the case of centrifuged CTAB-AuNR2$_{0.5}$, Hg^{2+} shows a prominent color change compared to centrifuged AuNR1$_{0.5}$. The detection of Hg^{2+} is also obtained with centrifuged CTAB-AgNS$_{0.5}$, but centrifuged CTAB-AuNS$_{0.5}$ did not detect any metal ions. A subtle change in capping concentration on AuNR1 and AuNR2 was observed due to their length (Table 1). The change in concentration or size of nanorods ultimately affects the sensitivity towards metal ion detection. The metal selectivity was observed for all metal ions (Supporting Information File 1, Figure S13). With increasing nanoparticle concentration, centrifuged CTAB-AuNR2$_{1.0}$ and AuNR2$_{0.5}$ detected Hg^{2+} and Cu^{2+} with 20–50 μL NaOH (Figure 6c–f). The metal selectivity was changed upon increasing the NaOH volume and concentration of nanoparticles, as also observed for the shorter nanorods. The mechanism is similar to the interaction of metals with longer nanorods. However, the change in metal selectivity is due to the size of nanorods. In NaOH absence, no metal shows prominent interaction with centrifuged CTAB-AuNR2$_{1.0}$ and AuNR2$_{0.5}$ (Supporting Information File 1, Figure S13 and Figure S14). The absence of NaOH and no metal detection indicate a strong binding of CTAB on the nanoparticles' surface. Therefore, it is certain that a minimum amount of NaOH is required to weaken the binding of CTAB without hampering the nanoparticles' sensing abilities. Furthermore, the higher CTAB concentration in as-prepared samples was also evaluated to confirm metal selectivity. The concentrations of CTAB in as-prepared and centrifuged CTAB-AuNR2 are 30655 and 12315 μg/mL, respectively; the longer nanorods have a lower amount of bound CTAB. However, in the case of as-prepared samples, nearly the same amount of CTAB is present.

In addition to this, the as-prepared CTAB-AuNR1 and CTAB-AuNR2 were also evaluated regarding heavy metal detection. Although the nanoparticle concentration has a big impact, washing nanoparticles is crucial in detecting heavy metals. As-prepared nanoparticles of the same concentration and size were evaluated to understand the impact of washing. As-prepared AuNR1 at 0.5 and 1 OD did not detect any metal through significant changes in color or plasmon resonance (Supporting Information File 1, Figure S15 and Figure S16). However, a slight blueshift of as-prepared CTAB-AuNR1$_{0.5}$ was observed with Hg^{2+} only in the presence of various amounts (10–50 μL) of NaOH (Supporting Information File 1, Figure S15). This is evident by the blueshift of the plasmonic peak by 10 nm compared to the control samples. However, no prominent color change was observed (Supporting Information File 1, Figure S15). This is due to the excess CTAB on as-prepared AuNR1, which does not allow for interaction with metals. Only Hg^{2+} showed interaction, as observed in CTAB-AgNS, where the concentration of CTAB is much lower than in CTAB-AuNR1. Similarly, no heavy metal interaction is possible in the case of CTAB-AuNS due to tightly bound CTAB. However, in the case of CTAB-AuNR1, CTAB is tightly bound to the flat side and show an intermicellar gap at the curvature. The curvature allows for metal interaction only after adding a specific amount of NaOH. The nanoparticles (as-prepared AuNR1$_{0.5}$ and AuNR1$_{1.0}$) without NaOH showed no metal detection (Supporting Information File 1, Figure S15 and Figure S16). The robust nature of CTAB on nanoparticle surfaces is well known, thus resisting the interaction with target molecules without surface modification. In our case, NaOH was used to weaken CTAB micelles without hampering the physicochemical properties of the synthesized nanoparticles. This weakening of CTAB solves the persistent problem of surface modification or the use of linker molecules with CTAB-capped nanoparticles for sensing applications. In addition, the nanorod size might be crucial regarding nanorod–metal interactions. In a previous study conducted by Xu et al., Cu^{2+} was detected with cysteine-functionalized CTAB-AuNR (λ_{max} 800 nm), while Hg^{2+} was detected with cysteine-functionalized CTAB-AuNR (λ_{max} 650 nm) [50,52]. Both L-cysteine-functionalized CTAB-AuNR detected different metals. Thus, it was confirmed that the size of the nanoparticles is a critical parameter influencing the physical and chemical properties of gold nanoparticles. The current study also evaluated size-dependent metal sensing using longer gold nanorods with the help of NaOH. Upon the addition of a specific volume of NaOH, the absorption band of CTAB-AuNR2 was blueshifted (λ_{max} 770 ± 5 nm to 740 ± 5 nm). The shifted peak of CTAB-AuNR2 was used as a control for further heavy metal sensing experiments because no aggregation was observed. As-prepared CTAB-AuNR2$_{0.5}$ interacted only with Hg^{2+} with a prominent blueshift of the plasmonic peak after addition of 10–50 μL of NaOH (Figure 7b–f). The present study demonstrated that merely altering the parameters of nanorods is sufficient for the detection of heavy metals, eliminating the need for any additional linker or buffer.

As-prepared AuNR2$_{0.5}$ interacted with Ni^{2+}, Cu^{2+}, and Fe^{3+} metal ions in the presence of 5 μL NaOH (Figure 7a). However, no significant change in nanoparticles was observed in the

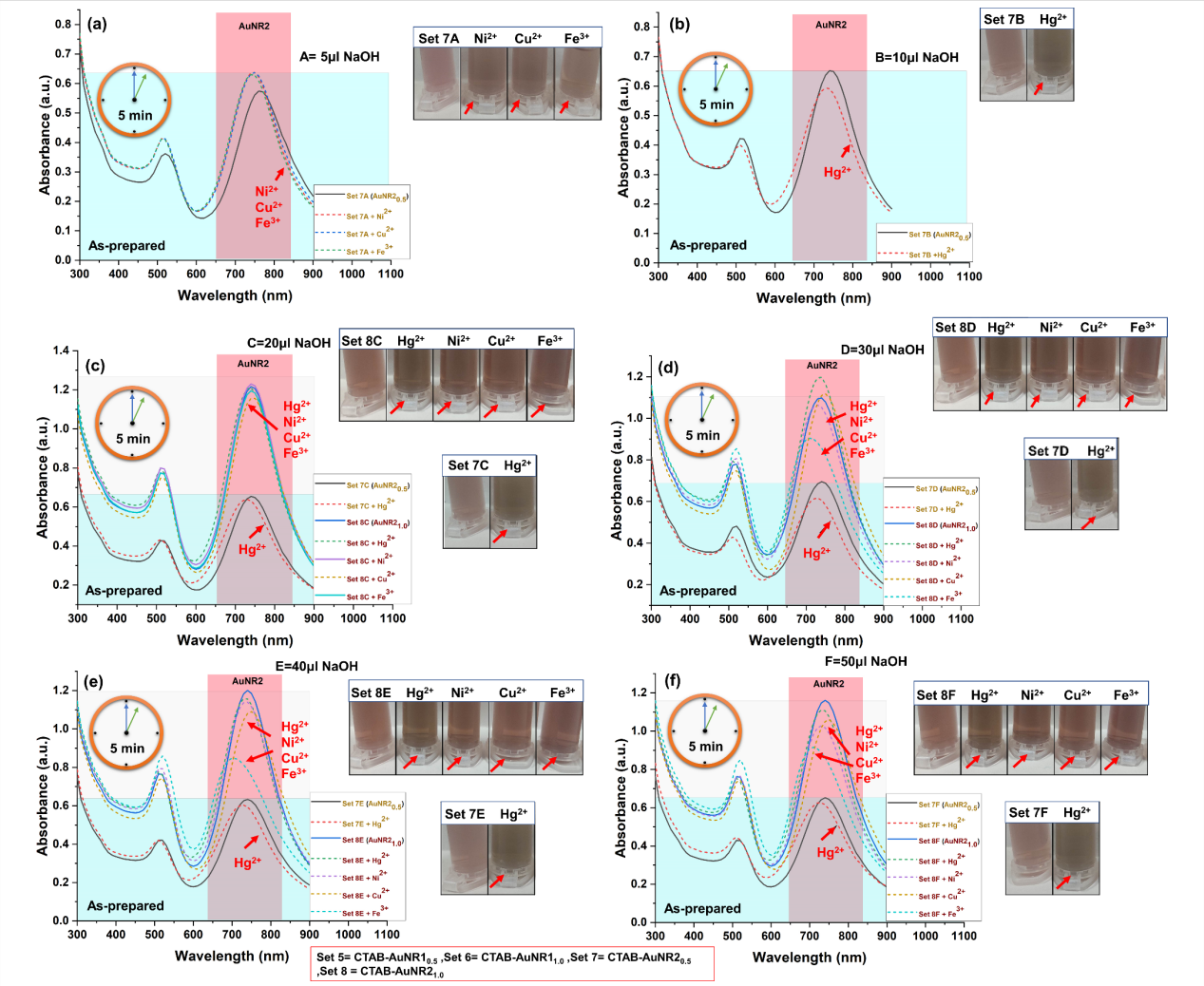


Figure 7: Spectrophotometric and colorimetric detection of heavy metals using as-prepared CTAB-AuNR2 in the presence of NaOH. (a) Only $AuNR2_{0.5}$ (set 7) detects Ni^{2+}, Cu^{2+}, and Fe^{3+} in the presence of 5 µL NaOH (A). (b) $AuNR2_{0.5}$ (set 7) detects Hg^{2+} in the presence of 10 µL NaOH (B). (c–f) $AuNR2_{0.5/1.0}$ (set 7 and set 8) detect Hg^{2+}, Ni^{2+}, Cu^{2+}, and Fe^{3+} in the presence of 20, 30, 40, 50 µL NaOH (C–F). The subscripts 0.5 and 1.0 represent the nanoparticle concentration in terms of optical density. Sets 5–8 correspond to nanoparticles $AuNR1_{0.5}$, $AuNR1_{1.0}$, $AuNR2_{0.5}$ and $AuNR2_{1.0}$, respectively. A, B, C, D, E, and F mean NaOH volumes of 5, 10, 20, 30, 40, and 50 µL, respectively, added to the nanoparticles. The short-dashed line shows the change in the sample compared to the control (marked by an arrow). The first centrifuge tube in each colorimetric panel represented as control for that panel.

absence of NaOH compared to the control (Supporting Information File 1, Figure S17). As-prepared CTAB-$AuNR2_{1.0}$ showed interaction with Hg^{2+}, Ni^{2+}, Cu^{2+}, and Fe^{3+} in the presence of 20–50 µL of NaOH with a prominent blueshift of the absorption band (Figure 7c–f). The metal selectivity changed in the case of as-prepared CTAB-$AuNR2_{1.0}$ compared to centrifuged $AuNR2_{1.0}$ and AuNR1, which might be due to the size of nanorods or shifting of the control sample peak upon the addition of NaOH. The as-prepared $AuNR2_{1.0}$ showed no plasmonic or colorimetric change with metal ions in the absence and presence of 5–20 µL NaOH (Figure 7a–c and Supporting Information File 1, Figure S18). The color and plasmon change confirmed the metal–nanoparticle interactions. Gold nanorods of two sizes (AuNR1 and AuNR2) detected different metals, suggesting that size, concentration, and centrifuged/as-prepared nanorods are critical parameters for designing a sensing probe for heavy metals. Shape and metal (with the same capping) were also evaluated for their role in heavy metal detection. Table 2 summarizes various studies on detecting heavy metals using CTAB-capped metal nanoparticles via linkers or buffers. Table 2 includes detected metals using as-prepared/centrifuged CTAB-capped AgNS, AuNS, AuNR1, and AuNR2.

Possible mechanism of heavy metal detection

Previous studies have established that CTAB prevents interactions with ligands such as metal ions. Consequently, alternative linkers have typically facilitated metal ion detection using CTAB-capped nanoparticles. However, this study has de-

Table 2: Studies related to CTAB-capped gold and silver nanoparticles for the detection of heavy metals.

CTAB-capped nanoparticles	Ligand/linker	Buffer	Metal detected	Reference
AgNP	poly(L-lysine)	—	Hg^{2+}	[9]
AuNS (λ_{max} 530 nm)	sodium thiosulfate	—	Pb^{2+}	[24]
AuNR (λ_{max} 650 nm)	L-cysteine	—	Hg^{2+}	[50]
AuNR (λ_{max} 801 nm)	cysteine	—	Cu^{2+}	[52]
AuNR (λ_{max} 655 nm)	*N*-alkylaminopyrazole ligand, 1-[2-(octylamino)ethyl]-3,5-diphenylpyrazole	—	Hg^{2+}	[53]
AuNR (λ_{max} 732 nm)	TPDT-silicate	—	Hg^{2+}	[54]
AuNR (λ_{max} 625 nm)	$Na_2S_2O_3$	NH_3/NH_4Cl buffers (pH 10.4)	Cu^{2+}	[55]
AuNR	—	hydrogen bromide buffer solution	Cu^{2+}	[56]
AuNR (λ_{max} 700 nm)	dithiothreitol (DTT)	—	As^{3+}	[57]
AuNR	L-arginine	—	Hg^{2+}	[58]
AgNS (λ_{max} 410 nm)	—	—	Hg^{2+}, Cu^{2+}, and Fe^{3+}	this work[a]
AuNS (λ_{max} 525 nm)	—	—	—	this work[a]
AuNR1 (λ_{max} 630 nm)	—	—	Cr^{3+}, Co^{2+}, Ni^{2+}, and Cu^{2+}	
AuNR2 (λ_{max} 770 nm)	—	—	Hg^{2+}, Ni^{2+}, Fe^{3+}, and Cu^{2+}	

[a]The metal detection depends on size, shape (isotropic and anisotropic), concentration (0.5 and 1 OD), and the nature (centrifuged or as-prepared) of the nanoparticles and the volume of added NaOH.

veloped a system capable of detecting metal ions without such linkers. The detection mechanism in this study is influenced by factors such as the amount of NaOH, nanoparticle shape, and nanoparticle concentration. As previously reported, CTAB-capped silver nanospheres detected Cu^{2+} and Hg^{2+}, attributed to the interaction between the metal ions and the nanoparticles. The underlying mechanism is based on the higher affinity of Hg^{2+} towards silver, with a binding energy of 1.78 eV [9]. This strong affinity allows Hg^{2+} ions to penetrate the CTAB bilayer, particularly in AgNS, where the amount of bound CTAB is lower [9]. Additionally, Cu^{2+} ions undergo a galvanic replacement reaction with silver, facilitated by their high redox potential, enabling Cu–Ag interaction in low-bound CTAB nanoparticles [59]. In contrast, gold nanospheres did not exhibit any metal interactions in the presence of NaOH, which is attributed to the tightly bound CTAB on AuNS surfaces. However, CTAB-AuNS was reported to detect Pb^{2+} in the presence of sodium thiosulfate due to the thiol group's higher affinity for metal ions [24]. Furthermore, the study found that AuNR1 and AuNR2 detected metals only in the presence of NaOH, possibly due to the removal of CTAB from the nanorod curvature, which is known to contain less CTAB. Centrifuged $AuNR1_{0.5}$ nanorods detected Cr^{3+}, Co^{2+}, Ni^{2+}, and Cu^{2+} with NaOH volumes of 5–10 µL. Upon increasing the NaOH volume, only Cr^{3+} and Cu^{2+} were detected with $AuNR1_{0.5}$ and $AuNR1_{1.0}$ nanorods. This suggests that NaOH plays a crucial role in facilitating nanorod–metal interactions through surface CTAB dissolution. Similar to the interaction between copper and silver, copper and gold can undergo galvanic replacement. Gold ions in solution can replace copper atoms in nanoparticles, forming bimetallic structures [60]. It is assumed that Cr^{3+} and Cu^{2+} ions interacted directly with CTAB and adsorbed onto the nanorod surface. Previous studies have shown that CTAB-AuNR in hydrogen bromide-buffered solution and coated with $Na_2S_2O_3$ in NH_3/NH_4Cl buffer selectively detect Cu^{2+} [55,56]. Additionally, L-cysteine-coated gold nanorods have been reported to detect Cu^{2+} [52]. These findings suggest that the interaction between CTAB and Cu^{2+} is independent of the ligand or buffer, as Cu^{2+} was detected across different conditions. In this study, NaOH was employed to weaken CTAB on nanorods, potentially allowing for the detection of multiple metals, which was not observed in previous studies (Table 2). Using longer nanorods (AuNR2), different metals such as Hg^{2+}, Cu^{2+}, Ni^{2+}, and Fe^{3+} were detected. The underlying mechanism is similar to that of AuNR1, where the addition of NaOH leads to weak binding of CTAB on the nanorod surface. This allowed Hg^{2+} to interact with Au due to its high affinity, similar to its interaction with Ag. Previous reports have shown that L-cysteine-, TPDT-silicate-, and L-arginine-coated AuNR can detect Hg^{2+} despite different ligand conjugations [50,54,58]. These findings suggest that metal–ion interactions with CTAB-capped nanoparticles occur through ionic interactions with the surface capping. Once the surface capping is weakened, multiple metals, rather than a single metal, can be detected. This approach enhances the sensing ability regarding various metal ions without the need for additional linkers, ligands, or buffers.

The current study demonstrates superior performance compared to traditional methods and establishes a novel multimetal detection system using CTAB-capped nanoparticles, which has not been reported before.

LOD and LOQ quantification

This study confirmed the detection of heavy metals using CTAB-capped metal nanoparticles by changing the parameters such as size, shape, as-prepared/centrifuged, and concentration of the nanoparticles, as well as the volume of added NaOH solution. However, the detected metals were at 1 ppm concentration. Therefore, it is impossible to calculate the minimum detection limit because the metal detection happened at a minimum threshold of 1 ppm. Despite that, this study allows other researchers to design nanosensors without surface modification or the use of linker molecules for multimetal detection. However, pristine isotropic gold and silver nanoparticles (without capping) detect multiple metals at 1 ppm concentration, including chromium (Supporting Information File 1, Figure S10). Furthermore, the LOD of Cr^{3+} was calculated using bare AuNS using a linear plot in the range of 100–400 ppb (Supporting Information File 1, Figure S19a,b). The LOD and LOQ of Cr^{3+} using pristine gold nanoparticles were 469.34 and 1422.25 ppb, respectively. Even though CTAB-capped nanoparticles do not go beyond 1 ppm, they are selective for metal detection, which is not the case for pristine gold nanospheres. Thus, CTAB-capped metal nanoparticles can be tailored for heavy metal detection without using linkers or buffers by modifying parameters such as size, shape, concentration, as-prepared/centrifuged, and the volume of NaOH solution.

Catalytic efficiency of CTAB-capped nanoparticles

The catalytic efficiency of CTAB-capped metal nanoparticles was investigated using 4-nitrophenol, a commonly employed substrate for assessing the catalytic efficiency of nanoparticles, as a substrate. Previous studies on CTAB-capped nanoparticles have suggested their role as a catalytic agent for the conversion of 4-NP to 4-AP in the presence of $NaBH_4$ [27]. All catalysis experiments were conducted in situ by performing the reduction reaction in a standard 1 cm path length quartz cuvette and measuring the spectral changes as the reaction progressed. The experimental setup involved an aqueous solution of 0.1 mM 4-NP and 0.1 M $NaBH_4$, followed by the addition of CTAB-capped nanoparticles. Immediately after the addition of $NaBH_4$, a color change from light yellow to yellow-green was observed; simultaneously, the spectral absorption changed from 317 to 400 nm due to the formation of 4-nitrophenolate ions in the reaction medium [61]. The reduction of 4-nitrophenolate ions to 4-aminophenol was initiated only upon the addition of nanoparticles as a catalyst, and reaction kinetics were monitored using a UV–visible spectrophotometer. The visible change from yellow to a colorless solution corresponded to a decrease in the peak intensity at 400 nm and the formation of a minor peak around 300 nm due to the formation of 4-aminophenol. The catalytic conversion of 4-nitrophenol by as-prepared CTAB-$AgNS_{0.5}$ and CTAB-$AgNS_{1.0}$ was completed in 115 and 65 min with catalytic efficiencies of 87.82% and 89.14%, respectively, (Figure 8a,b).

Using centrifuged CTAB-$AgNS_{0.5}$ and CTAB-$AgNS_{1.0}$, the degradation times were 40 and 30 min with catalytic efficiencies of 93.13% and 90.78%, respectively (Figure 8c,d). Shaikh et al. showed the degradation of 4-NP using ginger extract-stabilized CTAB-capped silver nanospheres [62]. However, the current study observed the degradation of 4-NP based on nanoparticle concentration and preparation conditions without using any linker. Centrifuged particles are more efficient compared to as-prepared nanoparticles. In comparison, CTAB and pristine AgNPs (1 OD) degraded 4-NP within 60 and 40 min, respectively (Supporting Information File 1, Figure S20). CTAB-AgNPs degrade 4-NP faster because of a synergistic effect. Furthermore, the impact of the metal with the same capping was also evaluated. Using as-prepared CTAB-$AuNS_{0.5}$ and CTAB-$AuNS_{1.0}$, the degradation of 4-NP was achieved in 3 and 1 min with catalytic efficiencies of 93.91% and 94.37%, respectively (Figure 8e,f). The present findings corroborate those reported by Satapathy and colleagues. The authors concluded that the degradation of 4-NP highly depends on the nanoparticle concentration, which is also observed in our study [61]. Compared to the as-prepared nanoparticles, centrifuged CTAB-$AuNS_{0.5}$ and $AuNS_{1.0}$ took 5 and 3 min with catalytic efficiencies of 87.97% and 93.20%, respectively, for the degradation of 4-NP (Figure 8g,h). The time required for the degradation of 4-NP using centrifuged gold nanospheres is higher than that using as-prepared AuNS. This might be due to the lower amount of CTAB in centrifuged AuNS. The degradation times of 4-NP using CTAB and bare/uncapped AuNS were 60 and 5 min, respectively (Supporting Information File 1, Figure S20). This confirmed that gold nanoparticles have catalytic activity against 4-NP, enhanced upon capping with CTAB. However, it was reported that the shape of nanoparticles also influences their catalytic property in the degradation of 4-NP [63]. Figure 9a,b shows the decrease in optical absorption of 4-NP (λ_{max} 400 nm) using as-prepared CTAB-$AuNR1_{0.5}$ and $AuNR1_{1.0}$ as reaction catalysts. The Figure inset represents a color change from yellow to colorless obtained within 8 and 5 min with catalytic efficiencies of 93.83% and 94.37%, respectively, after the addition of as-prepared CTAB-$AuNR1_{0.5}$ and $AuNR1_{1.0}$.

A similar trend was observed in the case of centrifuged AuNR1, where a high nanoparticle concentration ($AuNR1_{1.0}$) required less time than a lower concentration ($AuNR1_{0.5}$) (Figure 9c,d).

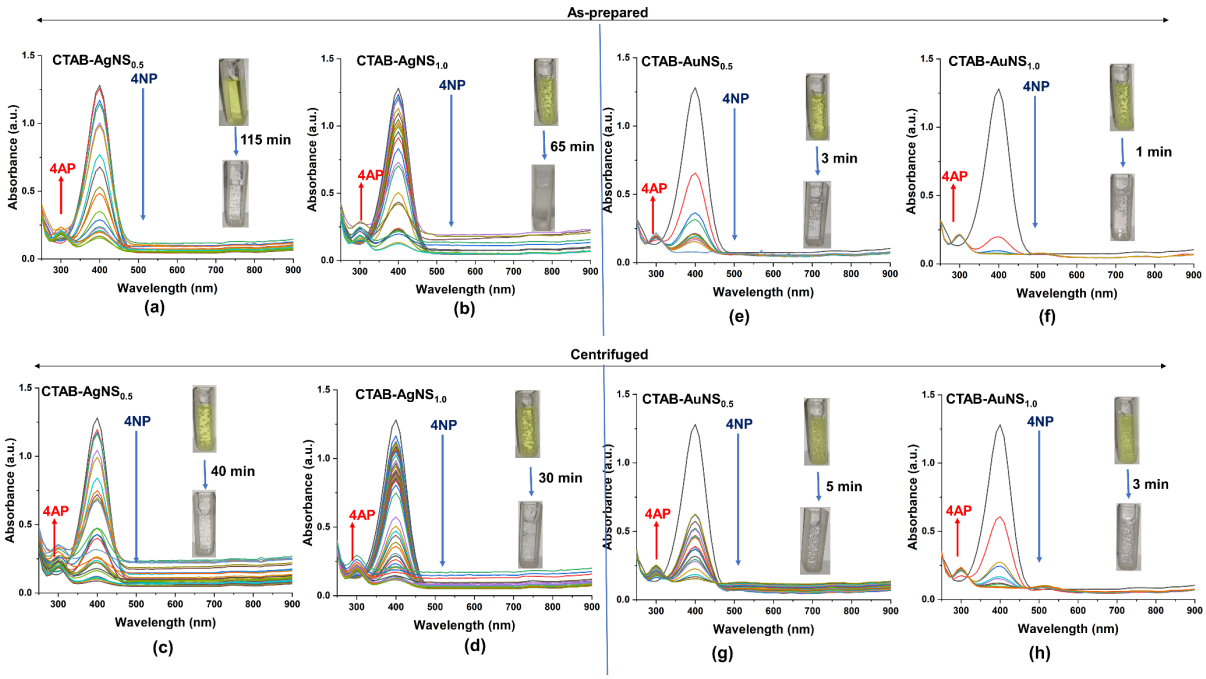


Figure 8: Degradation of 4 nitrophenol (4-NP) to 4 aminophenol (4-AP) using CTAB-AgNS and AuNS. (a) As-prepared $AgNS_{0.5}$, (b) as-prepared $AgNS_{1.0}$, (c) centrifuged $AgNS_{0.5}$, (d) centrifuged $AgNS_{1.0}$, (e) as-prepared $AuNS_{0.5}$, (f) as-prepared $AuNS_{1.0}$, (g) centrifuged $AuNS_{0.5}$, and (h) centrifuged $AuNS_{1.0}$. The inset color shows a change in the degradation of 4-NP to 4-AP. The subscripts 0.5 and 1.0 represent the nanoparticle concentration in terms of optical density.

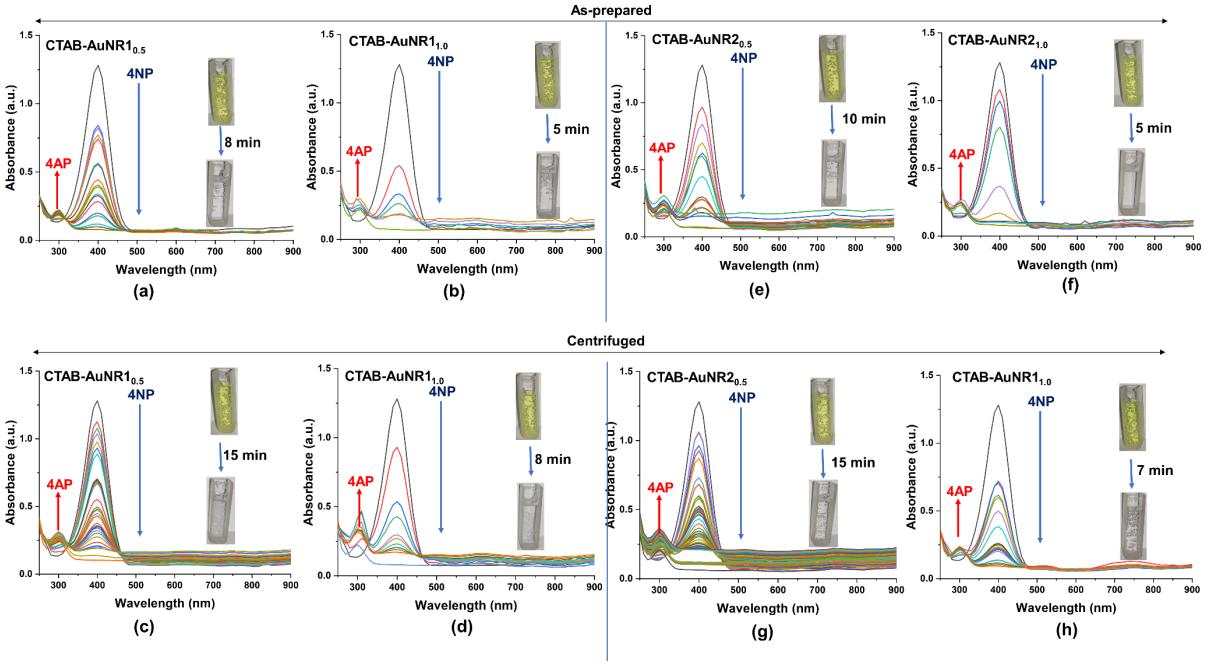


Figure 9: Degradation of 4 nitrophenol (4-NP) to 4 aminophenol (4-AP) using CTAB-AuNR1 and AuNR2. (a) As-prepared $AuNR1_{0.5}$, (b) as-prepared $AuNR1_{1.0}$, (c) centrifuged $AuNR1_{0.5}$, (d) centrifuged $AuNR1_{1.0}$, (e) as-prepared $AuNR2_{0.5}$, (f) as-prepared $AuNR2_{1.0}$, (g) centrifuged $AuNR2_{0.5}$, and (h) centrifuged $AuNR2_{1.0}$. The inset shows the change in degradation of 4-NP to 4-AP. The subscripts 0.5 and 1.0 represent the nanoparticles concentration in terms of optical density.

The degradation times of 4-NP using centrifuged $AuNR1_{0.5}$ and $AuNR1_{1.0}$ were 8 and 5 min with catalytic efficiencies of 91.95% and 93.83%, respectively. This confirmed that as-prepared AuNR1 showed higher efficiency for the degradation of 4-NP compared to centrifuged AuNR1. This might be due to excess CTAB in as-prepared AuNR1, which is also the case with CTAB-AuNS. CTAB, without nanoparticles, can reduce 4-NP to 4-AP (Supporting Information File 1, Figure S20a). However, the degradation time was much higher than that of the CTAB-capped nanoparticles, as observed in the case of CTAB-AuNR1. We also analyzed the role of nanoparticle size in the degradation of 4-NP. Therefore, the potential of longer CTAB-AuNR was also evaluated. As-prepared $CTAB\text{-}AuNR2_{0.5}$ and $AuNR2_{1.0}$ showed degradation times of 10 and 5 min with catalytic efficiencies of 94.76% and 93.83%, respectively (Figure 9e,f). Centrifuged $CTAB\text{-}AuNR2_{0.5}$ and $AuNR2_{1.0}$ degraded 4-NP within 15 and 7 min with catalytic efficiencies of 95.01% and 92.74%, respectively, similar to the case for CTAB-AuNR1 (Figure 9g,h). A slight change in degradation time was observed due to the size difference of the gold nanorods. A trend reversal in CTAB-AgNS was observed, where centrifuged AgNS showed minimal degradation time compared to as-prepared. The 4-NP degradation time of centrifuged CTAB-AgNS was comparable to that of bare AgNS (Supporting Information File 1, Figure S20). This study suggests that the degradation of 4-NP using nanoparticles highly depends on nanoparticle concentration, size, shape, and preparation. Table 3 summarizes various studies performed regarding the degradation of 4-nitrophenol using nanoparticle-based systems.

Possible mechanism of 4-NP degradation

The catalytic degradation of 4-NP was achieved using CTAB-capped nanoparticles as nanocatalysts, where CTAB-AuNS is highly efficient compared to CTAB-AgNS, CTAB-AuNR1, and CTAB-AuNR2. The underlying mechanism behind 4-NP degradation using CTAB-capped gold and silver nanoparticles involves a complex series of surface-mediated reactions. Initially, 4-NP in its ionic form (4-nitrophenolate) penetrates the CTAB bilayer and adsorbs onto the metal nanoparticle surface, facilitated by electrostatic interactions [69,70]. Concurrently, borohydride ions (BH^{4-}) from $NaBH_4$ also adsorb on the nanoparticle surface. The metal nanoparticle acts as an electron relay, accepting electrons from BH^{4-} and transferring them to the adsorbed 4-nitrophenolate [69]. This electron transfer initiates a stepwise reduction of the nitro group, proceeding through nitroso and hydroxylamine intermediates before finally yielding 4-aminophenol (4-AP).

The reduction follows the pathway: 4-NO_2-phenolate → 4-NO-phenolate → 4-NHOH-phenolate → 4-NH_2-phenolate. Once formed, 4-AP desorbs from the nanoparticle surface, allowing the catalytic cycle to continue [69]. The efficiency of this process is influenced by nanoparticle properties such as surface area, size, and shape, with smaller particles generally exhibiting higher catalytic activity due to their increased surface-to-volume ratio.

Conclusion

This study developed a flexible nanosensor without linkers, using cetyltrimethylammonium bromide as capping agent on gold and silver nanoparticles. The nanosensor was designed to rapidly detect heavy metal ions and degrade organic pollutants like 4-nitrophenol. CTAB-AgNS, CTAB-AuNS, CTAB-AuNR1, and CTAB-AuNR2 nanoparticles were characterized regarding size, shape, surface charge, functional group interactions, and crystalline structure. Stability tests with NaCl and NaOH showed that CTAB-AgNS exhibited decreased plas-

Table 3: Studies related to nanoparticles for the degradation of 4-nitrophenol.

System	Shape	Degradation time (min)	Reference
CTAB-AuNP	sphere	1	[61]
CTAB-AgNP and bare AgNP (in extract)	sphere	3	[62]
Silica coated CTAB-AuNR	rod	5–6	[64]
Cochliobolus geniculatus coated ZnO nanoparticles	quasi-spherical	30	[65]
B. amyloliquefaciens capped silver nanoparticles	sphere	15	[66]
Jatropha leaf extract capped iron nanoparticles	irregular shaped	60	[67]
polyvinyl alcohol/silver nanoparticle film	sphere	25	[68]
CTAB AgNS	sphere	30	this work[a]
CTAB-AuNS	sphere	1	
CTAB-AuNR1	rod	5	
CTAB-AuNR2	rod	5	

[a]The obtained degradation time depends on nanoparticle concentration, size, shape and preparation of the nanoparticles.

monic intensity and aggregation, while CTAB-AuNS and CTAB-AuNR1 demonstrated higher stability than CTAB-AuNR2. CTAB-AuNS efficiently degraded 4-nitrophenol (94.37% within 1 min), while CTAB-AuNR1 and AuNR2 degraded it within 5 min with an efficiency of 94.37% and 93.83%, respectively. The efficiency of the sensing probes depended on factors like nanoparticle concentration, preparation method (as-prepared/centrifuged), and NaOH addition. As-prepared CTAB-AgNS detected Cu^{2+} and Hg^{2+} ions at specific concentrations, whereas CTAB-AuNR1 and AuNR2 detected multiple metals under particular conditions. CTAB-AuNS showed no metal ion detection capability. These results highlight the importance of size, shape, concentration, and preparation method of the nanoparticles in sensing and catalytic applications. The sensor achieved metal ion detection at 1 ppm without linkers or buffer solvents and detected multiple metal ions based on reaction parameters. Future research will enhance sensitivity towards metal detection using linker-free CTAB-capped metal nanoparticles combined with advanced strategies. This study demonstrates the potential of linker-free CTAB-capped metal nanoparticles for simultaneous pollutant detection and degradation, offering promising environmental remediation and sensing applications.

Supporting Information

The file contains twenty figures. Figure S1 is an HPLC chromatogram showing peak retention time for CTAB and CTAB-capped nanoparticles. Figures S2–S9 are spectrophotometric and colorimetric visualizations of metal detection using isotropic CTAB-capped nanoparticles. Figure S10 depicts the spectrophotometric and colorimetric detection of metal ions using bare gold and silver nanoparticles. Figures S11–S18 show the detection of metal ions using anisotropic nanoparticles of gold (i.e., AuNR1 and AuNR2). Figures S19 and S20 present the quantification of Cr^{3+} using bare AuNS and the catalytic degradation of 4-NP with CTAB, bare AuNS and bare AgNS, respectively.

Supporting Information File 1

Additional figures.
[https://www.beilstein-journals.org/bjnano/content/supplementary/2190-4286-15-106-S1.pdf]

Acknowledgements

The authors acknowledge Mrs. Nidhi Arjaria and Mr. Jai Shankar for TEM imaging, Mr. Joel Saji for XRD and Mr. Alok Kumar for HPLC measurements. The authors are grateful to CSIR-IITR, Lucknow, for providing the platform and facilities for this research work. The CSIR-IITR publication committee approved this paper, and the communication number is IITR/SEC/MS/2024/22.

Funding

This research work was supported by the CSIR-Indian Institute of Toxicology Research (Major Laboratory Project-MLP-001) approved by the competent authority of CSIR-IITR, Lucknow, India. Akash Kumar is thankful to CSIR for providing a fellowship.

Conflict of Interest

The authors declare that there is no conflict of interest.

Author Contributions

Akash Kumar: data curation; investigation; methodology; validation; visualization; writing – original draft. Raja Gopal Rayavarapu: conceptualization; data curation; formal analysis; funding acquisition; investigation; project administration; resources; software; supervision; validation; visualization; writing – review & editing.

ORCID® iDs

Akash Kumar - https://orcid.org/0000-0002-0493-1991
Raja Gopal Rayavarapu - https://orcid.org/0000-0002-8769-4679

Data Availability Statement

The data that supports the findings of this study is available from the corresponding author upon reasonable request.

References

1. Das, A.; Dey, A. *J. Environ. Chem. Eng.* **2020,** *8,* 103830. doi:10.1016/j.jece.2020.103830
2. Ariga, K. *Bull. Chem. Soc. Jpn.* **2024,** *97,* uoad001. doi:10.1093/bulcsj/uoad001
3. Javed, R.; Zia, M.; Naz, S.; Aisida, S. O.; Ain, N. u.; Ao, Q. *J. Nanobiotechnol.* **2020,** *18,* 172. doi:10.1186/s12951-020-00704-4
4. Li, X.; Yoneda, M.; Shimada, Y.; Matsui, Y. *Sci. Total Environ.* **2017,** *574,* 176–182. doi:10.1016/j.scitotenv.2016.09.065
5. Al-Thabaiti, S. A.; Obaid, A. Y.; Hussain, S.; Khan, Z. *Arabian J. Chem.* **2015,** *8,* 538–544. doi:10.1016/j.arabjc.2014.11.030
6. Carnovale, C.; Bryant, G.; Shukla, R.; Bansal, V. *ACS Omega* **2019,** *4,* 242–256. doi:10.1021/acsomega.8b03227
7. El-Nahass, M. N.; Bakr, E. A.; Fayed, T. A.; Hamada, W. M.; Salem, M. M.; Radwan, A. M. *J. Iran. Chem. Soc.* **2024,** *21,* 699–718. doi:10.1007/s13738-023-02952-1
8. Anna, K. K.; Bogireddy, N. K. R.; Ramírez-Bon, R. *Nanotechnology* **2021,** *32,* 105707. doi:10.1088/1361-6528/abccee
9. Moudgil, L.; Jaiswal, J.; Mittal, A.; Saini, G. S. S.; Singh, G.; Kaura, A. *J. Mol. Liq.* **2019,** *276,* 910–918. doi:10.1016/j.molliq.2018.12.106
10. Tchieno, F. M. M.; Tonle, I. K. *Rev. Anal. Chem.* **2018,** *37,* 20170019. doi:10.1515/revac-2017-0019

11. Abd Elnabi, M. K.; Elkaliny, N. E.; Elyazied, M. M.; Azab, S. H.; Elkhalifa, S. A.; Elmasry, S.; Mouhamed, M. S.; Shalamesh, E. M.; Alhorieny, N. A.; Abd Elaty, A. E.; Elgendy, I. M.; Etman, A. E.; Saad, K. E.; Tsigkou, K.; Ali, S. S.; Kornaros, M.; Mahmoud, Y. A.-G. *Toxics* **2023,** *11,* 580. doi:10.3390/toxics11070580
12. Teschke, R. *Int. J. Mol. Sci.* **2022,** *23,* 12213. doi:10.3390/ijms232012213
13. Wyatt, L. H.; Luz, A. L.; Cao, X.; Maurer, L. L.; Blawas, A. M.; Aballay, A.; Pan, W. K. Y.; Meyer, J. N. *DNA Repair* **2017,** *52,* 31–48. doi:10.1016/j.dnarep.2017.02.005
14. Yuen, H.-W.; Becker, W. Iron toxicity. *StatPearls [Internet];* StatPearls Publishing, 2023. PMID:29083637.
15. Bradberry, S. M. *Medicine* **2016,** *44,* 182–184. doi:10.1016/j.mpmed.2015.12.008
16. Naushad, M.; Ahamad, T.; Rizwan Khan, M. *Chemosphere* **2022,** *303,* 135173. doi:10.1016/j.chemosphere.2022.135173
17. Szafran, B.; Klein, R.; Buser, M.; Balachandran, R.; Haire, K.; Derrick, H.; Roney, N.; Hall, S.; Gao, A.; Zaccaria, K. CHAPTER 1: RELEVANCE TO PUBLIC HEALTH. *Toxicological Profile for Nitrophenols;* Agency for Toxic Substances and Disease Registry (US): Atlanta (GA), 2023. https://www.ncbi.nlm.nih.gov/books/NBK601147/
18. Xu, G.; Song, P.; Xia, L. *Nanophotonics* **2021,** *10,* 4419–4445. doi:10.1515/nanoph-2021-0363
19. Singh, A.; Shah, S. S.; Sharma, C.; Gupta, V.; Sundramoorthy, A. K.; Kumar, P.; Arya, S. *J. Environ. Chem. Eng.* **2024,** *12,* 113032. doi:10.1016/j.jece.2024.113032
20. Javaid, R.; Kawasaki, S.-i.; Suzuki, A.; Suzuki, T. M. *Beilstein J. Org. Chem.* **2013,** *9,* 1156–1163. doi:10.3762/bjoc.9.129
21. Chen, Z.; Zhang, Z.; Qi, J.; You, J.; Ma, J.; Chen, L. *J. Hazard. Mater.* **2023,** *441,* 129889. doi:10.1016/j.jhazmat.2022.129889
22. Alberti, G.; Zanoni, C.; Magnaghi, L. R.; Biesuz, R. *Chemosensors* **2021,** *9,* 305. doi:10.3390/chemosensors9110305
23. Kailasa, S. K.; Chandel, M.; Mehta, V. N.; Park, T. J. *Spectrochim. Acta, Part A* **2018,** *195,* 120–127. doi:10.1016/j.saa.2018.01.038
24. Nguyen, N. L. T.; Kim, E. J.; Chang, S.-K.; Park, T. J. *BioChip J.* **2016,** *10,* 65–73. doi:10.1007/s13206-016-0109-8
25. Sung, H. K.; Oh, S. Y.; Park, C.; Kim, Y. *Langmuir* **2013,** *29,* 8978–8982. doi:10.1021/la401408f
26. Yagyu, J.; Islam, M. S.; Yasutake, H.; Hirayama, H.; Zenno, H.; Sugimoto, A.; Takagi, S.; Sekine, Y.; Ohira, S.-I.; Hayami, S. *Bull. Chem. Soc. Jpn.* **2022,** *95,* 862–870. doi:10.1246/bcsj.20220058
27. Fenger, R.; Fertitta, E.; Kirmse, H.; Thünemann, A. F.; Rademann, K. *Phys. Chem. Chem. Phys.* **2012,** *14,* 9343–9349. doi:10.1039/c2cp40792b
28. Sui, Z. M.; Chen, X.; Wang, L. Y.; Xu, L. M.; Zhuang, W. C.; Chai, Y. C.; Yang, C. J. *Phys. E (Amsterdam, Neth.)* **2006,** *33,* 308–314. doi:10.1016/j.physe.2006.03.151
29. Silva, L. I. M.; Pérez-Gramatges, A.; Larrude, D. G.; Almeida, J. M. S.; Aucélio, R. Q.; da Silva, A. R. *Colloids Surf., A* **2021,** *614,* 126174. doi:10.1016/j.colsurfa.2021.126174
30. Rayavarapu, R. G.; Petersen, W.; Hartsuiker, L.; Chin, P.; Janssen, H.; van Leeuwen, F. W. B.; Otto, C.; Manohar, S.; van Leeuwen, T. G. *Nanotechnology* **2010,** *21,* 145101. doi:10.1088/0957-4484/21/14/145101
31. Das, N.; Kumar, A.; Kumar Roy, S.; Kumar Satija, N.; Raja Gopal, R. *IET Nanobiotechnol.* **2020,** *14,* 851–857. doi:10.1049/iet-nbt.2020.0097
32. He, J.; Unser, S.; Bruzas, I.; Cary, R.; Shi, Z.; Mehra, R.; Aron, K.; Sagle, L. *Colloids Surf., B* **2018,** *163,* 140–145. doi:10.1016/j.colsurfb.2017.12.019
33. Kuperkar, K.; Abezgauz, L.; Prasad, K.; Bahadur, P. *J. Surfactants Deterg.* **2010,** *13,* 293–303. doi:10.1007/s11743-009-1173-z
34. Kianfar, E. Catalytic Properties of Nanomaterials and Factors Affecting it. *Importance & Applications of Nanotechnology;* MedDocs Publishers, 2020; Vol. 5, pp 22–25. https://meddocsonline.org/ebooks/ebook-nanotechnology/catalytic-properties-of-nanomaterials-and-factors-affecting-it.pdf
35. Ziai, Y.; Rinoldi, C.; Nakielski, P.; De Sio, L.; Pierini, F. *Curr. Opin. Biomed. Eng.* **2022,** *24,* 100413. doi:10.1016/j.cobme.2022.100413
36. Sahu, A. K.; Das, A.; Ghosh, A.; Raj, S. *Nano Express* **2021,** *2,* 010009. doi:10.1088/2632-959x/abd966
37. da Silva, J. A.; Netz, P. A.; Meneghetti, M. R. *Langmuir* **2020,** *36,* 257–263. doi:10.1021/acs.langmuir.9b03235
38. Kalipillai, P.; Raghuram, E.; Bandyopadhyay, S.; Mani, E. *Phys. Chem. Chem. Phys.* **2022,** *24,* 28353–28361. doi:10.1039/d2cp02202h
39. Fischer, K.; Schmidt, M. *Biomaterials* **2016,** *98,* 79–91. doi:10.1016/j.biomaterials.2016.05.003
40. Danaei, M.; Dehghankhold, M.; Ataei, S.; Hasanzadeh Davarani, F.; Javanmard, R.; Dokhani, A.; Khorasani, S.; Mozafari, M. R. *Pharmaceutics* **2018,** *10,* 57. doi:10.3390/pharmaceutics10020057
41. Joseph, E.; Singhvi, G. Multifunctional nanocrystals for cancer therapy: a potential nanocarrier. *Nanomaterials for Drug Delivery and Therapy;* Elsevier: Amsterdam, Netherlands, 2019; pp 91–116. doi:10.1016/b978-0-12-816505-8.00007-2
42. Mandal, S.; Arumugam, S. K.; Adyanthaya, S. D.; Pasricha, R.; Sastry, M. *J. Mater. Chem.* **2004,** *14,* 43–47. doi:10.1039/b308180j
43. Nikoobakht, B.; El-Sayed, M. A. *Langmuir* **2001,** *17,* 6368–6374. doi:10.1021/la010530o
44. Niu, Y.; Omurzak, E.; Cai, R.; Syrgakbek kyzy, D.; Zhasnakunov, Z.; Satyvaldiev, A.; Palmer, R. E. *Surfaces (Basel, Switz.)* **2022,** *5,* 202–208. doi:10.3390/surfaces5010013
45. Yadav, V. D.; Jain, R.; Dandekar, P. *Mater. Res. Express* **2017,** *4,* 085015. doi:10.1088/2053-1591/aa8088
46. Cunningham, B.; Engstrom, A. M.; Harper, B. J.; Harper, S. L.; Mackiewicz, M. R. *Nanomaterials* **2021,** *11,* 1516. doi:10.3390/nano11061516
47. Vashishtha, M.; Mishra, M.; Shah, D. O. *J. Mol. Liq.* **2015,** *210,* 151–159. doi:10.1016/j.molliq.2015.02.017
48. Roque, L.; Fernández, M.; Benito, J. M.; Escudero, I. *Colloids Surf., A* **2020,** *601,* 124999. doi:10.1016/j.colsurfa.2020.124999
49. Samuel, V. R.; Rao, K. J. *Appl. Nanosci.* **2024,** *14,* 33–42. doi:10.1007/s13204-023-02948-6
50. Placido, T.; Comparelli, R.; Striccoli, M.; Agostiano, A.; Merkoci, A.; Curri, M. L. *IEEE Sens. J.* **2013,** *13,* 2834–2841. doi:10.1109/jsen.2013.2257738
51. Shahbazi, N.; Zare-Dorabei, R. *ACS Omega* **2019,** *4,* 17519–17526. doi:10.1021/acsomega.9b02389
52. Xu, S.; Wang, Y.; Sun, Y.; Shan, G.; Chen, Y.; Liu, Y. *Sens. Actuators, B* **2017,** *248,* 761–768. doi:10.1016/j.snb.2017.04.016
53. Placido, T.; Aragay, G.; Pons, J.; Comparelli, R.; Curri, M. L.; Merkoci, A. *ACS Appl. Mater. Interfaces* **2013,** *5,* 1084–1092. doi:10.1021/am302870b
54. Jayabal, S.; Sathiyamurthi, R.; Ramaraj, R. *J. Mater. Chem. A* **2014,** *2,* 8918–8925. doi:10.1039/c4ta01363h

55. Chen, Z.; Liu, R.; Wang, S.; Qu, C.; Chen, L.; Wang, Z. *RSC Adv.* **2013,** *3,* 13318–13323. doi:10.1039/c3ra40559a
56. Zhang, Z.; Chen, Z.; Qu, C.; Chen, L. *Langmuir* **2014,** *30,* 3625–3630. doi:10.1021/la500106a
57. Ge, K.; Liu, J.; Fang, G.; Wang, P.; Zhang, D.; Wang, S. *Sensors* **2018,** *18,* 2372. doi:10.3390/s18072372
58. Guan, J.; Wang, Y.-C.; Gunasekaran, S. *J. Food Sci.* **2015,** *80,* N828–N833. doi:10.1111/1750-3841.12811
59. He, X.; He, R.; Lan, Q.; Duan, F.; Xiao, J.; Song, M.; Zhang, M.; Chen, Y.; Li, Y. *J. Nanomater.* **2016,** *2016,* 2127980. doi:10.1155/2016/2127980
60. Luo, K.; Li, Y.; Liu, T.; Zhuge, X.; Chung, E.; Timms, A. R.; Graham, S. P.; Ren, G. *ACS Omega* **2023,** *8,* 36171–36178. doi:10.1021/acsomega.3c03665
61. Satapathy, S.; Mohanta, J.; Si, S. *ChemistrySelect* **2016,** *1,* 4940–4948. doi:10.1002/slct.201600985
62. Shaikh, J. A. *J. Iran. Chem. Soc.* **2022,** *19,* 4149–4158. doi:10.1007/s13738-022-02593-w
63. De Oliveira, F. M.; Nascimento, L. R. B. d. A.; Calado, C. M. S.; Meneghetti, M. R.; Da Silva, M. G. A. *Catalysts* **2016,** *6,* 215. doi:10.3390/catal6120215
64. Mohanta, J.; Satapathy, S.; Si, S. *ChemPhysChem* **2016,** *17,* 364–368. doi:10.1002/cphc.201501127
65. Kadam, V. V.; Shanmugam, S. D.; Ettiyappan, J. P.; Balakrishnan, R. M. *Environ. Sci. Pollut. Res.* **2021,** *28,* 12119–12130. doi:10.1007/s11356-020-10833-w
66. Samuel, M. S.; Jose, S.; Selvarajan, E.; Mathimani, T.; Pugazhendhi, A. *J. Photochem. Photobiol., B* **2020,** *202,* 111642. doi:10.1016/j.jphotobiol.2019.111642
67. Rawat, S.; Singh, J.; Koduru, J. R. *Environ. Technol. Innovation* **2021,** *24,* 101857. doi:10.1016/j.eti.2021.101857
68. Mostafa, A. M.; Menazea, A. A. *J. Mol. Struct.* **2020,** *1212,* 128125. doi:10.1016/j.molstruc.2020.128125
69. Mejía, Y. R.; Reddy Bogireddy, N. K. *RSC Adv.* **2022,** *12,* 18661–18675. doi:10.1039/d2ra02663e
70. Das, T. K.; Das, N. C. *Int. Nano Lett.* **2022,** *12,* 223–242. doi:10.1007/s40089-021-00362-w

License and Terms

This is an open access article licensed under the terms of the Beilstein-Institut Open Access License Agreement (https://www.beilstein-journals.org/bjnano/terms), which is identical to the Creative Commons Attribution 4.0 International License (https://creativecommons.org/licenses/by/4.0). The reuse of material under this license requires that the author(s), source and license are credited. Third-party material in this article could be subject to other licenses (typically indicated in the credit line), and in this case, users are required to obtain permission from the license holder to reuse the material.

The definitive version of this article is the electronic one which can be found at:
https://doi.org/10.3762/bjnano.15.106

BEILSTEIN JOURNAL OF NANOTECHNOLOGY

Clays enhanced with niobium: potential in wastewater treatment and reuse as pigment with antibacterial activity

Silvia Jaerger[*1,2], Patricia Appelt[‡2], Mario Antônio Alves da Cunha[‡3], Fabián Ccahuana Ayma[‡2], Ricardo Schneider[‡1], Carla Bittencourt[‡4] and Fauze Jacó Anaissi[*,‡2]

Full Research Paper

Open Access

Address:
[1]Federal University of Technology - Paraná - UTFPR, Campus Toledo, Rua Cristo Rei, 19. 85902-490, Toledo, Brazil, [2]Chemistry Department, Universidade Estadual do Centro-Oeste, Guarapuava 85040-167, PR, Brazil, [3]Department of Chemistry, Universidade Tecnológica Federal do Paraná, Pato Branco 85503-390, Brazil and [4]Chimie des Interactions PlaBEa-Surface (ChIPS), Research Institute for Materials Science and Engineering, University of Mons, 7000 Mons, Belgium

Email:
Silvia Jaerger[*] - sjaerger@gmail.com; Fauze Jacó Anaissi[*] - anaissi@unicentro.br

* Corresponding author ‡ Equal contributors

Keywords:
adsorption; bentonite; hybrid pigment; niobium; photocatalysis; water remediation

Beilstein J. Nanotechnol. **2025,** *16,* 141–154.
https://doi.org/10.3762/bjnano.16.13

Received: 10 September 2024
Accepted: 07 January 2025
Published: 10 February 2025

This article is part of the thematic issue "Advanced functional nanomaterials for water remediation applications".

Associate Editor: K. Ariga

© 2025 Jaerger et al.; licensee Beilstein-Institut.
License and terms: see end of document.

Abstract

Bentonite clay sourced from the Guarapuava region, Brazil, was modified with niobium oxide (BEOx) and niobium phosphate (BEPh) to act as an adsorbent and photocatalyst in the remediation of wastewater containing methylene blue (MB) dye. Additionally, colored materials were evaluated for their potential as antibacterial hybrid pigments. The bentonite clay modified with niobium was prepared by a solution containing swelling clay mixed with niobium oxide (NbOx) and niobium phosphate (NbPh) in a water solution; after that, the suspension was calcinated. X-ray diffractometry, X-ray photoelectron spectroscopy, and laser-induced breakdown spectroscopy assessed the modifications induced by the incorporation of niobium compounds into the clay, confirming the presence of niobium in the bentonite clay. Following characterization, the BEOx and BEPh samples were used as adsorbents or photocatalysts for treating solutions containing the MB dye (400 $mg{\cdot}L^{-1}$) at 25 °C. The results showed adsorption and photocatalysis efficiency above 94% for both samples. The blue-colored BEOx and BEPh samples were then applied as a hybrid pigment. The power pigment and its dispersion in colorless paint were evaluated by the CIEL*a*b* color space, and the ΔE parameters show values above 12, indicating a very strong color parameter difference. Subsequently, the efficacy of BEOx and BEPh as a hybrid pigment was assessed using the minimum inhibitory concentration (MIC) assay against two bacteria strains: *Bacillus cereus* (ATCC 10876) and *Proteus mirabilis* (ATCC 35649). The analysis revealed remarkable antibacterial activity against *Proteus mirabilis*, suggesting a preferential selectivity for Gram-negative bacteria.

Introduction

The most found dye pollutants in wastewater on a global scale originate from textile, plastic, paper, food, cosmetics, mineral, and pharmaceutical industries, among others, resulting in significant environmental impacts [1]. Dyes, as chemical compounds that impart color to different materials, play a crucial role in industries requiring coloring, such as textile, food, cosmetics, rubber, printing, paper, and plastic. Globally, an estimated 7×10^5 tons of dyes are produced, with 10–15% typically disposed of as wastewater pollutants [2]. Among the most used dyes, methylene blue (MB) is an intense blue cationic dye important in medical sciences, chemistry, and biology, as well as widely used in the textile industry [2]. Prolonged exposure to MB can result in adverse health effects, including abdominal disorders, respiratory distress, skin sensitization, and blindness [3]. The dark blue color of MB in wastewater reduces light penetration into aquatic organisms, disturbing the balance of the ecosystem and harming various forms of life [3]. Effluents and water bodies containing MB require prioritized treatment due to its adverse effect on water quality. Therefore, it is crucial to explore remedial strategies for MB, especially considering the water scarcity challenges that many countries face [3].

To satisfy environmental regulations, a range of wastewater treatment technologies with inherent advantages and limitations are available, encompassing processes such as advanced oxidation, extraction, and biodegradation [4]. Unfortunately, these methods exhibit inefficiencies due to the generation of secondary pollution and high operational costs. Biological and anaerobic degradation of dyes may yield carcinogenic by-products [4,5], highlighting the significant challenge in purifying water contaminated with dyes necessitating the development of cost-effective technologies for their removal from industrial effluents.

Adsorption emerges as a widely used method for pollutant removal from wastewater due to its design simplicity, operational ease, and relatively straightforward regeneration of the adsorbent. Various adsorbents including chitosan, cellulose, organophilic clays, kaolinite and montmorillonite clays, and activated carbon have been used for removing toxic compounds from polluted water [6]. Among these adsorbents, bentonite and smectite clays exhibit advantageous properties as an adsorbent, characterized by their low cost, abundant availability, nontoxic nature, and large surface area [2,7]. Additionally, its negatively charged surface renders it favorable for the adsorption of cations [7]. Bentonite clay is abundantly found in Guarapuava, Paraná, Brazil. This natural clay has predominantly the bentonite phase (at least 50%), known as montmorillonite. Isomorphic substitution of cations between the interlayer space of montmorillonites by exchanging Na^+, Ca^{2+}, Mg^{2+}, and Cu^{2+} cations add other functionalities to the resulting material [7].

Heterogeneous photocatalysis is a cost-effective alternative to biological treatment methods for purifying polluted water [8]. Using semiconductors as heterogeneous catalysts proves to be more efficient than traditional methods, as the photocatalytic process gradually decomposes contaminating molecules without generating residues from the original organic matter, thus avoiding the disposal of sludge [8]. This approach allows the removal of various organic pollutants, including textile dyes, using solid semiconductors (e.g., $NbOPO_4$ and Nb_2O_5) and photons (with energy greater than the bandgap energy of the semiconductor) to generate $OH^{\bullet}$ radicals (strong oxidants), leading to the mineralization of organic pollutants, including textile dyes [8].

In this study, the strategy and objective are to modify bentonite clay with niobium phosphate and niobium oxide by the calcinated method, and then use it as an adsorbent or photocatalyst to treat MB dye solutions and reuse this material as a hybrid pigment. Considering the semiconductor properties of niobium and the high capacity of the clay to remove pollutants from wastewater, we proposed in this research to use the niobium-modified clay as an adsorbent and photocatalyst to treat MB dye solutions. To reuse this colored material, recovered from the adsorption and photocatalysis tests, we propose using these as-prepared, blue-colored samples as a hybrid pigment. Subsequently, the as-prepared, blue-colored samples were evaluated for their color properties by CIEL*a*b* color space as a pigment in the powder form and dispersed in colorless paint. The novel-developed pigments, specifically the smectite clay modified with niobium-containing adsorbed dye, were investigated as antibacterial pigments.

Experimental

Materials

The bentonite clay from the Guarapuava region in the Parana State, Brazil, was purchased from a local supplier. Niobium phosphate ($NbOPO_4$) and niobium pentoxide (Nb_2O_5) were provided as donations by Companhia Brasileira de Metalurgia e Mineração (CBMM). Methylene blue, with molecular mass of 319.8513 $g \cdot mol^{-1}$, was obtained from Nuclear (Brazil).

Clay modified with niobium

First, the clays were swollen; for this purpose, 2 g of bentonite clay was dispersed in 100 mL of water, and the resulting suspension was kept under stirring for 24 h. In this experiment step, the color of raw clay was brown (Figure 1a). Then, 3.14 g of $NbOPO_4$ and Nb_2O_5 was added. The clay/Nb suspension was



Figure 1: The appearance of the sample of bentonite: raw bentonite (a); bentonite modified with $NbOPO_4$ (b), and bentonite modified with Nb_2O_5 (c).

continuously stirred for 72 h at 65 °C. The color of the bentonite modified with niobium changes to light yellow (Figure 1b,c). Finally, after being cooled to room temperature, the suspensions were subjected to thermal treatment at 500 °C, with a heating rate of 5 °C/min. These samples were named BEPh and BEOx for modification with $NbOPO_4$ and Nb_2O_5, respectively.

Adsorption and photocatalysis tests

Before the adsorption and photocatalysis assessments, a stock solution of the MB dye was prepared at a concentration of 1 $g{\cdot}L^{-1}$. The calibration analytical curve was established using a UV–vis spectrophotometer at a wavelength of 664 nm.

Adsorption experiments were conducted in batches containing 250 mg of the BEPh and BEOx samples under agitation at 25 °C. A volume of 100 mL of MB solutions at a concentration of 400 $mg{\cdot}L^{-1}$ were used for 3 h. The adsorption experiment was carried out considering ambient light conditions in the laboratory. Following the adsorption process, the clay/Nb samples were centrifuged at 3500 rpm for 10 min, and the final concentration of the solutions was determined using a UV–vis spectrophotometer. These samples were named A-BEPh and A-BEOx to designate the modification with $NbOPO_4$ and Nb_2O_5, respectively.

Photocatalytic tests were performed using 100 mL of an MB solution at a concentration of 400 $mg{\cdot}L^{-1}$. This experiment used 250 mg of the BEPh and BEOx samples as catalysts. The experimental setup system included a thermostatic Pyrex glass reactor at 25 °C (open), a magnetic stirrer, and a UV lamp (253.7 nm, 15 W, 220 V) within a dark chamber. After 3 h of exposure, the solutions were centrifuged at 3500 rpm for 10 min, and their final concentrations were determined using a UV–vis spectrophotometer. These samples were labeled as A-BEPhP and A-BEOxP to designate the modifications with $NbOPO_4$ and Nb_2O_5, respectively.

The adsorption efficiency of MB by the clays was calculated using Equation 1:

$$\%\text{Remotion} = 100 \cdot \frac{(C_0 - C_f)}{C_0}, \quad (1)$$

where C_0 ($mg{\cdot}L^{-1}$) is the initial concentration of the solution, and C_f ($mg{\cdot}L^{-1}$) is the concentration of the solution after the adsorption experiment.

The efficiency of MB photodegradation (X%) was determined by Equation 2:

$$X(\%) = \frac{(M_0 - M_f)}{M_0} \cdot 100, \quad (2)$$

where M_0 and M_f are the concentrations of MB at the beginning and at the end of the photocatalytic test, respectively.

Dispersion of the pigments clay/Nb and clay/Nb/MB in colorless commercial paint

The samples A-BEPh, A-BEOx, A-BEPhP, and A-BEOxP were separated through centrifugation and dried in an oven at 70 °C. The clay powders, clay/Nb, and clay/Nb/MB powders were tested as pigments in colorless commercial paint. For this purpose, a 10% (w/w) ratio of the pigments in colorless commercial paint (a transparent paint) was used. A sodium hydroxide solution (NaOH, 1 $mol{\cdot}L^{-1}$) was dripped onto the clay powders until reaching a pH between 8 and 10. Subsequently, this suspension was blended with the transparent paint. Plaster molds were painted with both colorless and pigmented paint. After the paint dried, the color was characterized through colorimetric analysis (CIEL*a*b*) and UV–vis spectroscopy.

Antimicrobial activity test

The antimicrobial properties of the BEPh, BEOx, A-BEPh, A-BEOx, A-BEPhP, and A-BEOxP samples were investigated against the bacteria *Bacillus cereus* (ATCC 10876) (Gram-positive) and *Proteus mirabilis* (ATCC 35649) (Gram-negative). The samples of bentonite clay modified with niobium were

dispersed in water. The assay followed the protocols described by the Clinical and Laboratory Standards Institute (CLSI). The samples were evaluated using the minimum inhibitory concentration (MIC) method [9,10] at concentrations ranging from 1.25 to 0.09 mg/mL.

The bacterial stock cultures were activated by culturing in brain heart infusion (BHI) broth at 37 °C for 24 h. Then, the cellular concentrations were standardized according to the McFarland 0.5 scale (≈1.5×10^8 CFU/mL) using a spectrophotometer at a wavelength of 625 nm in saline water tubes. Subsequently, 100 µL of Mueller–Hinton broth was added to all wells in 96-well plates, followed by duplicate addition of the samples using serial microdilution, and finally, 10 µL of the inoculum. The plates were then incubated for 24 h at 37 °C. After incubation, 20 µL of the TTC dye (0.125% w/v - 2,3,5-triphenyltetrazolium chloride 0.125%) (NEON®) was added to all wells, and the plate was kept in an oven for an additional two hours. The antibacterial activity was determined by MIC, observing the presence/absence of viable bacteria due to the reaction of the TTC dye with the enzyme succinate dehydrogenase (present in the mitochondria), leading to the formation of a salt called Formazan with a pink-reddish color.

Characterization

X-ray diffraction (XRD) measurements of the powder were conducted using a Rigaku BEartLab SE 3 kW diffractometer equipped with Cu Kα radiation (λ = 1.5410 Å) operating at 40 kV and 30 mA. Data were collected in scanning mode in steps between 4° and 75° (2θ) with a step size of 0.05°/s. The basal distance was obtained using Bragg's Law.

Fourier-transform infrared spectroscopy (FTIR) spectra were collected on a Perkin Elmer Frontier FTIR spectrometer using KBr pellets containing 1% by weight of the samples. Analyses of all samples were performed in the range of 4000 to 400 cm^{-1} with a resolution of 4 cm^{-1}, accumulating 10 scans.

Absorbance measurements of the supernatant solutions were analyzed using a UV–vis spectrophotometer (UV-1800 SHIMADZU) with a 1 cm path length glass cuvette at λ_{max} (maximum absorbance) in nanometers.

Samples collected after the adsorption process had the electronic spectra analyzed using an Ocean Optics USB-2000 instrument for solid samples with a tungsten lamp in the range of 200–800 nm in diffuse reflectance mode.

Powder and paint-applied samples were analyzed by colorimetry, based on the CIEL*a*b* system, using a portable colorimeter (NR60CP – 3NH).

The oxidation state and elemental composition of the samples were evaluated using X-ray photoelectron spectroscopy (XPS) with a PHI Genesis instrument from Physical Electronics (Chanhassen, MN, USA), equipped with a monochromatic Al Kα X-ray source. The binding energy was calibrated based on the C 1s peak at 284.6 eV.

Laser-induced breakdown spectroscopy (LIBS) analyses were carried out by using the Applied Spectra J200 equipment. The clay samples were pelletized in circular discs of 1.2 cm and approximately 0.2–0.3 cm of height. The discs were prepared using 5 mg of each sample, and then they was pressed at 10 tons. The spectra were collected under air atmosphere between 186 and 1050 nm using a laser line at 50% as the source performing 10 shots per spot with 50 µm of diameter and gate delay of 0.5 µs.

A static laser scattering (SLS) Horiba LA-960 equipment assessed the powder particle size distribution measurements using a 15 mL cuvette accessory and water as the dispersion medium. The refractive index was set to 1.640 for red and blue lines.

Results and Discussion

The XRD profile for bentonite clay, niobium phosphate, niobium oxide and its modifications with niobium phosphate and niobium oxide (BEPh and BEOx, respectively), as well as the samples obtained after adsorption/photocatalysis of MB (A-BEPh, A-BEOx, A-BEPhP, A-BEOxP), are shown in Figure 2. The XRD analysis for bentonite before modification with niobium indicates dioctahedral montmorillonite (M-COD 9002779 $M_x(Al_{4-x}Mg_x)Si_8O_{20}(OH)_4$) with an amount of kaolinite (K-COD 1011045 $Al_2H_4O_9Si_2$) and quartz (Q-COD 9012600 SiO_2) at 13.8%, 41.6%, and 44.6%, respectively [8].

The characteristic reflections of montmorillonite (M) for the basal spacing correspond to approximately 15 Å (d001 = 14.88 Å), related to the interlayer distance of 2:1 clays, resulting in a spacing between 14.0–15.0 Å corresponding to the peak at 6.17 2θ (º) [11]. The quartz phase (Q) was identified by the presence of reflections at 2θ = 50.02° and 68.32°. The characteristic peaks that allowed the identification of the kaolinite phase (K) were at 2θ = 12.48°and 20.14° [7].

Figure 2a,b presents diffraction patterns with amorphous characteristics of the niobium compounds $NbOPO_4$ and Nb_2O_5. Two broad peaks were identified, one at approximately 25.54° (2θ) and the other at 49.73° (2θ) [12,13]. The amorphous pattern characteristic of niobium compounds was maintained upon modification of the bentonite clay with these compounds.

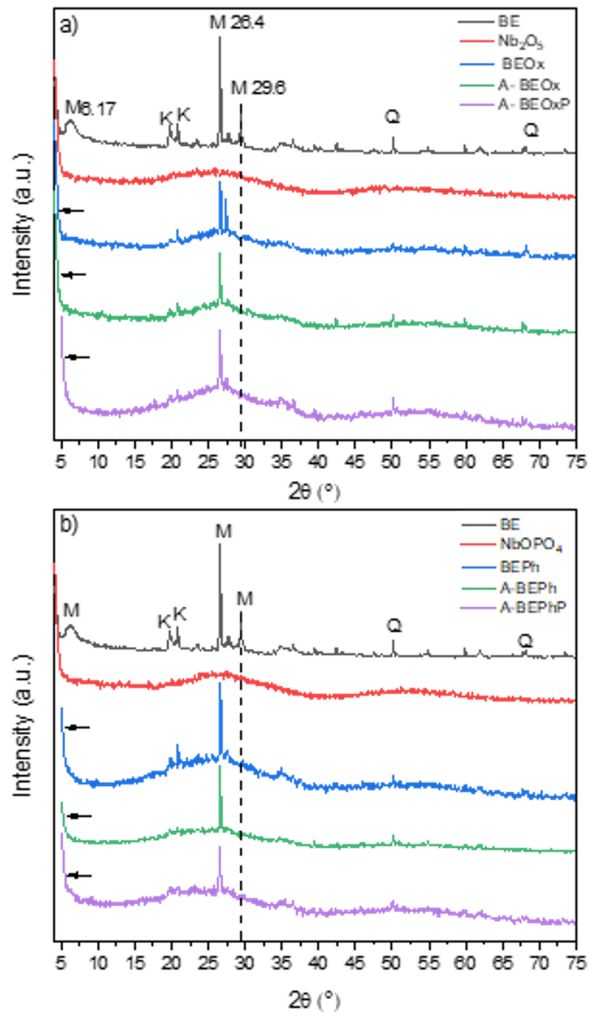


Figure 2: X-ray diffraction patterns of the bentonite samples and those modified with niobium oxide (a) and niobium phosphate (b).

The X-ray pattern of the samples of bentonite clay modified with the niobium compounds (BeOx and BEPh) and the same obtained after adsorption/photocatalysis of MB (A-BEPh, A-BEOx, A-BEPhP, and A-BEOxP) show the characteristic diffraction peak at approximately 26.4° (2θ) indicating that the niobium modification did not destroy the structure of the montmorillonite layer [14]. However, the relative intensity of the diffraction peak at 29.6° (2θ) decreased with the addition of the niobium compounds. This decrease can be attributed to the intercalation of the niobium in the interlayer of the clay, which increases the layer distance and the ion coordination of the interlayer to produce the polyhydroxyniobium. Another fact that can explain this result is the slight shifts of the montmorillonite characteristic diffraction peak (6.17° 2θ) to lower 2θ angles as observed in Figure 2a,b, suggesting increased interlayer space of the clay. The studies of Qiu et al. (2019) [14] and Gallo et al. (2006) [15] observed the same results, and indicated that the bentonite clay modified with niobium initiated the inorganic pillarization process from the polyhydroxyniobium process [14,15]. The supposed structure of bentonite clay modified with niobium phosphate and niobium oxide proposed in this study can be observed in Figure 3.

The FTIR spectra of the bentonite before and after modification with niobium are shown in Figure 4. It can be observed that for the BE samples and all those modified with $NbOPO_4$ (Figure 4a), the spectra show a narrow band in the region of 3638 cm^{-1}, associated with the (Al–OH–Al) Al_2OH vibrational stretching, indicative of bentonite with a high aluminum content in octahedra [7,16]. The spectra for the $NbOPO_4$ samples and for the bentonite modified with niobium phosphate (BEPh) before and after adsorption/photocatalysis (Figure 4a) show a

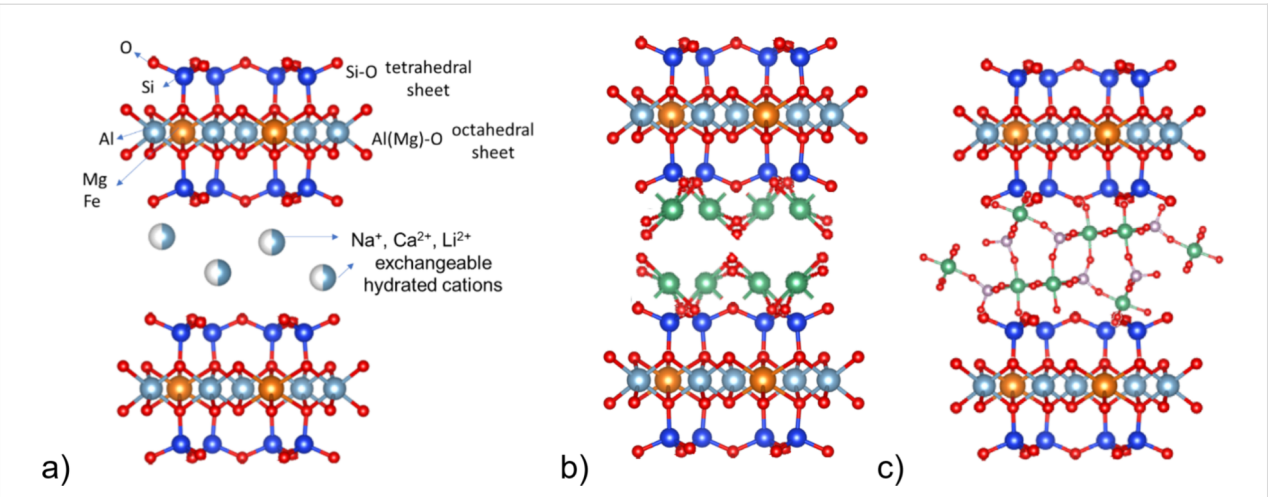


Figure 3: Schematic representation of bentonite clay (a), bentonite modified with NbOX (BeOx) (b), and bentonite modified with NbPh (BePh) (c). The structures were obtained with the Vesta program using the COD 1100106, COD 1534619, and COD 1517684 for montmorillonite, niobium oxide, and niobium phosphate, respectively.

band in the region of 1043 cm^{-1}, due to the vibrational mode (ν) of asymmetric stretching of the phosphate ion.

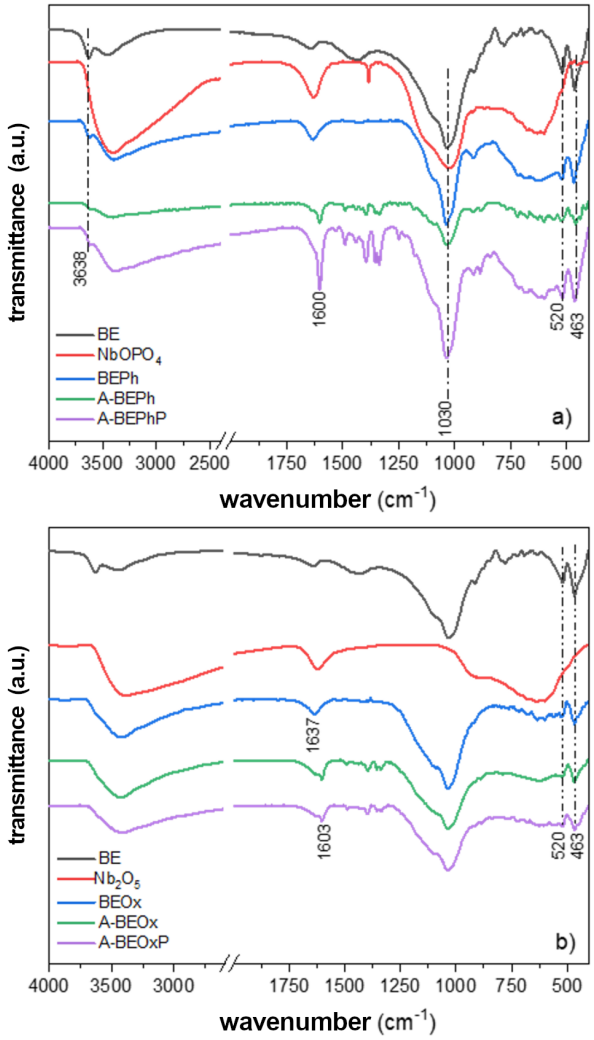


Figure 4: FTIR spectra for the bentonite samples modified with niobium phosphate (a) and niobium oxide (b).

The broad band in the region of 3385 cm^{-1} and the narrow band in the region of 1600 or 1637 cm^{-1} present in the spectrum for BE and the clay samples modified with $NbOPO_4$ and Nb_2O_5 are attributed to the stretching of hydroxyl and angular deformation of the water molecule, respectively [7,17]. The band in the region of approximately 1115 cm^{-1} is related to the stretching vibrations of Si–O. Bands in the region of 520 and 463 cm^{-1}, which appear in all spectra of bentonite and bentonite modified with niobium, are attributed to the stretching and bending of Si–O present in the clay layers [7].

The spectra for Nb_2O_5 and $NbOPO_4$ and the bentonite modified with niobium before and after adsorption/photocatalysis present an intense band in the region of 630 cm^{-1} related to the stretching of the Nb–O bond. The A-BEPh, A-BEPhP, A-BEOx, and A-BEOxP samples exhibit a set of bands in the region from 1477 to 1277 cm^{-1} typical for the identification of the MB dye, indicating the presence of the dye in the clay structure [18].

Figure 5 shows the XPS analysis of niobium in BEOx and BEPh samples (Figure 4a and Figure 4b, respectively). The Nb 3d spectra exhibit two distinct peaks centered at 207.5 and 210.2 eV, corresponding to Nb $3d_{5/2}$ and Nb $3d_{3/2}$, respectively, indicative of niobium +5. The O 1s XPS spectra are shown in Figure 5c for BEOx and Figure 5d for BEPh. The spectra of samples BEOx and BEPh are reproduced with two components centered at 530.9 and 533.5 eV. The component centered at 531.0 eV can be attributed to photoelectrons emitted from oxygen atoms in Si–O, Al–O, or Nb–O bonds, whereas the low-intensity component at a higher binding energy can be associated with the hydroxyl OH^- group of Nb–OH located in the interlayer region of the clay. These results confirm the increased interlayer space of the clay observed in DRX results (Figure 2). Figure 5e shows the O 1s spectrum recorded on sample BE. The high-intensity component centered at 532.0 eV is associated with oxygen bonds in Si–O–Si bonds [12].

Table 1 presents the chemical compositional analysis of the samples BE, BEOx, and BEPh determined by XPS. The results indicate that the bentonite clay modified with niobium phosphate (BEPh) exhibits a phosphorous content of 2.0% (wt %), thereby confirming the successful modification of the clay with this niobium compound. Furthermore, the samples BEOx and BEPh displayed niobium relative concentrations of 6.4 wt % and 4.0 wt %, respectively. These results suggest the incorporation of niobium into the clay matrix. In Table 1, considering the montmorillonite phase with the empirical formula $M_x(Al_{4-x}Mg_x)Si_8O_{20}(OH)_4$, when it was modified with the niobium compounds, the element sodium had its percentage decreased compared with that in the bentonite sample. However, the little change in the percentage of aluminum and silica, corresponding to the octahedral and tetrahedral layer, respectively, confirms that the niobium compounds are exchanged with sodium counter ions.

In recent years, laser-induced breakdown spectroscopy, an optical emission spectroscopic technique, has emerged as a rapid qualitative and quantitative analysis [19]. This spectroscopic technique can be explained by the short-duration, high-intensity pulsed laser being focused on a material, producing a plasma called laser-induced plasma (LIP). Qualitative and quantitative information about a sample is obtained by measuring the spectral delivery of the laser-induced plasma [19].

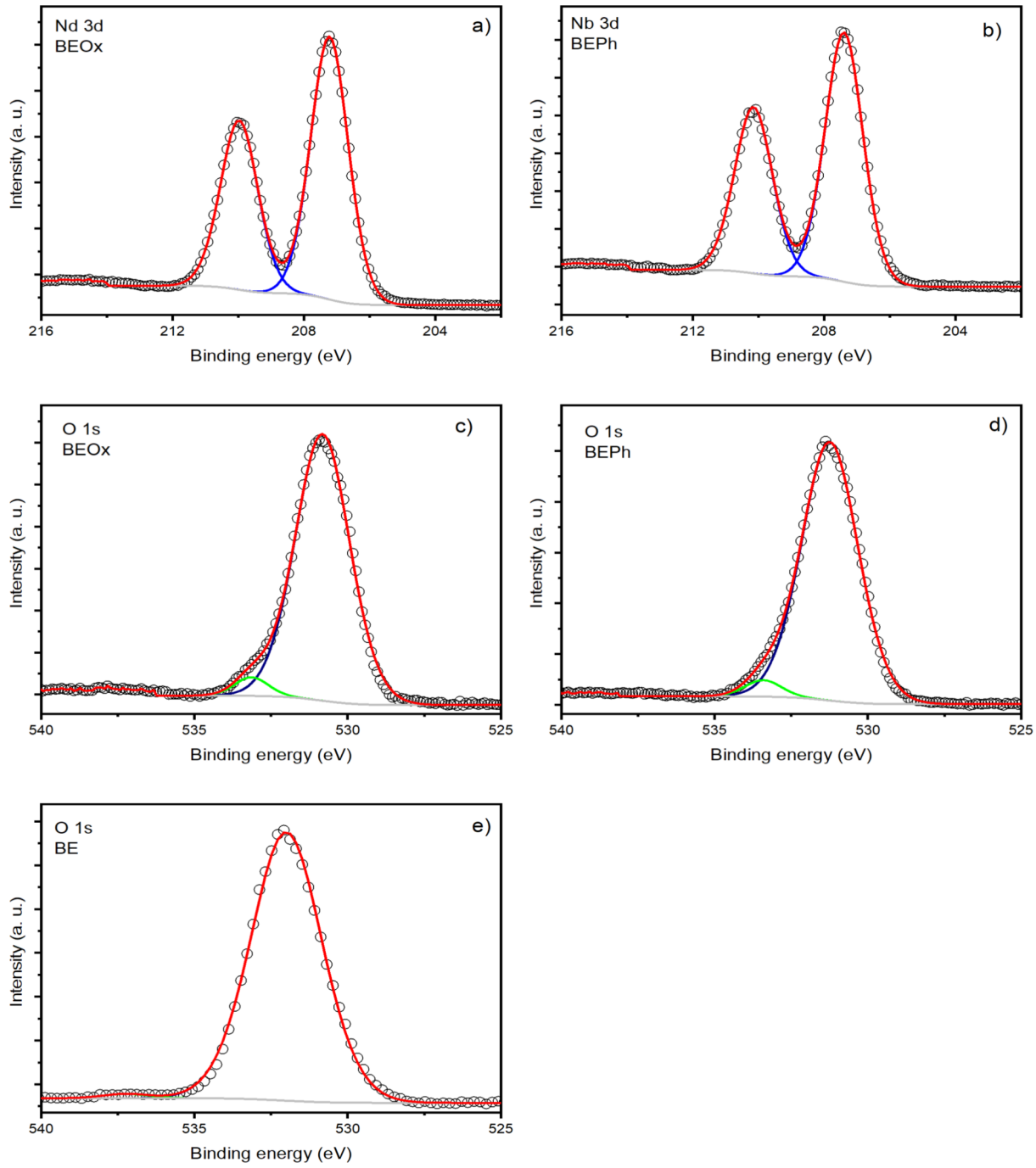


Figure 5: Photoelectron spectroscopy results for Nb3d (a and b for the samples BEOx and BEPh, respectively), O 1s (c, d, and e for the samples BEOx, BEPh, and BE, respectively).

Figure 6 shows LIBS spectra for the samples BE, BEPh, and BEOx. It is observed that the samples containing niobium show a higher density of spectral lines. For the sample BE, the principal emissions lines for Mg^{2+}, Al^{3+}, Na^{+}, at around 279 nm, 309 nm and 589 nm, respectively, are consistent with the montmorillonite structure, and these results are coherent with XPS composition in Table 1. The modification of the clay samples with niobium was characterized by the presence of many other lines throughout the spectrum region, which highlighted the lines at 666 nm. XPS analysis (Table 1), as well as the XRD results (Figure 2), suggest that the niobium compounds ($NbOPO_4$ and Nb_2O_5) were exchanged with Na^{+} ions of the clay, due to the decreased percentage of these elements in XPS composition as observed in Figure 5. The LIBS results showed

Table 1: Composition of the samples BE, BEOx, and BEPh determined by XPS.

Samples	wt %											
	C	N	O	F	Na	Mg	Al	Si	P	Ca	Nb	Fe
BEOx	6.4	–	62.5	1.1	2.6	2.1	4.8	13.1	–	1.0	6.4	–
BEPh	7.9	1.5	62.7	1.0	1.7	1.3	4.4	12.5	2.0	1.0	4.0	–
BE	9.3	–	55.0	–	6.0	3.8	6.5	17.5	–	1.4	–	0.5

the presence of lines of Mg and Na for the BE sample, at around 280 nm and 819 nm, respectively. As demonstrated in Table 1, the compositions of Na were reduced when the BE sample was modified with niobium compounds.

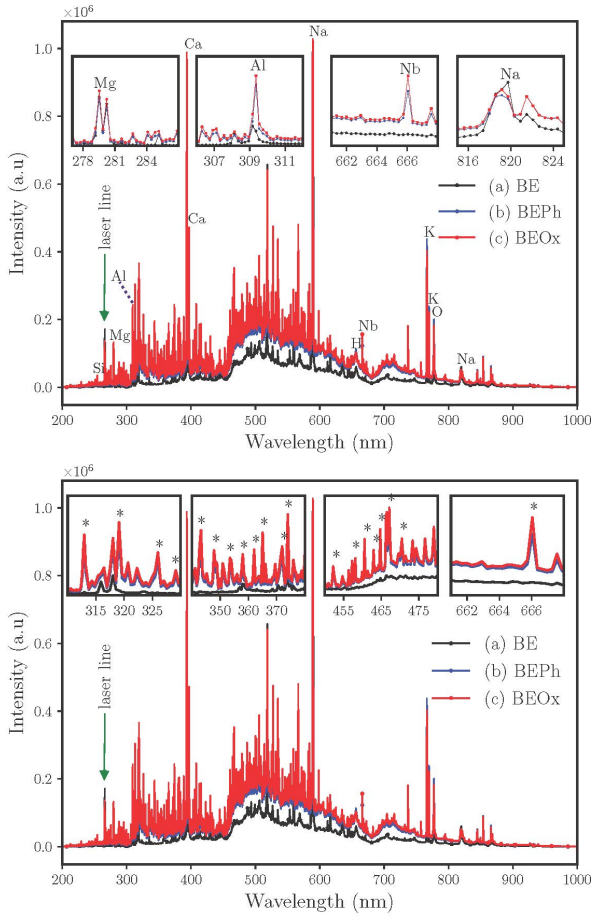


Figure 6: Laser-induced breakdown spectroscopy analysis for the samples BE (a), BEPh(b) and BEOx (c).

The average particle size for the samples BE, NbPh, and NbOx were 12, 410, and 54 µm, respectively, and it is present in Supporting Information File 1, Figure S1. The BEPh and BEOx samples presented different particle size distributions, so the average particle size (D50) for them was 4.52 and 86 µm, respectively. These values indicate that the clay aggregates are dissociated and well dispersed, as shown in the study by Yang et al. [20].

The absorbance spectra profiles in the visible region for the bentonite samples and bentonite modified with niobium are presented in Figure 7. It can be observed that the $NbOPO_4$ and Nb_2O_5 powder samples do not show an absorption band. However, the bentonite modified with these compounds exhibited a band with a maximum of 493 nm. The samples BEOx and BEPh obtained after adsorption/photocatalysis present profiles like BE clay, with intense absorption in the UV region with a

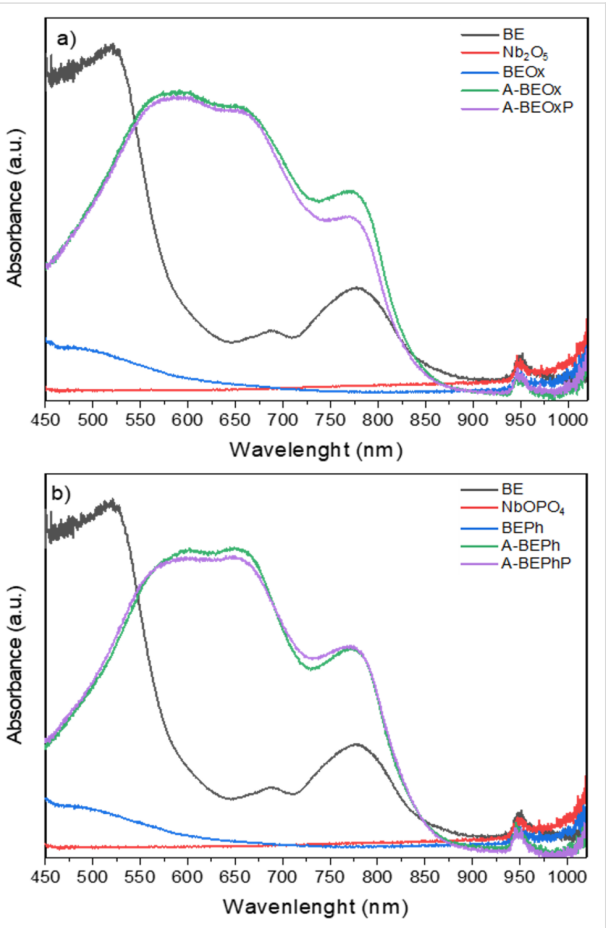


Figure 7: The absorption spectra in the visible region for the samples of bentonite and their modifications with niobium oxide (a) and niobium phosphate(b).

sharp drop of around 550 nm [8]. This fact indicates the feasibility of activating the A-BEPh, A-BEPhP, A-BEOx, and A-BEOXPh samples under visible light (above 400 nm) [8].

The indirect bandgap energy values for the BE, $NbOPO_4$ and Nb_2O_5 and the bentonite clay modified with niobium BEPh and BEOx samples were estimated by the Tauc method [21]. For this, Kubelka–Munk method was applied as observed in Supporting Information File 1, Figure S2. The bandgap value of the BE sample (3.2 eV) was slightly higher than for the $NbOPO_4$ and Nb_2O_5 compounds (3.13 and 3.2 eV, respectively). The calculated bandgap is coherent with the literature, Nakhaei et al. (2019) [22] obtained a value of 3.6 eV for bentonite clay, and for the niobium compounds Ücker et al. 2018 obtained the values of a bandgap equal to 3.0 eV [23]. The bentonite clay samples modified with niobium (BEOx and BEPh) remained with bandgap values lower compared with the clay, 3.07 and 3.13 eV, respectively. These values are consistent with the results of the study by Ascencios et al. 2019 [8] in which obtained bandgap values to clay/Nb were around 3.0 and 3.38 eV. The small decrease in values occurred due to the bentonite clay with high bandgap values, which generated impurity energy levels above the valence band edge. This results in lower energy values required to excite charge carriers, reducing the optical band [24].

Figure 8 shows the results of the comparison obtained regarding the percentage of removal from adsorption and heterogeneous photocatalysis tests. The photocatalysis mechanism can be explained as follows: a semiconductor such as the BEPh and

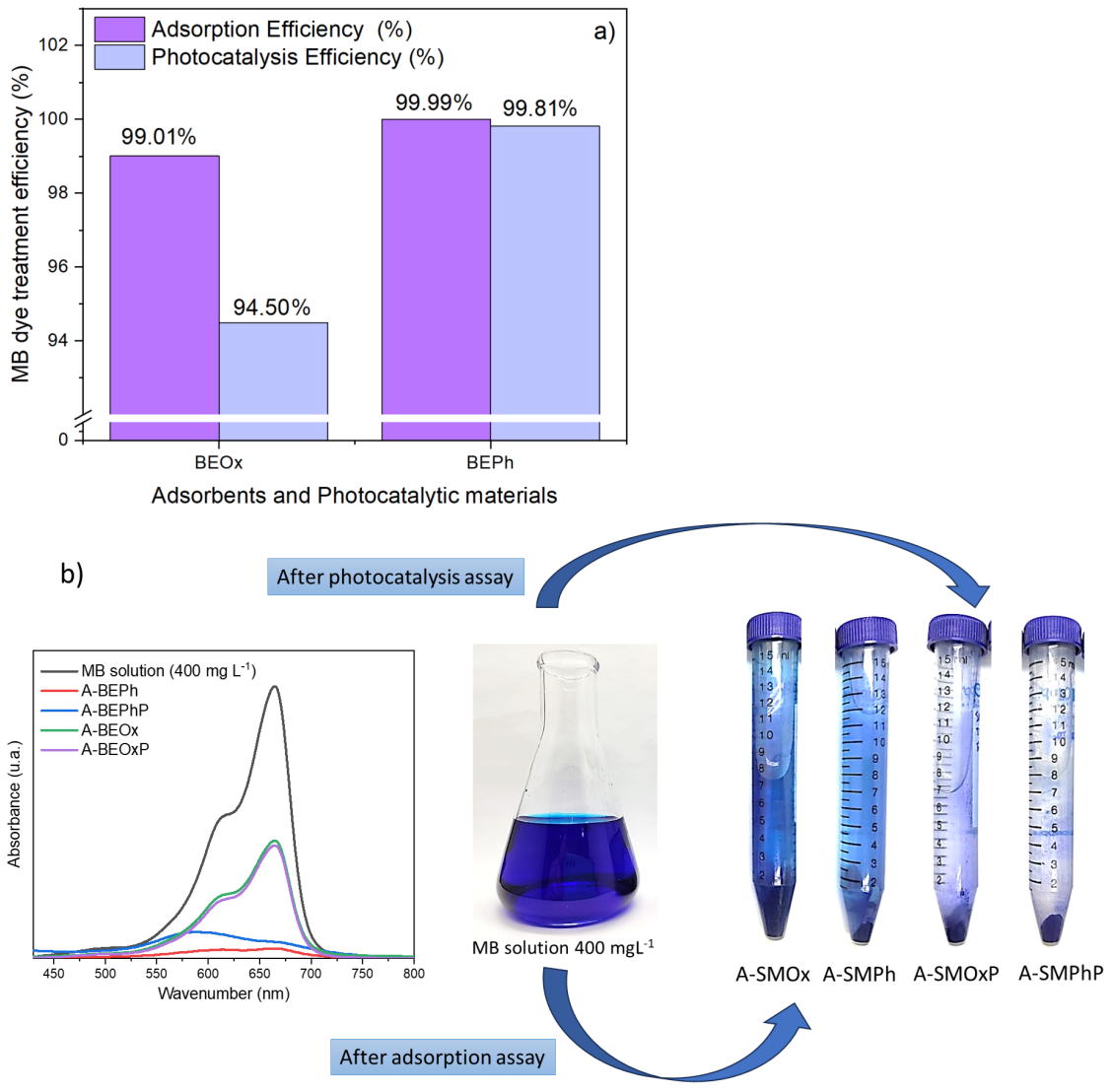


Figure 8: Adsorption and photocatalysis efficiency (a) and UV–vis spectra following the digital images of the MB solutions after adsorption and photocatalysis assays (b) using the starting materials BEOx and BEPh.

BEOx samples absorbs a photon, promoting an electron from the valence band (V_B) to the conduction band (C_B), creating a hole in the valence band (h_{BV}^+) [8]. These holes induce the oxidative decomposition of organic molecules adsorbed on the catalytic surface. They also react with water molecules, producing the hydroxyl radical ($OH^•$). This radical rapidly attacks the dye molecules in the solution, leading to mineralization into CO_2 and H_2O [8].

According to the observed results, the BEOx and BEPh samples notably exhibited higher efficiency in the adsorption process (99.01% and 99.99%, respectively) than in photocatalysis. This phenomenon can be attributed to the negative surface charge of the modified clays BEOx and BEPh, which exhibit a strong affinity with the positively charged structure of the MB dye. On the other hand, the BEOx and BEPh samples demonstrated significant efficacy in MB removal, with removal rates of 94.5% and 99.81%, respectively. The preferential electron–hole (h_{BV}^+) favoring of the BEOx catalyst hindered its photocatalytic activity [8].

In a study by Asencios et al. (2019) [8], niobium-modified clay was explored for the photocatalysis of rhodamine B dye, yielding removal rates close to 95%. Additionally, Lacerda et al. (2020) [25] achieved up to 90% efficiency in the removal of reactive blue 19 dye using niobium-modified bentonite. These reports demonstrate that the material obtained in this study presents high values of MB removal under UV light, standing out as a novel material.

The absorbance profiles of the niobium-modified samples dispersed in clear paint are shown in Supporting Information File 1, Figure S3. It is possible to observe that the BEOx and BEPh samples dispersed in clear paint, despite presenting a yellow coloration, did not show absorption bands. The samples collected after the adsorption/photocatalysis assays exhibited bands in the maximum region at 664 nm, corresponding to the $\pi \rightarrow \pi^*$ electronic transitions of the adsorbed MB dye [26].

Table 2 and Table 3 and Supporting Information File 1, Figures S4 and S5 present the values of the CIEL*a*b* colorimetric parameters for the samples BEOx and BEPh (powder sample, cycle) even as they disperse in colorless paint (paint sample, square), respectively. The tables also include color difference values between the samples in powder form and those dispersed in colorless paint. Colorless paint does not contain white pigment in its matrix, enhancing the dispersed pigment color. The ΔE parameter quantified the color difference between two samples, BEOx and BEPh, in powder form and those dispersed in colorless paint. As observed, the results of ΔE show that the samples A-BEPhP (12.17) and BEOx (9.82) before the adsorption/photocatalysis process when dispersed in colorless paint demonstrate a strong color parameter difference (ΔE = 6–12). The ΔE values obtained for the samples BEPh (13.62) before the adsorption/photocatalysis process, A-BEPh (23.38), A-BEOx (15.97), and A-BEOxP (13.80) were above 12, indicating a very strong color parameter difference [27].

The colorimetric parameters presented in Table 2 and Table 3 and in Supporting Information File 1, Figures S2 and S3 demonstrate that the test specimens painted with niobium-modified clay before the adsorption/photocatalysis of MB show higher luminosity (L). When the clay samples were colored MB, after the adsorption/photocatalysis process, the luminosity decreased. The A-BEPhP sample shows a slight tendency towards green coloration (-a*). On the other hand, when evaluating the b* parameter, it is observed that all samples obtained after adsorption/photocatalysis of MB (A-BEPh, A-BEPhP, A-BEOx and A-BEOxP), whether in powder form or dispersed in paint, show a tendency towards blue coloration, as observed in the negative b* values.

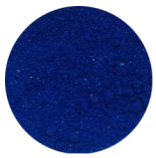
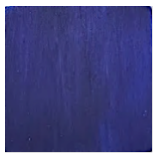
The BEPh, BEOx, A-BEPh, A-BEOx, A-BEPhP, and A-BEOxP samples were evaluated for their in vitro antibacterial capacity using the minimum inhibitory concentration (MIC) method against the pathogenic bacteria *Proteus mirabilis* and *Bacillus cereus*. The results obtained are presented in Table 4.

The samples A-BEPh, A-BEPhP, A-BEOx, and A-BEOxP demonstrated antibacterial activity against the *Proteus mirabilis* bacterial strains, with MIC values recorded at 0.31, 0.15, 0.31, and 0.62 mg/mL, respectively. In contrast, the BEPh and BEOx samples exhibited no inhibitory effects at the tested concentrations for this microorganism.

Observing the adsorption and photocatalysis efficiency in Figure 8a, similar values for the samples BEPhP and BEPh were obtained (99.81% and 99.81%, respectively) that is, the amount of dye present in these samples is practically the same. The MIC results of these samples indicated 0.15 mg/mL and 0.31 mg/mL for the samples A-BEPhP and A-BEPh, respectively. The adsorption and photocatalysis efficiency for the samples BEOxP and BEOx were 94.50% and 99.01%, respectively. These results suggest that sample A-BeOX contains a larger amount than sample A-BePh. The A-BEOxP sample yielded an MIC of 0.62 mg/mL, while the A-BEOx had an MIC of 0.31 mg/mL, indicating a more effective antibacterial action against the tested strains.

It is noteworthy that antibacterial activity was only observed in materials that had the addition of methylene blue, highlighting the influence of the dye on the assay outcomes. According to

Table 2: Colorimetric parameters obtained by the CIEL*a*b* system for the BEPh samples before and after the adsorption/photocatalysis assays in powder form (circle) and dispersed in colorless paint (square).

Sample	Colorimetric parameters						Images of the sample
	L*	a*	b*	C*	h	Δ*E*	
BEPh	77.02	2.47	10.38	10.67	76.67	–	
BEPh	90.54	2.19	12.03	12.23	68.01	13.62	
A-BEPh	13.45	4.91	–36.34	36.67	277.69	–	
A-BEPh	32.05	3.15	–22.29	22.51	278.05	23.38	
A-BEPhP	31.91	–5.08	–21.03	21.63	256.42	–	
A-BEPhP	32.98	5.97	–26.01	26.68	282.92	12.17	

Thesnaar (2021) [28], many studies have demonstrated that methylene blue, either alone or in combination with other compounds, possesses antibacterial activity; however, the precise mechanism of action remains unclear. The BEPh, BEOx, A-BEPh, A-BEOx, A-BEPhP, and A-BEOxP samples did not exhibit minimum inhibitory activity against the other studied bacterial strain *Bacillus cereus*.

These results highlight the selectivity of the studied samples (A-BEPh, A-BEPhP, A-BEOx, and A-BEOxP) in inhibiting Gram-negative bacteria, which typically exhibit increased resistance due to the presence of an outer membrane that protects them from certain antimicrobial agents [29]. Therefore, the preliminary results indicate that bentonite clay modification with niobium oxide (BEOx) and niobium phosphate (BEPh), when adsorbed and/or photocatalyzed for the treatment of wastewater containing MB, demonstrates promising selective antibacterial activity against Gram-negative bacteria.

Conclusion

In conclusion, the presented study demonstrates that the modification of bentonite clay with niobium phosphate and niobium oxide can be achieved through a simple and low-cost procedure. The XRD results revealed that the raw bentonite contains additional phases such as kaolinite and quartz. The niobium incorporated into bentonite clay (BEPh and BEOx) indicated that the

Table 3: Colorimetric parameters obtained by the CIEL*a*b* system for the BEPh samples before and after the adsorption/photocatalysis assays in powder form (circle) and dispersed in colorless paint (square).

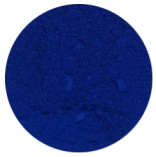
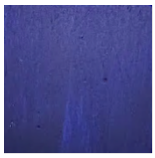
Sample	Colorimetric parameters						Images of the sample
	L	a*	b*	C*	h	Δ*E*	
BEOx	80.96	3.07	13.17	11.05	73.85	–	
BEOx	90.42	0.71	12.03	9.63	85.78	9.82	
A-BEOx	22.91	13.94	–36.80	39.55	290.74	–	
A-BEOx	30.93	6.79	–24.99	25.90	285.20	15.97	
A-BEOxP	18.25	7.90	–30.06	31.00	284.72	–	
A-BEOxP	30.65	7.15	–24.06	25.10	286.54	13.80	

Table 4: MIC (mg/mL) for the in vitro antibacterial activity in water.

Sample	BEPh	BEOx	A-BEPh	A-BEOx	A-BEPhP	A-BEOxP
MIC *P. mirabilis*	–[a]	–[a]	0.31	0.31	0.15	0.62

[a]MIC values were not determined.

niobium modification did not destroy the structure of the montmorillonite layer, as indicated by the XRD results. Furthermore, analyses using XPS and LIBS confirmed that the niobium compounds exchanged with Na^+ ions of the clay tetrahedral sheet.

The bentonite sample, along with the BEPh and BEOx samples, exhibited adsorption and photocatalytic efficiencies exceeding 94% for the removal of MB in water. This process resulted in a final blue-colored product as evidenced by the colorimetric pa-

rameters obtained through the CIEL*a*b* color space. The samples derived from the adsorption/photocatalysis tests (A-BEPh, A-BEPhP, A-BEOx, and A-BEOxP) demonstrate significant antibacterial activity against the Gram-negative bacteria *Proteus mirabilis*, highlighting the influence of the dye in the assay outcomes.

The implications of this work extend to the development of a novel hybrid pigment. This pigment, synthesized from abundant natural clays of the Guarapuava region in conjunction with niobium, an abundant metal in Brazil, is easily synthesized, cost-effective, and has potential to be used as a pigment in commercial paints. Moreover, it exhibits antibacterial properties against pathogens responsible for various diseases, including ocular and ear infections.

Supporting Information

Supporting Information File 1

Additional figures.
[https://www.beilstein-journals.org/bjnano/content/supplementary/2190-4286-16-13-S1.pdf]

Acknowledgements

The authors also thank Dr. Andressa dos Santos for the colorimetric analysis. The structural drawings contained in the Graphical Abstract were produced using the VESTA software (Version 3), https://jp-minerals.org/vesta/en/download.html [28].

Funding

The authors would like to thank the following agencies for their support: Capes, CNPq, Finep, and Fundação Araucaria. S.J. is thankful for a CNPq PDJ post-doctorate grant (152230/2022-0).

Author Contributions

Silvia Jaerger: conceptualization; data curation; formal analysis; investigation; methodology; project administration; resources; validation; visualization; writing – original draft; writing – review & editing. Patricia Appelt: conceptualization; data curation; formal analysis; investigation; methodology; validation; writing – original draft; writing – review & editing. Mario Antônio Alves da Cunha: investigation; methodology; visualization. Fabián Ccahuana Ayma: data curation; methodology; software. Ricardo Schneider: data curation; formal analysis; methodology; software; validation; visualization; writing – original draft; writing – review & editing. Carla Bittencourt: conceptualization; data curation; formal analysis; investigation; methodology; visualization; writing – original draft; writing – review & editing. Fauze Jacó Anaissi: conceptualization; data curation; formal analysis; investigation; methodology; project administration; supervision; validation; visualization; writing – original draft; writing – review & editing.

ORCID® iDs

Patricia Appelt - https://orcid.org/0000-0003-4302-534X
Fabián Ccahuana Ayma - https://orcid.org/0000-0002-5610-0559
Ricardo Schneider - https://orcid.org/0000-0001-9501-8489
Carla Bittencourt - https://orcid.org/0000-0002-3330-6693
Fauze Jacó Anaissi - https://orcid.org/0000-0002-5454-472X

Data Availability Statement

Data generated and analyzed during this study is available from the corresponding author upon reasonable request.

Preprint

A non-peer-reviewed version of this article has been previously published as a preprint: https://doi.org/10.3762/bxiv.2024.59.v1

References

1. Saber-Samandari, S.; Saber-Samandari, S.; Joneidi-Yekta, H.; Mohseni, M. *Chem. Eng. J.* **2017,** *308,* 1133–1144. doi:10.1016/j.cej.2016.10.017
2. Bingül, Z. *J. Mol. Struct.* **2022,** *1250,* 131729. doi:10.1016/j.molstruc.2021.131729
3. Nayl, A. A.; Abd-Elhamid, A. I.; Arafa, W. A. A.; Ahmed, I. M.; AbdEl-Rahman, A. M. E.; Soliman, H. M. A.; Abdelgawad, M. A.; Ali, H. M.; Aly, A. A.; Bräse, S. *Materials* **2023,** *16,* 514. doi:10.3390/ma16020514
4. Ma, L.; Islam, S. M.; Xiao, C.; Zhao, J.; Liu, H.; Yuan, M.; Sun, G.; Li, H.; Ma, S.; Kanatzidis, M. G. *J. Am. Chem. Soc.* **2017,** *139,* 12745–12757. doi:10.1021/jacs.7b07123
5. Li, K.; Zheng, Z.; Feng, J.; Zhang, J.; Luo, X.; Zhao, G.; Huang, X. *J. Hazard. Mater.* **2009,** *166,* 1180–1185. doi:10.1016/j.jhazmat.2008.12.035
6. Akhtar, J.; Amin, N. A. S.; Shahzad, K. *Desalin. Water Treat.* **2016,** *57,* 12842–12860. doi:10.1080/19443994.2015.1051121
7. Rocha, M. L. M.; Balaba, N.; Jaerger, S.; Primo, J. O.; Horsth, D. F. L.; Appelt, P.; Meneguzzi, D.; Cunha, M. A. A.; Anaissi, F. J. *Minerals (Basel, Switz.)* **2023,** *13,* 785. doi:10.3390/min13060785
8. Asencios, Y. J. O.; Quijo, M. V.; Marcos, F. C. F.; Nogueira, A. E.; Rocca, R. R.; Assaf, E. M. *Sol. Energy* **2019,** *194,* 37–46. doi:10.1016/j.solener.2019.10.005
9. *M 07 Methods for Dilution Methods for Dilution Antimicrobial Susceptibility Tests for Bacteria that Grow Aerobically,* 11th ed.; Clinical and Laboratory Standards Institute (CLSI): Wayne, PA, USA, 2018.
10. Balouiri, M.; Sadiki, M.; Ibnsouda, S. K. *J. Pharm. Anal.* **2016,** *6,* 71–79. doi:10.1016/j.jpha.2015.11.005
11. Chen, J.; Lu, J.; Su, L.; Ruan, H.; Zhao, Y.; Lee, C.; Cai, Z.; Wu, Z.; Jiang, Y. *Appl. Sci.* **2022,** *12,* 3182. doi:10.3390/app12063182
12. Marin, L. M.; Hallett-Tapley, G. L.; Impellizzeri, S.; Fasciani, C.; Simoncelli, S.; Netto-Ferreira, J. C.; Scaiano, J. C. *Catal. Sci. Technol.* **2014,** *4,* 3044–3052. doi:10.1039/c4cy00238e

13. Liang, F.; Wu, D.; Jiang, L.; Zhang, Z.; Zhang, W.; Rui, Y.; Tang, B.; Liu, F. *ACS Appl. Mater. Interfaces* **2021,** *13,* 51057–51065. doi:10.1021/acsami.1c15763
14. Qiu, G.; Huang, C.; Sun, X.; Chen, B. *Green Chem.* **2019,** *21,* 3930–3939. doi:10.1039/c9gc01225g
15. Gallo, J. M. R.; Teixeira, S.; Schuchardt, U. *Appl. Catal., A* **2006,** *311,* 199–203. doi:10.1016/j.apcata.2006.06.019
16. Madejová, J. *Vib. Spectrosc.* **2003,** *31,* 1–10. doi:10.1016/s0924-2031(02)00065-6
17. Zhang, Y.; Wang, J.; Ren, J.; Liu, X.; Li, X.; Xia, Y.; Lu, G.; Wang, Y. *Catal. Sci. Technol.* **2012,** *2,* 2485–2491. doi:10.1039/c2cy20204b
18. Raiyaan, G. I. D.; Kalith, S. B. M.; Sheriff, M. A.; Arunachalam, K. D. *J. Aquacult. Mar. Biol.* **2021,** *10,* 146–150. doi:10.15406/jamb.2021.10.00316
19. Singh, P.; Mal, E.; Khare, A.; Sharma, S. *J. Cult. Heritage* **2018,** *33,* 71–82. doi:10.1016/j.culher.2018.03.011
20. Yang, T.; Wang, N.; Gu, H. *Appl. Clay Sci.* **2023,** *235,* 106866. doi:10.1016/j.clay.2023.106866
21. Borth, K. W.; Galdino, C. W.; Teixeira, V. d. C.; Anaissi, F. J. *Appl. Surf. Sci.* **2021,** *546,* 149126. doi:10.1016/j.apsusc.2021.149126
22. Nakhaei, M.; Barzgari, Z.; Mohammadi, S. S.; Ghazizadeh, A. *Res. Chem. Intermed.* **2019,** *45,* 4995–5005. doi:10.1007/s11164-019-03877-2
23. Ücker, C. L.; Gularte, L. T.; Fernandes, C. D.; Goetzke, V.; Moreira, E. C.; Raubach, C. W.; Moreira, M. L.; Cava, S. S. *J. Am. Ceram. Soc.* **2019,** *102,* 1884–1892. doi:10.1111/jace.16080
24. Zainab, S.; Azeem, M.; Awan, S. U.; Rizwan, S.; Iqbal, N.; Rashid, J. *Sci. Rep.* **2023,** *13,* 6954. doi:10.1038/s41598-023-33200-4
25. Hass Caetano Lacerda, E.; Monteiro, F. C.; Kloss, J. R.; Fujiwara, S. T. *J. Photochem. Photobiol., A* **2020,** *388,* 112084. doi:10.1016/j.jphotochem.2019.112084
26. Kostjukova, L. O.; Leontieva, S. V.; Kostjukov, V. V. *J. Mol. Liq.* **2021,** *336,* 116369. doi:10.1016/j.molliq.2021.116369
27. Quindici, M. *O Segredo das Cores;* All Print: São Paulo, Brazil, 2013.
28. Thesnaar, L.; Bezuidenhout, J. J.; Petzer, A.; Petzer, J. P.; Cloete, T. T. *Eur. J. Pharm. Sci.* **2021,** *157,* 105603. doi:10.1016/j.ejps.2020.105603
29. Ramachandran, G. *Virulence* **2014,** *5,* 213–218. doi:10.4161/viru.27024

License and Terms

This is an open access article licensed under the terms of the Beilstein-Institut Open Access License Agreement (https://www.beilstein-journals.org/bjnano/terms), which is identical to the Creative Commons Attribution 4.0 International License (https://creativecommons.org/licenses/by/4.0). The reuse of material under this license requires that the author(s), source and license are credited. Third-party material in this article could be subject to other licenses (typically indicated in the credit line), and in this case, users are required to obtain permission from the license holder to reuse the material.

The definitive version of this article is the electronic one which can be found at:
https://doi.org/10.3762/bjnano.16.13

BEILSTEIN JOURNAL OF NANOTECHNOLOGY

Emerging strategies in the sustainable removal of antibiotics using semiconductor-based photocatalysts

Yunus Ahmed[*1,§], Keya Rani Dutta[1], Parul Akhtar[1], Md. Arif Hossen[2], Md. Jahangir Alam[3], Obaid A. Alharbi[4], Hamad AlMohamadi[5] and Abdul Wahab Mohammad[6]

Review

Open Access

Address:
[1]Department of Chemistry, Chittagong University of Engineering and Technology, Chattogram-4349, Bangladesh, [2]Institute of River, Harbor and Environmental Science, Chittagong University of Engineering and Technology, Chattogram-4349, Bangladesh, [3]Department of Civil Engineering, Chittagong University of Engineering and Technology, Chattogram-4349, Bangladesh, [4]Water Management & Treatment Technologies Institute, Sustainability & Environment Sector, King Abdulaziz City for Science and Technology (KACST), Riyadh, 11442, Saudi Arabia, [5]Department of Chemical Engineering, Faculty of Engineering, Islamic University of Madinah, Madinah 42351, Saudi Arabia and [6]Chemical and Water Desalination Engineering Program, College of Engineering, University of Sharjah, Sharjah 27272, United Arab Emirates

Email:
Yunus Ahmed[*] - yunusahmed@cuet.ac.bd

* Corresponding author
§ H/P: +8801833512231

Keywords:
antibiotics; degradation pathways; heterojunctions; mechanisms; photocatalysts; semiconductor

Beilstein J. Nanotechnol. **2025,** *16,* 264–285.
https://doi.org/10.3762/bjnano.16.21

Received: 27 July 2024
Accepted: 24 January 2025
Published: 25 February 2025

This article is part of the thematic issue "Advanced functional nanomaterials for water remediation applications".

Associate Editor: C. T. Yavuz



© 2025 Ahmed et al.; licensee Beilstein-Institut.
License and terms: see end of document.

Abstract

In the constantly growing field of environmental sustainability, the threat of newly discovered pollutants, particularly antibiotics, has become a crucial concern. The widespread presence of these pharmaceutical substances in water sources presents a complex hazard to human health and ecological balance, requiring immediate and novel intervention techniques. Regarding this, semiconductor-based photocatalysts have appeared as promising candidates, providing a sustainable and efficient way to remove antibiotics from aquatic ecosystems. Nanomaterials can effectively and precisely break down and neutralize antibiotic compounds with high efficiency and selectivity by utilizing a complex interaction between radical reactive oxygen species and non-radical equivalents under light irradiation. Although photocatalysts have certain drawbacks, such as a limited capacity to absorb light and concerns about catalytic stability, photocatalysis outperforms other advanced oxidation processes in multiple aspects. This study focuses on summarizing recent advances in the sustainable removal of antibiotics using semiconductor-based photocatalysts. By reviewing the latest studies and sustainable technologies, this study presents new insights into the complex relationship between contaminants and catalytic degradation processes. Compared to single and binary photocatalysts, modified ternary composites were found to have su-

perior photodegradation performance under visible light exposure. To be specific g-C_3N_4-based ternary photocatalysts exhibited more than 90% degradation of tetracycline and sulfamethazine antibiotics within one hour of irradiation. This study addresses the antibiotic degradation efficiency during photocatalytic processes and suggests new approaches to improve the performance and scalability for wider use in real-world situations.

Introduction

Antibiotics are chemical substances used to treat bacterial infections in humans, animals, aquaculture, and livestock feed [1]. Their global use has increased significantly, reaching an estimated 100,000 to 200,000 tonnes between 2010 and 2019 [2], with approximately half designated for animal feed, projected to escalate to 105,596 tonnes by 2030 [3,4]. The widespread and often excessive use of antibiotics has raised public concern, especially because they are environmental contaminants originating from human and animal waste [5]. These antibiotics can persist without change or as active metabolites in the environment, posing significant toxicity risks to aquatic and human life [6-8]. The continuous presence of antibiotics in natural environments can contribute to the development of antibiotic-resistant bacteria (ARBs) and their resistance genes (ARGs), hastening the spread of antibiotic resistance [9,10]. Several studies have reported that this situation poses significant risks to human health and ecological systems [11-16]. Alarming projections in the USA anticipated that antimicrobial resistance-related deaths exceeding the combined toll of cancer and diabetes, with approximately 23,000 deaths annually [17].

For the mitigation of environmental hazards caused by antibiotics, several physical, biological, and chemical methods have been applied [13,18,19]. Various physical wastewater treatment techniques are based on mechanical separation to reduce contaminant levels by relocating rather than degrading antibiotics [7,8,20]. Biological approaches, such as the activated sludge process and biological membrane technologies, are commonly applied in wastewater treatment [21]. However, these technologies have come under scrutiny because of certain limitations, such as extended processing times and the generation of heat [22]. Conversely, chemical methods such as degradation and solid–liquid separation are also commonly used in making the pollutants non-toxic or non-hazardous [13,23]. It should be noted that many of the conventional methods fail in degrading antibiotics completely since most antibiotics are very complex in structure and are even resistant to biodegradation in an aquatic medium [24]. As a result, antibiotics have been found in different water sources from rivers to lakes, streams, and groundwater sources in many regions. Advanced oxidation processes (AOPs) have lately arisen as very effective treatment technology that has proven to remove antibiotics more effectively than the previous methods of physical adsorption, flocculation, and chemical oxidation [7,8,25]. AOPs offer several advantages, including simple equipment, straightforward operation, minimal sludge production, and the rapid generation of mineralized products. Additionally, they are highly effective in degrading high-strength organic and refractory chemicals [26]. Photocatalyst-based AOPs represent a promising strategy for eliminating antibiotics from polluted water, providing several advantages over other oxidation techniques. By utilizing light energy to activate catalysts, these AOPs facilitate antibiotic degradation without extra chemical oxidants and with minimal harmful byproducts, promoting environmental sustainability [27]. Moreover, they exhibit high selectivity towards antibiotics while preserving water quality. Compared to other photocatalysts material, semiconductor-based photocatalysts often achieved superior efficiency and high mineralization rates, offering a comprehensive solution for antibiotic contamination (see below in Tables 1–6). The progressively increasing trend of publications and corresponding citations in recent times highlight the superiority of semiconductor-based photocatalysts for the degradation of antibiotics (Figure 1). The appeal of photocatalysis lies in its potential to achieve extensive mineralization, converting organic pollutants into harmless mineral compounds. Furthermore, its nonselective nature enables it to address a broad spectrum of contaminants, making it a versatile option for environmental remediation across various water and air treatment applications. These features collectively make photocatalysis an attractive approach for addressing pollution challenges in diverse settings.

In recent years, several significant review papers have focused on removing antibiotics through AOPs [28-30]. Articles explored specific AOP methods tailored for antibiotic remediation, such as H_2O_2-based AOP [29], Fenton-based AOPs [31], UV-based AOPs [32], UV/chlor(am)ine-based AOP [33], electrochemical-based AOP (EAOP) [34], persulfate and peroxymonosulfate-based AOPs [30] as well as catalytic degradation processes [35], graphene-based materials [36,37], and adsorption processes [7,8]. However, these papers primarily discuss the oxidizing agents or AOP processes and their efficiency in removing antibiotics without focusing on the detailed mechanisms of how these materials or processes degrade antibiotics. They do not address the entry of antibiotics into the environment, their adverse impact on human health and the environment, or the effects of each treatment process in relation to established industrial applications. As a result, there is a lack of

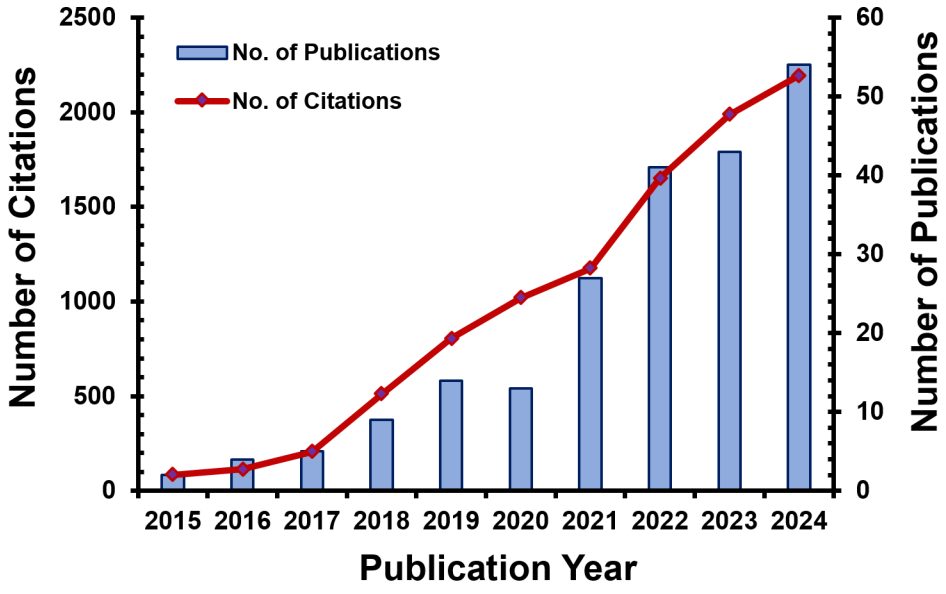


Figure 1: Publications and citations regarding antibiotic degradation using semiconductor-based photocatalysts (Scopus database).

understanding about these processes and their practical limitations for large-scale commercial wastewater treatment.

This review concentrates on semiconductor-based photocatalytic processes and their effectiveness in eliminating antibiotics while also addressing their practical constraints. The scope includes discussions on antibiotic sources, pollution risks and impacts, removal challenges, and influential factors. This study aims to provide readers with a comprehensive understanding of the principles and mechanisms underlying semiconductor-based photocatalysts and their modification for enhanced antibiotic degradation from contaminated water. The discussion also includes concluding remarks and future directions of emerging techniques for sustainable wastewater treatment.

Review

Sources of antibiotics

The primary sources of antibiotics in surface water include animal husbandry and aquaculture, domestic sewage discharges, pharmaceutical manufacturing, and healthcare facilities [38]. Antibiotics are commonly administered to animals through feed or water, primarily for growth promotion in large-scale animal farming operations and to prevent and treat infectious diseases [39]. Consequently, antibiotic residues are excreted by the animals in their feces, which can enter the environment by applying manure as fertilizer or runoff from animal housing facilities. Additionally, antibiotics are extensively used in aquaculture, where only a fraction (20–30%) of the pharmaceuticals used are absorbed by the animals [40]. Domestic sewage discharge represents a significant source of antibiotics in urban water systems [41]. Antibiotics are commonly prescribed to individuals to treat various infections. Yet, research indicates that only a small fraction of antibiotics administered to the body are absorbed and utilized by organisms. The remaining 40–90% of active medications or metabolites are excreted in feces and urine [42]. Consequently, treated wastewater or septic effluent containing residual antibiotics can be released into nearby water bodies [43]. Pharmaceutical companies generate, handle, and dispose of significant quantities of antibiotics during production. A study found that downstream water sources from pharmaceutical production plants had significantly higher antibiotic concentrations than upstream sources [44]. Hospitals and healthcare facilities also significantly contribute antibiotics to urban water systems [45]. These facilities administer large doses of antibiotics to patients, resulting in the excretion of antibiotic residues through wastewater. Medical waste incineration is a significant source of antibiotic emissions, potentially contributing to the spread of antibiotic resistance. The present study investigates several primary sources of environmental antibiotics, as illustrated in Figure 2. It provides a comprehensive analysis of their pathways and the mechanisms influencing their movement and persistence in environmental systems.

Challenges of removing antibiotics from the environment

The challenge of removing antibiotics from the environment, including water bodies, soil, and wastewater, is commonly called the antibiotic removal problem. Antibiotics present in the

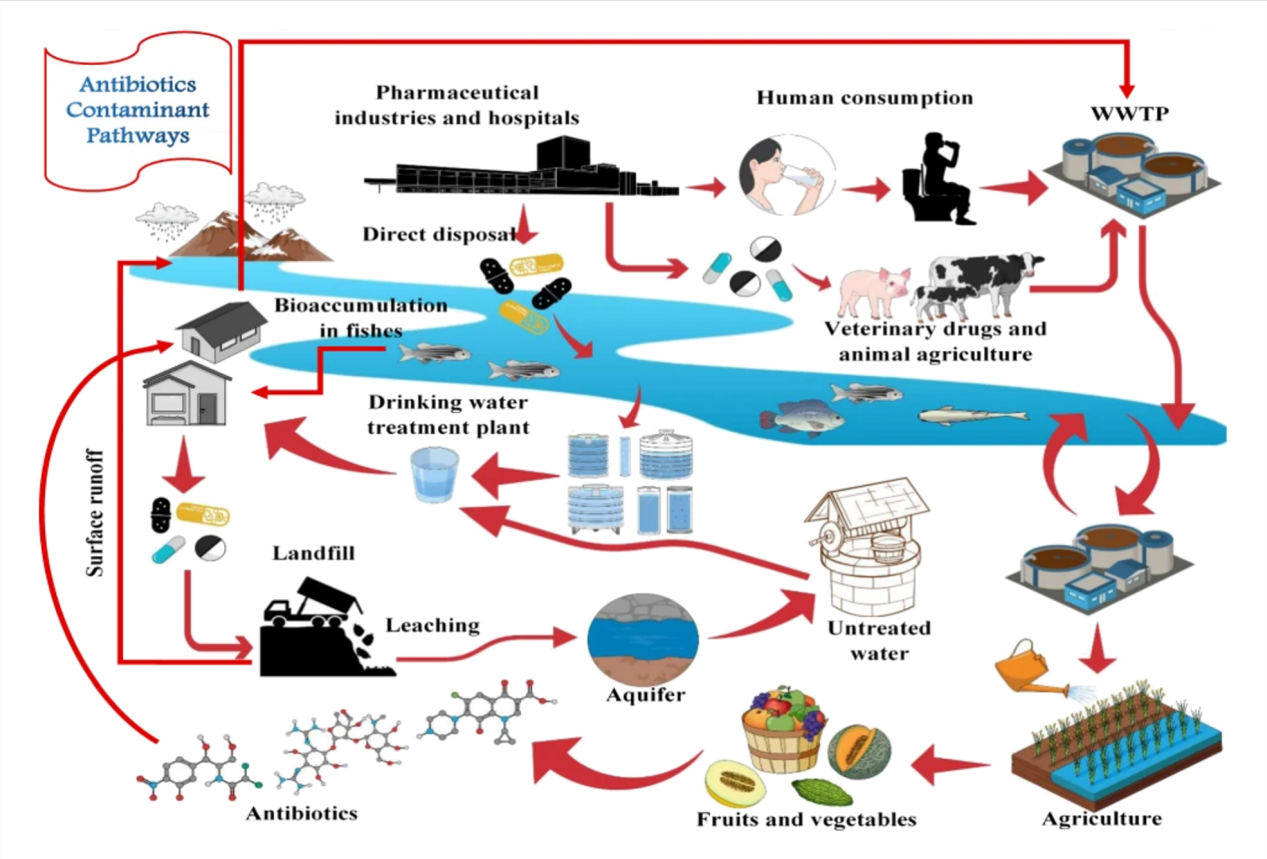


Figure 2: Sources of antibiotics in the environment and their pathways for impacts of antibiotic residues on the environment and human health. Reproduced from [46] (© 2020 C. Bhagat et al., published by Springer Nature, distributed under the terms of the Creative Commons Attribution 4.0 International License, https://creativecommons.org/licenses/by/4.0).

environment pose risks to both ecosystems and human health. Several primary barriers contribute to the difficulty in removing antibiotics effectively:

Chemical complexity

The diverse chemical structures of antibiotics present a significant challenge for their removal compared to simpler contaminants. Various classes of antibiotics necessitate specific treatment processes to achieve effective removal. Furthermore, the degradation of antibiotics can result in the formation of transformation products [47], which may possess distinct properties and introduce additional environmental and health risks.

Low quantities

Antibiotics are frequently present in the environment in small amounts, usually in the range of parts per billion (ppb) or parts per trillion (ppt) range. Detecting and eliminating them at such low concentrations poses a significant challenge [42]. Additionally, antibiotics may be co-present with a mixture of other pollutants in certain instances, complicating the isolation and targeted removal of antibiotics.

Multiple sources

Antibiotics can enter the environment through various pathways, including wastewater discharges from healthcare facilities, pharmaceutical industry effluents, agricultural runoff, and human and animal waste [48]. However, effectively locating and regulating each source poses a significant challenge.

Persistence nature

Certain antibiotics exhibit persistence and resist environmental degradation, resulting in prolonged contamination [49]. Additionally, they are classified as emerging contaminants because of ongoing research on their potential hazards and environmental impacts [50]. Consequently, standardized removal methods may not be readily available.

Cost and infrastructure

Implementing successful antibiotic removal technologies often requires substantial investments in advanced treatment infrastructure at high operational cost. While advanced treatment processes like advanced oxidation or membrane filtration may be effective, they are energy-intensive and expensive to implement on a large scale [28].

Limited public awareness

Many people may be unaware of how improper antibiotic disposal harms the environment or of the importance of antibiotic removal, which leads to poor practices and pollution. Additionally, in many areas, there may be a lack of regulatory regulations for safe antibiotic levels in water [51], making it challenging to establish treatment targets.

Principal mechanisms of photocatalytic processes for antibiotic degradation

Semiconductor-based photocatalysis effectively promotes the degradation of antibiotics from contaminated water. Researchers have conducted experiments to evaluate the efficacy of various photocatalysts in eliminating different antibiotics from their respective environments. Research on catalyst composition and application has evolved through four distinct generations [52], each shedding light on the mechanisms of various photocatalysts used for pollutant degradation, namely, single-component transition metal oxides (TMOs) representing the first generation, doped TMOs, binary TMOs, and doped binary TMOs as the second generation, and inactive/active support-immobilized TMOs as the third generation, while the fourth generation refers to ternary/quaternary compositions. The first two generations represent suspended catalysts, the third generation is supported catalysts, and the fourth generation can be suspended or supported. Generally, oxides of titanium, zinc, bismuth, and tungsten, as well as graphene, graphitic carbon nitride (g-C_3N_4), and their substitute materials are commonly synthesized and used as photocatalysts for the removal of antibiotics from contaminated sources. These materials are synthesized through a variety of advanced methods, including sol–gel, hydrothermal, solvothermal, precipitation and template-assisted techniques [53]. The synthesis method chosen often depends on factors such as the desired crystal structure, particle size, surface area, and photocatalytic activity required for the specific application.

General mechanisms of the photocatalysis process

Three fundamental steps can be identified in semiconductor photocatalysis for the breakdown of antibiotics in contaminated water, that is, photon absorption, excitation, and reaction [54,55]. When a photocatalyst absorbs photons with energy higher than its bandgap, electrons (e^-) in the valence band (VB) transition to the conduction band (CB), resulting in the formation of holes (h^+) in the VB (photocatalyst + hν → photocatalyst + h^+ + e^-) [54,55]. Afterwards, the electrons and holes are effectively separated and move toward the surface of the photocatalyst, initiating further reactions on the material surface. Photogenerated holes have the potential to directly target antibiotics (h^+ + antibiotics → H_2O + CO_2 + degradation products). This process can possibly result in substantial destruction of the harmful antibiotics. Figure 3 illustrates the different phases of the typical photocatalytic decomposition of antibiotics.

Materials scientists have suggested and acknowledged two distinct degradation pathways [56]. The first pathway occurs when the semiconductor's CB potential is more negative than the $O_2/O_2^{\bullet-}$ redox potential (−0.13 eV vs normal hydrogen electrode (NHE)). In this reductive pathway, the photoexcited electrons have the ability to interact with electron acceptors, like

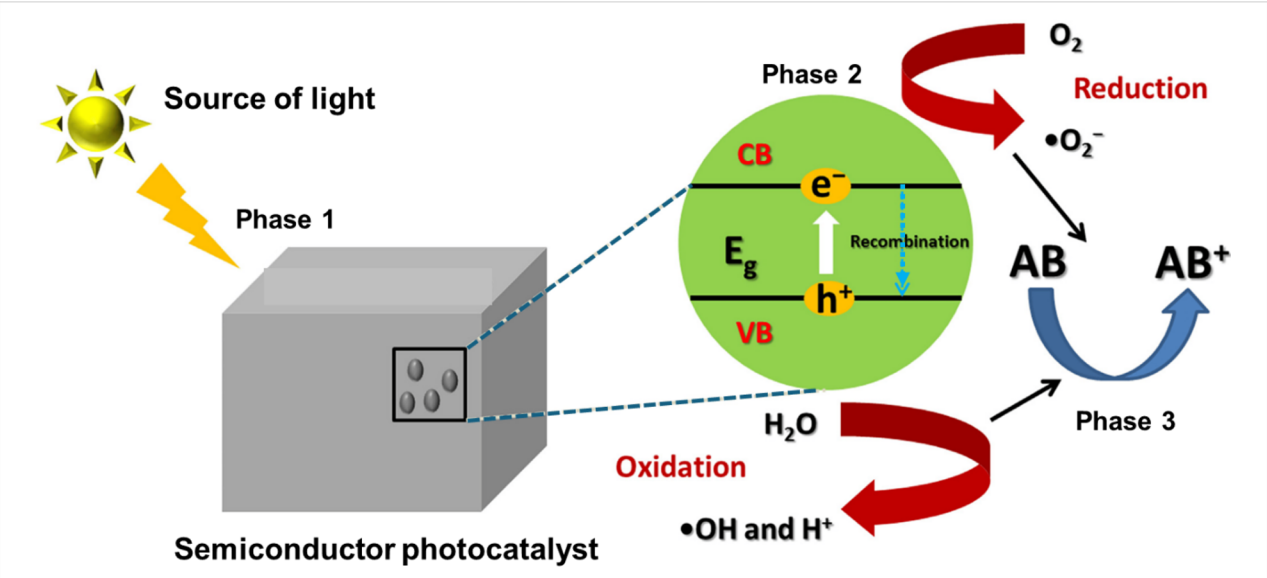


Figure 3: General mechanism for antibiotic degradation using semiconductor-based photocatalysis processes. Reproduced from [35] (© 2022 X. Bai et al., published by MDPI, distributed under the terms of the Creative Commons Attribution 4.0 International License, https://creativecommons.org/licenses/by/4.0).

O_2, which can be found on the catalyst surface or dissolved in water. This reaction reduces O_2, forming a superoxide radical anion ($O_2^{\bullet-}$) ($O_2 + e^- \rightarrow O_2^{\bullet-}$) [35,55]. Additionally, H_2O_2 can be generated by transferring electrons from the conduction band to the adsorbed O_2. Because the CB of the catalyst has a higher negative potential than the O_2/H_2O_2 system (+0.682 eV vs NHE), the generated H_2O_2 subsequently reacts with electrons generated by light to yield active $HO^\bullet$ radicals [35,57]. The second pathway also known as the oxidative pathway, occurs when the holes migrate to the surface of the photocatalyst. As a result, $HO^\bullet$ radicals are generated by oxidizing H_2O/OH^-, and this generation is influenced by the alkalinity or acidity of the surrounding environment ($H_2O/OH^- + h^+ \rightarrow HO^\bullet + H^+$) [35,57]. After excitation, H^+ possesses the capacity to interact with electrons, generating thermal energy ($H^+ + e^- \rightarrow$ energy). This process results in a reduction of the photodegradation efficiency. Notably, the typical redox potential of photocatalysts must exceed that of $HO^\bullet/OH^-$ (+1.99 eV vs RHE) [35,57]. Both ROS ($HO^\bullet$ and $O_2^{\bullet-}$) are highly reactive oxidizing agents in photocatalysis. Under extended exposure to high-energy light, they have the ability to efficiently convert antibiotics and their intermediates into the final mineralization products, such as CO_2 and H_2O (antibiotics + $HO^\bullet$ and/or $O_2^{\bullet-} \rightarrow CO_2 + H_2O$).

Mechanisms of metal, nonmetal, or co-doped photocatalysts

The large bandgap and high electron–hole recombination rate of traditional and single semiconductor photocatalysts limit their effectiveness under visible light, which hinders their practical application. To improve the photocatalytic efficiency, several dopants, such as transition metals (Fe, Cu, Mn, Zn, Ni, Co, Cr, Ru, and Ag) or nonmetals (C, N, S, and F) have been introduced into the semiconductor material. Metal and nonmetal dopants have the ability to construct an impurity energy level located below the CB of the material [58,59]. This action serves to reduce the bandgap, which in turn extends the absorption wavelength edge towards the region of visible light [60,61]. The idea of modifying semiconductor materials in the second generation involves the process of co-doping with both metal and nonmetal atoms. This method has attracted considerable interest because of its synergistic effect on improving the absorption of visible light and minimizing electron–hole recombination [62-64]. However, these synthesized materials not only remove antibiotic pollutants but also impact the formation of ROS. The co-doped material provide more holes and electrons for the generation of ROS than other monodoped materials. Shen and their group made a comparable observation regarding a Co–N co-doped TiO_2 photocatalyst, demonstrating that the co-doped TiO_2 photocatalyst played a significant role in the generation of holes and electrons. Specifically, it contributed 70.1% of the holes and 29.9% of the electrons, in comparison to Co-doped TiO_2 and N-doped TiO_2 [60]. This can be attributed to the electron-trapping capabilities of Co ions, which enhance charge transfer and facilitate highly efficient electron–hole separation. The detailed mechanism of dopant ions in semiconductor materials is shown in Figure 4.

Mechanisms of heterojunction photocatalysts

Most semiconductor materials are susceptible to electron–hole recombination, which reduces photocatalytic efficacy. As a result, additional efforts must be taken to ensure that visible light is used efficiently while electron–hole recombination is avoided. To improve semiconductor material performance, charge carriers should be separated better, their lifespan extended, the photocatalyst's bandgap reduced, and the surface area increased [52]. Researchers have taken two approaches to developing effective solar light-activated semiconductor-based photocatalysts. The main approach is to improve the absorption of visible light of semiconductor materials by including metal or nonmetal elements. This augmentation can modify the energy band structure or enable localized surface plasmonic resonance (LSPR). The second strategy focuses on the development of heterojunctions between two semiconductors that is activated by visible light [65,66]. These heterojunctions should have bandgaps and energy levels that match the valence and conduction bands. Heterojunctions can be classified in type-I heterojunctions (Figure 5a), type-II heterojunctions (Figure 5b), p–n junctions (Figure 5c), Schottky junctions (Figure 5d), and Z-scheme heterojunctions (Figure 5e,f), which have all been extensively studied regarding antibiotic photodegradation [67,68]. When a potential difference is applied in heterojunction systems, electrons transfer from the conduction band (CB) of semiconductor 1 (SC1) to the CB of semiconductor 2 (SC2). At the same time, holes in the valence band (VB) of SC1 migrate to the VB of SC2. This charge transfer occurs in type-I heterojunctions, as shown in Figure 5a.

In type-II heterojunctions, however, holes move from SC2 to SC 1 (Figure 5b). In the p–n junction system, a type-II mechanism exchanges electrons and holes. Electrons travel from p-type to n-type semiconductors, whereas holes move from n-type to p-type semiconductors (Figure 5c). The effective segregation of light-induced charge carriers allows the CB of the second semiconductor and the VB of the first semiconductor to engage in reduction and oxidation processes, thus enhancing the photocatalytic activity. Although type-II heterojunctions can restrict photogenerated charge recombination, they also reduce compound semiconductors' redox capacity and pose problems to the continuous flow of electrons and holes because of electrostatic repulsion. A Schottky junction is also formed by combining two different semiconductor materials

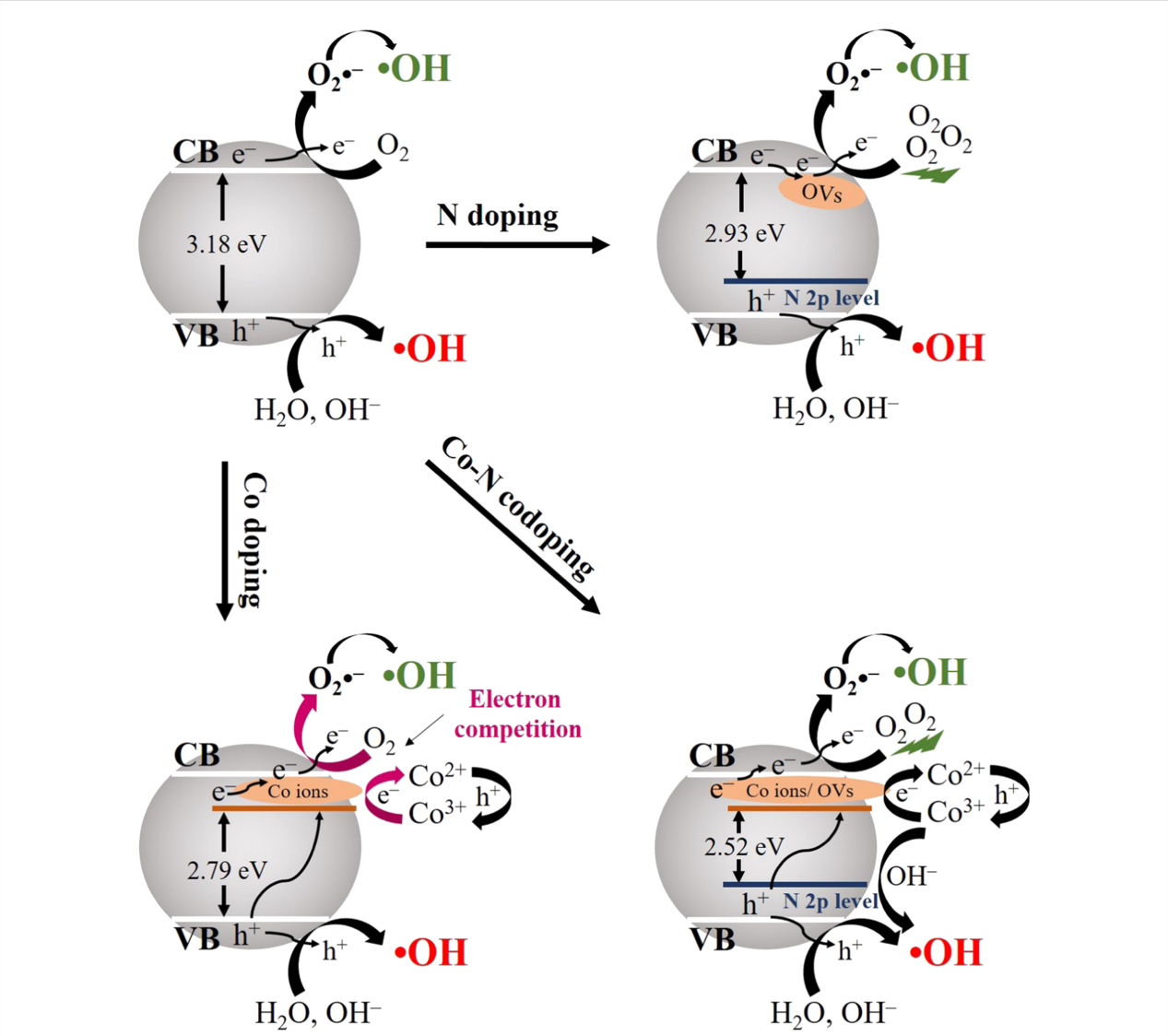


Figure 4: The mechanism of doped ions in semiconductor materials. Figure 4 was reprinted from [60], Journal of Alloys and Compounds, vol. 862, by J.-H. Shen, Y.-H. Tang, Z.-W. Jiang, D.-Q. Liao, J.-J. Horng, "Optimized preparation and characterization of Co-N codoped TiO_2 with enhanced visible light activity: An insight into effect of dopants on surface redox reactions of photogenerated charge carriers for hydroxyl radical formation", article no. 158697, Copyright (2021), with permission from Elsevier. This content is not subject to CC BY 4.0.

(Figure 5d). The oxidation capability of Schottky heterojunctions is restricted to some organic impurities because of the location of the semiconductor photocatalyst's VB. To overcome the aforementioned concerns with other heterojunctions, the concept of Z-scheme heterojunctions was developed, inspired by natural photosynthesis [69-71]. These heterojunctions are classified based on their charge transfer mechanism and the presence or absence of mediators. The direct Z-scheme relies on the direct electron transfer between photocatalysts; eliminating the electron mediator simplifies the design and enhances stability but may suffer from higher charge recombination. In contrast, an indirect Z-scheme, which uses a redox pair (e.g., Fe^{3+}/Fe^{2+}) or a conductive mediator to facilitate efficient charge transfer and spatial separation of charge carriers, reduces the risk of recombination and increases the photocatalytic efficiency. While indirect composites are more complicated to fabricate and possibly beset by stability problems due to mediator degradation, indirect Z-schemes are nevertheless often used in applications that demand high charge separation performance. In contrast, direct Z-schemes are best suited for systems where robustness and simplicity are desired. When exposed to visible light, electrons at a lower CB location on SC2 interact with holes on the VB of SC1 via the heterojunction interface (Figure 5e) or an intermediary conducting medium (Figure 5f). This enables the photocatalyst to maintain high redox capacity.

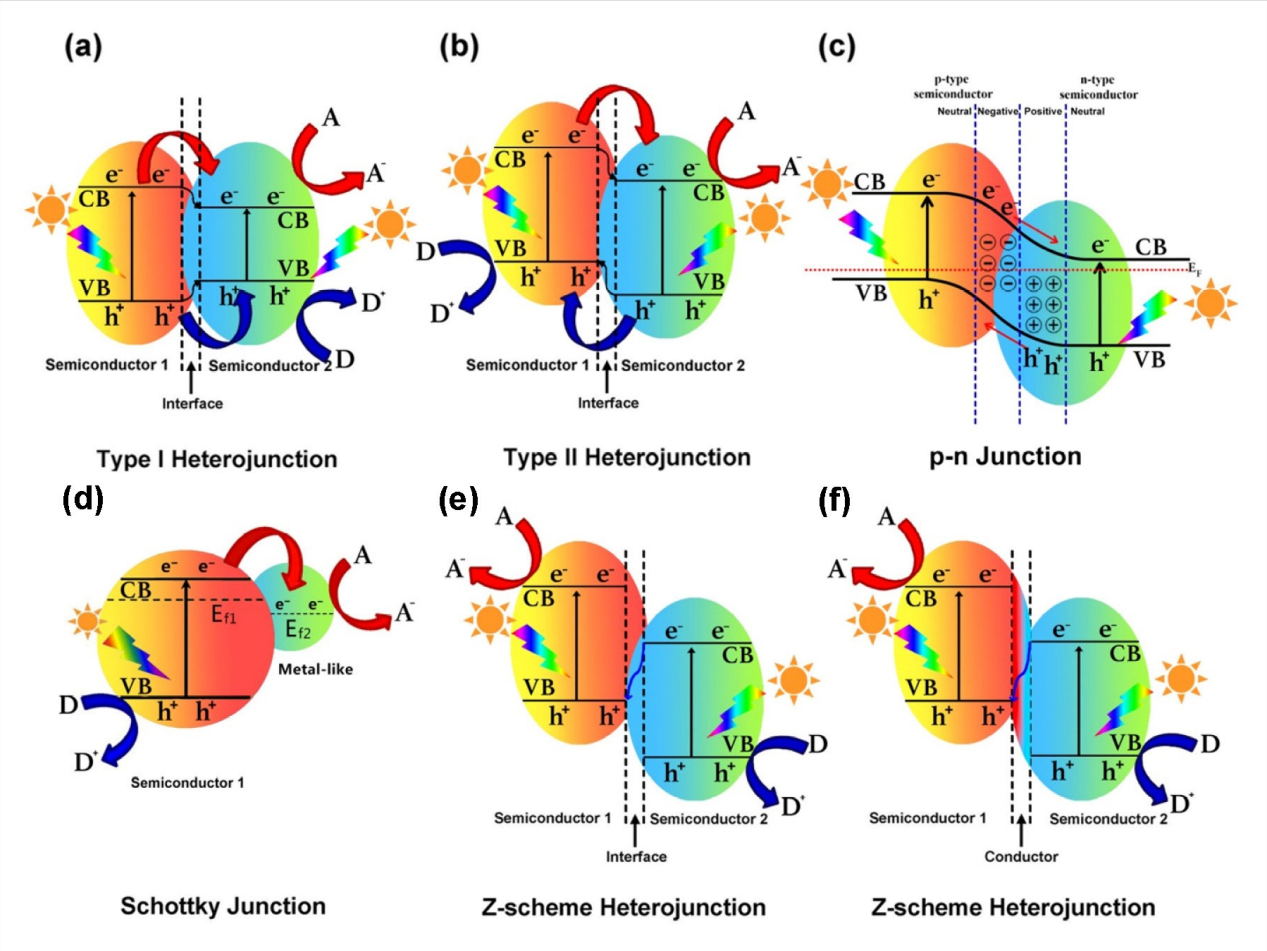


Figure 5: Six structural heterojunction models: (a) type-I heterojunction, (b) type-II heterojunction, (c) p–n junction, (d) Schottky junction, (e) Z-scheme heterojunction (without an electron mediator), and (f) indirect Z-scheme (with an electron mediator). Figure 5 was reprinted from [67], Chinese Journal of Catalysis, vol. 40, by Y. Ren, D. Zeng, W.-J. Ong, "Interfacial engineering of graphitic carbon nitride (g-C_3N_4)-based metal sulfide heterojunction photocatalysts for energy conversion: A review", Pages 289–319, Copyright (2019), with permission from Elsevier. This content is not subject to CC BY 4.0.

Efficiency of antibiotic removal by semiconductor-based photocatalysts

Photocatalysis is a highly effective, affordable, and environmentally friendly approach for removing antibiotics from wastewater. Various semiconductor photocatalysts, such as TiO_2, ZnO, bismuth oxyhalide (BiOX), g-C_3N_4, graphene oxide (GO), WO_3, and their derivatives, have distinct physical and chemical characteristics that influence their efficiency and efficacy in removing antibiotics. The subsequent sections describe these six commonly used semiconductor materials to remove antibiotics from the environment and their impact on sustainable wastewater treatment.

Titanium dioxide-based materials

TiO_2 is the most commonly used photocatalyst for antibiotic removal owing to its unique features. In nanostructured forms, this substance exhibits outstanding physical and chemical durability, a high ratio of surface area to volume, adjustable electronic properties, exceptional photocatalytic performance, lack of toxicity, widespread availability, and cost efficiency [65]. It has a broad bandgap (3.2 eV). Therefore, it can be activated only by UV radiation, which is only a small part of the solar spectrum. This feature makes TiO_2 not suitable for outdoor applications where natural light is abundant. Although TiO_2 has a high photocatalytic activity under UV light, its practical use is limited because of rapid electron–hole recombination and insufficient visible light absorption [65]. Hence, it is critical to develop effective strategies to enhance TiO_2 activity under visible light. When using TiO_2 in a full-scale field deployment, reducing the amount and utilizing solar energy can be extremely cost-effective and beneficial to wastewater treatment. Researchers have improved the photocatalytic activity of bulk TiO_2 through various modifications, including doping with a suitable transition metal and synthesizing composite materials. Several advanced photocatalysts have been developed and successfully used to prevent antibiotics contamination, a list of which is

shown below in Table 1. These modifications have led to improved charge separation rates, reduced recombination rates, and the generated oxygen vacancies, ultimately enhancing catalytic efficiency in visible light or solar-simulated light. The durability of the modified TiO_2 relied on the number of electrons in the dopants and their ionic size.

Although researchers have significantly improved the catalytic efficacy of TiO_2 under visible or solar-simulated light, retrieving the synthesized small particles poses new challenges. Researchers have recently synthesized heterojunctions using TiO_2 and magnetic particles such as α-Fe_2O_3 and Fe_3O_4 in order to solve the problem of recovering particles. They accomplished the separation with success, greatly enhancing the efficiency of the catalysts and their potential to be reused, while also decreasing the overall cost of synthesis. The construction of the α-Fe_2O_3@TiO_2 photocatalyst resulted in a higher efficiency in removing the antibiotic cefixime (CFX) than that of pure TiO_2 and Fe_2O_3 under visible light illumination (500 W halogen lamp and wavelengths above 400 nm) [72]. At a dosage of 0.012 g/L of α-Fe_2O_3@TiO_2 and pH 4.76, 98.8% of an initial CFX concentration of 20.5 mg/L was effectively removed after 103 min. The heterojunction formed between TiO_2 and Fe_2O_3 promoted the electron–holes segregation rate and reduced the rate of recombination. A TiO_2/GO/chitosan photocatalyst was synthesized by Erim et al. [73] for the degradation of CFX under UV-A irradiation. Under optimized conditions (catalyst dose of 0.327 g/L, CFX concentration of 20.29 mg/L, pH 4.1, and UV-A irradiation of 60 W), the TiO_2/GO/chitosan photocatalyst exhibited a prominent degradation efficiency of 95.34%. They also reported in another article that the SWCNT/ZnO/Fe_3O_4 combination exhibited a CFX decomposition efficiency of 94.19% at pH 5.93, 22.76 ppm CFX, and 0.46 g/L photocatalyst [74]. In a recent study, Jeyaprakash and coworkers [75] synthesized Ti^{3+}-doped TiO_2 with oxygen vacancies utilizing ultrasonic treatment for the degradation of tetracycline (TC) via sono-photocatalysis under visible halogen lamp irradiation. The modified TiO_2 demonstrated remarkable degradation of TC, with an efficiency of approximately 96%, which is 1.56 times higher than that of pure TiO_2 photocatalysts.

Zinc oxide-based materials

Zinc oxide (ZnO) is another widely used semiconductor material that exhibits enhanced sensitivity to ultraviolet (UV) light. It possesses a substantial surface area, exhibits good thermal stability, is non-toxic, and can be easily morphologically modified (such as nanorods, nanosheets, and nanobelts). Because of its higher quantum efficiency, it is anticipated to demonstrate superior photocatalytic activity in comparison with TiO_2, g-C_3N_4, and BiOBr [66]. However, its broader bandgap (3.37 eV) and rapid electron–hole recombination limit its ability to undergo photocatalytic reactions when exposed to visible light [66]. To address these limitations, significant endeavors have been undertaken to improve the properties of ZnO by introducing dopants (nonmetals and/or transition metals compounds) into ZnO. This alteration introduces surface defects, leading to a decrease in the bandgap. As a result, the materials become more efficient in harvesting energy to produce reactive species, which is beneficial for applications involving contaminant treatment [61]. Hunge and coworkers [76] synthesized MoS_2/ZnO (MZ) composites with a smaller bandgap (2.81 eV), which showed higher ciprofloxacin (CIP) removal efficiency than their single constituents (ZnO = 43% and MoS_2 = 50%). A similar approach was also observed for the removal of erythromycin (ERY), spiramycin (SP), and CIP by using $ZnIn_2S_4$ [77], g-C_3N_4/$ZnFe_2O_4$ [78], Cr_2O_3@ZnO [79], and ZnO/TiO_2 [80]. However, the application of doped ZnO for remediation purposes is presently impractical because of electron–hole recombination under certain conditions.

Scientists have found a variety of adsorbent materials, including biochar, metal-organic frameworks (MOFs), functionalized mesoporous silica, porous organic polymers, zeolite, and derivatives of graphene. These substances act as a support for metal oxides and immobilize the catalyst, increase the catalyst surface area, and improve the chemical stability. Consequently, there is an enhancement in catalytic performance. In a study conducted by Rahman and colleagues [61], it was found that pure ZnO has a very low efficiency (7%) in degrading the antibiotic metronidazole (MNZ) through photocatalysis under 180 min of irradiation with visible light (wavelength, $\lambda \geq 400$ nm and intensity ca. 3×10^4 lux). However, the efficiency increases to 31.8% when using N-doped ZnO photocatalyst. After 70 min of light exposure, a ternary GO-N-ZnO photocatalyst showed a considerable increase in photocatalytic efficiency of 43.45%. Yu and coworkers [81] synthesized ZnO with N,O-containing biochar (ZnO/NOC), which showed a TC removal efficiency of 97.08%. The photocatalytic activities of ZnO/NOC were 5.4 and 7.7 times higher than that of pure ZnO for TC (30 mg/L) under ultraviolet and visible light, respectively. The excellent performance was ascribed to large surface area, proper pore sizes, fast charge transfer, high density and long lifetime of photoinduced charges, and strong interaction between ZnO and N,O-containing biochar [81]. Roy and colleagues [82] effectively synthesized a rGO-ZnO composite functionalized with ferrocene through a simple hydrothermal method. This Fc@rGO-ZnO photocatalyst exhibited exceptional performance compared to pristine ZnO, resulting in a five-fold increase in CIP and SMX removal efficiency. After three hours of treatment, it removed more than 95% of the anti-

biotics. The most recent research on the use of ZnO- or Zn-based compounds as photocatalysts to remove antibiotics from water is compiled below in Table 2.

Bismuth-based materials

Although the activity of titanium dioxide- and zinc oxide-based photocatalysts has been increased through modification, they still absorb visible light poorly. Bi-based photocatalysts have been widely employed to degrade antibiotics under the illumination of UV and visible light [83,84]. They also possess a distinctive electronic structure with the VB containing Bi 6s and O 2p orbitals [54]. This distinctive configuration results in a more pronounced absorption edge in the visible light spectrum. The inclusion of bismuth in photocatalytic research is justified because of its limited solubility in water, which contributes to the compounds' ecological safety. Nevertheless, Bi-based photocatalysts have certain limitations, including reduced surface area, diminished absorption efficiency, poor heterojunction interface matching, and limited carrier transfer routes [85]. Bi-based materials for the degradation of antibiotics include various compounds such as Sillén-type BiOX, scheelite structures ($BiVO_4$, $BiOIO_3$, Bi_2O_3, and Bi_2S_3), Aurivillius-type Bi_2MO_6 (M = Mo, Cr, and W), and other composites synthesized with metals and nonmetals or heterojunctions. Table 3 below provides comprehensive details and a concise overview of the latest research on bismuth-based photocatalysts used to eliminate antibiotics from wastewater.

Bi_2O_3 is a widely utilized semiconductor in the fields of electronics and chemical engineering because of its uncomplicated composition, affordable price, and easy manufacturing process. Bi_2O_3 is widely recognised as a polycrystalline photocatalyst that exhibits four main phases. The majority of these phases are determined to be unstable, with α-Bi_2O_3 appearing at low temperatures and δ-Bi_2O_3 appearing at high temperatures. Scientists have noted that Bi_2O_3 in the metastable phase can undergo a transformation into $(BiO)_2CO_3$, which limits its potential as an effective visible photocatalyst because of its chemical instability [85]. Furthermore, β-Bi_2O_3 exhibits enhanced photocatalytic efficiency in comparison to α-Bi_2O_3. Nevertheless, the inherent instability of β-Bi_2O_3 presents a formidable obstacle in the development of uncomplicated techniques for producing pure β-Bi_2O_3, particularly at the nanoscale. The photocatalytic efficiency of Bi_2O_3 is inadequate for decomposing antibiotics without modification with suitable dopants. Chen and his colleagues [86] synthesized nanoscale Bi_2O_3 and observed little degradation of TC. Modification of Bi_2O_3 with MnO_2, changed the morphology from nanorods to nanosheets. This nanosheet structure showed a higher TC removal efficiency than pure Bi_2O_3, attributed to the increased specific surface area and absorption capacity. Using a one-step hydrothermal process, Wu et al. [69] synthesized Bi-bridged Z-scheme BiOCl/Bi_2O_3 heterojunctions. The constructed binary photocatalysts exhibited 94.79% TC degradation efficiency owing to the enhanced separation of electron–hole pairs and powerful redox capability. Higher photoactivity was also observed for other heterostructures such as $NiFe_2O_4$/Bi_2O_3 [87], Fe_3O_4@Bi_2O_3–RGO [88], Bi_2O_3/$(BiO)_2CO_3$ [89].

Bismuth oxyhalides (BiOX) are renowned as photocatalysts because of their distinctive optical and electrical properties, distinguishing them from other promising materials. The distinctive layered structure of BiOX (X = Cl, Br, and I) facilitates efficient separation of charge carriers, resulting in exceptional photocatalytic performance [85]. BiOX includes $[Bi_2O_2]^{2+}$ slabs surrounded by double slabs of $[X]^-$. The bandgaps of the different compounds are as follows: 3.22 eV (BiOF), 2.80 eV (BiOCl), 2.36 eV (BiOBr), and 1.75 eV (BiOI) [85]. Although BiOCl has a larger bandgap, it is considered a more promising photocatalyst than BiOI and BiOBr [90]. For example, BiOCl microspheres were able to remove 91.90% of TC after 30 min treatment at a dosage of 500 mg/L of catalyst, at pH 4.8 and an initial TC concentration of 20 mg/L [91]. The degrading effectiveness of the photocatalysts reduced as the amount of sorbitol was increased. The improved photodegradation was possible because the catalyst prevented the recombination of electrons and holes and facilitated the direct attack of h^+ on the surface of BiOCl [84,91]. This was verified by monitoring the lower effectiveness of BiOI [92] and BiOBr [93] in removing antibiotics. The photocatalytic activity of BiOX varies based on the dipole moment; the efficiency is particularly high when the dipole moment exceeds 2.0 D. The hybridization of halogens does not impact electron mobility. However, it does lead to a decrease in hole mobility while possibly enhancing the separation of charge carriers [94]. In order to enhance the photocatalytic activity of BiOX, significant endeavors have been undertaken, including the creation of heterojunctions or the introduction of metal doping. Wang et al. [84] synthesized BiOCl/Mt photocatalysts in which montmorillonite (Mt), which is naturally rich in iron, was combined with bismuth nitrate. According to the authors, the composite exhibited 3.4 times higher reactivity than BiOCl when exposed to visible light. The degradation of TC using the BiOCl/CdS catalyst exhibited a similar tendency, with degradation rates 4.73 and 2.94 times higher than those of pure CdS and BOCl, respectively [95]. Some other heterostructures also exhibited significant photocatalytic activity in the degradation of antibiotics; they are given below in Table 3.

Bismuth metal oxides such as Bi_2WO_6, Bi_2MO_6, $BiVO_4$, and $Bi_2Ti_2O_7$ are also gaining attention for their possible use in antibiotic degradation. The hybrid oxides mostly comprise

Bi_2O_3 and various metal oxides such as V_2O_5, W_2O_3, Mo_2O_3, and TiO_2. $BiVO_4$ is a newly designed n-type semiconductor with enhanced photocatalytic efficiency. This is attributed to its specific physicochemical features, including ferro-elasticity and ionic conductivity [90]. Regrettably, bismuth-based metal oxides exhibit a low light conversion efficiency as a result of the swift recombination of electrons and holes. However, several composite photocatalysts have been studied for the degradation of antibiotics, including $BiVO_4/MoS_2$, $BiVO_4/FeVO_4$, $AgI/BiVO_4$, $g\text{-}C_3N_4/BiVO_4/rGO$, $Ag/AgBr/BiVO_4$, $CuS/BiVO_4$, $BiVO_4/TiO_2/rGO$, $MnFe_2O_4/BiVO_4$, $BiVO_4/GO/CoFe_2O$, $ZnFe_2O_4/BiVO_4/g\text{-}C_3N_4$ and $BiVO_4$@BiOCl (see below in Table 3). A novel heterostructure of $BiVO_4$ nanosheets and MoS_2 nanoflakes yielded 97.46% degradation of TC within 90 min of visible light illumination with 40 mg/L initial concentration of TC and 15 mg/L catalyst loading [96]. Surprisingly, the photocatalytic TC degradation performance decreased to 66.82% when the catalyst loading was increased to 20 mg/L. The stability of the nanocomposite photocatalyst remained at 94.45% after 4th cycle of reuse. Trapping analysis showed that scavengers reduced the photodegradation rates.

Bismuth tungstate (Bi_2WO_6) is also an n-type semiconductor that belongs to the Aurivillius phases. The material exhibits two distinct crystallographic phases, namely monoclinic and orthorhombic. Orthorhombic Bi_2WO_6 has alternating layers of $(Bi_2O_2)^{2+}$ and WO_6 octahedrons. It comprises perovskite layers and has a bandgap of 2.77 eV. The research community has shown significant interest in zero-dimensional Bi_2WO_6 quantum dots and one-dimensional Bi_2WO_6 nanofibers. Bismuth tungstate exhibits excellent thermal and chemical stability in addition to its activity in visible light. It is typically synthesized through mixing $Bi(NO_3)_3$ and Na_2WO_4 using different methods. The distinctive layered structure of this material creates gaps between the slabs that form an electric field. This electric field opposes the movement of electrons and holes. This effect decreases the recombination of charge carriers, leading to an increase in photocatalytic activity. In a recent study, Wang et al. [97] found that small amounts of added Ti greatly enhanced the chloramphenicol (CAP) degradation capabilities of Bi_2WO_6, resulting in an impressive degradation rate of 92.44%. It has been observed that the incorporation of Mg, Fe, Zn, Cu or other transition metals through doping can potentially improve Bi_2WO_6 light absorption capabilities and increase the antibiotic degradation efficiency [98]. Some metal-doped bismuth photocatalysts and their antibiotic degradation efficiency are summarized below in Table 3.

Graphitic carbon nitride-based materials

Graphitic carbon nitride ($g\text{-}C_3N_4$) is a metal-free semiconductor material with distinct optical, electrical, structural, and physicochemical characteristics [99]. These properties make it well-suited for applications in energy and environmental fields. Because of its narrow bandgap of 2.7 eV, this material can efficiently absorb a significant amount of visible light, which is advantageous for both oxidation and reduction reactions [100]. Nevertheless, some noteworthy concerns arise, such as elevated rate of electron–hole recombination, limited surface area, restricted number of active sites, slow kinetics of surface reactions, and the reduced mobility of charges, resulting in electron delocalization [99,100]. The molecular rearrangement of $g\text{-}C_3N_4$ has been the subject of recent research because of its potential to alter the surface chemistry and textural structure [101]. This technique reduces carrier transfer resistance, improves pollutant adsorption, broadens the light absorption range, and promotes carrier separation. During the degradation of tetracycline hydrochloride (TCH), $g\text{-}C_3N_4$ exhibited remarkable activity under visible light and degraded 84.1% of TCH, while bulk $g\text{-}C_3N_4$ achieved only 52.1% after 90 min of irradiation.

Recently, researchers have revealed that adding small organic compounds into the precursors of $g\text{-}C_3N_4$ through copolymerization can significantly improve the efficiency of $g\text{-}C_3N_4$. Li et al. [102] carried out the copolymerization of thiourea with 7,7,8,8-tetracyanoquinodimethane (TCNQ) to enhance the energy band and electronic structure of $g\text{-}C_3N_4$. The pefloxacin degradation efficiency of the $g\text{-}C_3N_4$/TCNQ catalytic system was four times higher than that of pristine $g\text{-}C_3N_4$. By combining thiourea with 3-aminopyridine, researchers modified the morphology and textural structure of $g\text{-}C_3N_4$, which improved its solar absorption and charge-carrier transportation. The photocatalytic TC decomposition rate was 3.32 times higher in pyridazine-doped $g\text{-}C_3N_4$ than in the unmodified form [103].

Several studies have shown that heterojunctions formed by combining $g\text{-}C_3N_4$ with other semiconductors with comparable band structures can take advantage of the differences in energy band structures while simultaneously combining the best features of both components. The result is an intrinsic electric field between the materials, which slows down the recombination of photogenerated electrons and holes and speeds up the transfer of photogenerated carriers [104]. By combining ZnO and $g\text{-}C_3N_4$, Wang et al. [105] synthesized a Z-type heterostructure. The newly synthesized composite had greater interlayer spacing, specific surface area, and pore volume. After 120 min of simulated light exposure, the rates of TC degradation by pure ZnO, $g\text{-}C_3N_4$, and defective ZnO/$g\text{-}C_3N_4$ composite were found to be 35.20%, 71.48%, and 93.47%, respectively. Because of the existence of N defects, the constructed nanocomposite promotes the electron transfer efficiently with lower recombina-

tion rates. Other g-C_3N_4 heterojunction photocatalysts, such as CdS/g-C_3N_4 [106], CoO/g-C_3N_4 [107], and P-doped g-C_3N_4/Co_3O_4 [58], have also shown improved photocatalytic activity (see below in Table 4). The binary composite still has several shortcomings. Compared to the binary composite, adding a third semiconductor can improve the separation of charge carriers and expand the range of wavelengths that can be absorbed because of synergistic effects. As an example, Kumar and colleagues synthesized a ternary S-scheme K,P-codoped g-C_3N_4/GO/$CoFe_2O_4$ (KPCN/GO/$CoFe_2O_4$) photocatalyst, which demonstrated a greater TC removal efficiency compared to the single constituents and binary heterostructures [64]. The photodegradation efficiencies of TC for KPCN/GO/$CoFe_2O_4$, KPCN/GO, KPCN, and g-C_3N_4 were reported to be 85%, 57%, 42%, and 30% after 60 min of visible light exposure, respectively. Likewise, Liu et al. [108] designed a ternary g-C_3N_4/Ag_2CO_3/GO photocatalyst, which follows a double Z-scheme, to degrade TC. The ternary system exhibits potent oxidation and reduction capabilities for antibiotic degradation (81.6% within 60 min) compared to the binary g-C_3N_4/Ag_2CO_3 composite (67.5% within 60 min). Indirect Z-scheme photocatalytic systems differ from direct Z-scheme systems by incorporating an electron mediator between the two semiconductors. This mediator facilitates the transport and separation of electrons and holes. However, the inclusion of an ionic electron transport medium in the traditional Z-scheme photocatalytic system leads to the occurrence of reverse reactions on the surface of photocatalysts, resulting in a decrease in the total number of photogenerated charges. Samsudin and colleagues [109] validated their findings by designing a Z-scheme Ag/$AgVO_3$/g-C_3N_4 photocatalyst. This catalyst exhibited outstanding capabilities in degrading CIP (82.6% within 2 h) and generating hydrogen from rainwater. The effective separation and mobility of photogenerated charge carriers were credited to the role of Ag nanoparticles as electron mediators. There are some other observations, which are shown below in Table 4.

Graphene oxide-based materials

Graphene is a monolayer of carbon atoms organized in a hexagonal lattice, with various types of defects present around the edges. This material is categorized based on the level of surface oxidation, which includes pristine graphene, graphene oxide, and reduced graphene oxide (rGO). Among the derivatives of graphene, GO and rGO are frequently used to support photoactive materials and immobilize pollutants. Additionally, they serve as crucial interfaces for electron carriers, augmenting light absorption and antibiotic adsorption through their functional groups [110]. Graphene derivatives possess two notable drawbacks. They are more expensive than other carbon compounds, and their normal synthesis procedure requires using dangerous oxidizing and reducing agents [110]. Therefore, it is crucial to utilize direct, secure, economical, and eco-friendly synthesis methods to use these materials as photocatalysts.

GO has attracted interest as another metal-free carbon material, owing to its two-dimensional ultrathin layered structure, robust stability, and remarkable capacity to transport charge carriers [110]. When coupled with suitable semiconductor materials or modified to other forms of heterostructures, it can enhance the photocatalytic efficiency for various applications, including water purification. GO-based photocatalysts can facilitate this process by generating electron–hole pairs upon absorption of photons. Recently, Kumar et al. [64] fabricated a K,P-co-doped g-C_3N_4/$CoFe_2O_4$ catalyst with GO, which demonstrated an 85% degradation rate for TC and a 99% degradation rate for DOX within 60 min of treatment time. The degradation efficiencies were improved through doping and further enhanced by adding GO and magnetic $CoFe_2O_4$. Numerous ternary compounds (see below in Table 5) that incorporate GO as a co-catalyst have been employed in the photocatalysis field to remove antibiotics. For instance, g-C_3N_4/Ag_2CO_3/GO [108], BiOBr/MoS_2/GO [111], and g-C_3N_4/GO/$CoFe_2O_4$ [64].

rGO is also considered as a promising semiconductor material, but its characteristics can differ based on the level of reduction and the specific production techniques employed. GO is a type of insulating material that is made from graphene by oxidizing graphite. The reduction process eliminates functional groups in GO that contain oxygen, restoring π-conjugated structures and electrical conductivity. rGO has a uniform tendency to attract molecules, but its ability to react to light is limited because of its wide bandgap and inefficient absorption of light. Therefore, suitable modifications to the base catalyst considerably improve the photocatalysis efficiency [82]. For instance, combining TiO_2 and rGO makes it more energy-efficient than traditional photocatalysts such as TiO_2. The enhanced activity of these heterojunctions was determined under simulated solar light; 87% of sulfamethoxazole (SMX) was removed within 1 h [112]. Adding Ag_3PO_4 to N-doped rGO yielded higher degradation rates of SMX [113]. Incorporating metal oxides into rGO enhances the photosensitization. The process of degrading different antibiotics in wastewater through photoactive oxidation has been investigated utilizing various graphene oxide-based materials such as rGO/WO_3, g-C_3N_4/$BiVO_4$/rGO, $BiVO_4$/TiO_2/rGO, rGO/$Bi_4O_5Br_2$, rGO-$BiVO_4$-ZnO, rGO-ZnO, ferrocene-rGO-ZnO, α-Fe_2O_3/ZnO/rGO, CdS-Bi_2MoO_6/rGO, and rGO-modified tin selenide (see below in Table 5).

Tungsten oxide-based materials or composites

Tungsten trioxide (WO_3) is considered environmentally benign, making it a preferable option for eco-friendly water treatment

applications. In aqueous solutions, WO_3 is mechanically strong and physiochemically stable, and the synthesis of high-purity WO_3 is a good option for the degradation of antibiotics under solar light irradiation [114]. WO_3 is a catalyst that responds to visible light and has consistent physicochemical properties because of its low bandgap energy (2.4 to 2.8 eV) [114]. However, the usage of this material in environmental remediation processes is questionable [115-117] because the electrons generated by light in the CB of WO_3 (about +0.5 V vs NHE) have a weaker positive potential compared to the reduction potential of O_2 ($O_2/O_2^{\bullet-}$ = −0.33 V vs NHE). Diverse approaches have been suggested to enhance its photocatalytic activity. For example, g-C_3N_4-WO_3 [115], rGO/WO_3 [116], and multi-wall carbon nanotubes-WO_3 [118] were found to photodegrade SMX under 300 W xenon arc solar simulator light. These three catalysts showed remarkable degradation of SMX, with degradation rates of 91.7%, 98.0%, and 88.5%, respectively. Various composites were synthesized using a simple anion-exchange approach, including AgI/WO_3 [119], Ag_3VO_4/WO_3 [117], and AgCl/Ag_3PO_4/g-C_3N_4 [120]. These composites were prepared by adding different molar ratios of AgX. With the inclusion of AgX, there was a significant enhancement in the removal rate of antibiotics. This was achieved by augmenting the positive potential and accelerating electron transfer rates. The most recent research on using tungsten oxide as photocatalyst to remove antibiotics from water is compiled below in Table 6.

Conclusion

This review comprehensively explores the latest advancements and challenges in using semiconductor-based photocatalysts to degrade antibiotic contaminants in the environment. It emphasizes the negative impact of antibiotic discharge on ecosystems and human health. The study investigates the mechanisms involved in photocatalytic degradation, which rely on generating free radicals and reactive oxygen species. Because the use of solar radiation and visible light sources for photocatalytic activation is currently limited, there is a distinct and urgent need for further exploration and development in this field. Therefore, focusing on long-term antibiotic removal rates and conducting comprehensive studies on intermediate compounds is essential.

The present review also extensively covers different strategies to improve the semiconductor photocatalytic activity, including modifying the morphology/structure, constructing heterojunctions, doping metals and nonmetals into the photocatalyst surface, and making surface/interface modifications. These strate-

Table 1: Degradation of antibiotics by titanium dioxide-based photocatalysts.[a]

Antibiotic	Dosages of antibiotics and catalysts	Light source and other parameters	Removal efficiency (%)	Reaction time (min)	Ref.
clarithromycin	0.1 mg/L of CLA, 100 mg/L of graphene-modified TiO_2	1000 W xenon lamp, simulated sunlight, pH 6, RWW	86.0	60	[112]
sulfamethoxazole	10 mg/L of SMX, 1250 mg/L of TiO_2/pBC	50 W xenon lamp, visible light, pH 4 to 10, SWW	91.27	180	[121]
sulfamethoxazole	10 mg/L of SMX, 1250 mg/L of Zn-TiO_2/pBC	50 W xenon lamp, visible light, pH 4, RWW	81.21	180	[122]
sulfamethoxazole	30 mg/L of SMX, 1000 mg/L of F-Pd co-doped-TiO_2	320 W xenon lamp, simulated sunlight, UPW	94.2	20	[123]
ciprofloxacin	0.5 mg/L of CIP, 0.43 g/L of black Ti^{3+}/N-TiO_2 (b-N-TiO_2)	5 W LED, visible light, pH 6.7, UPW	98.5	70	[124]
ciprofloxacin levofloxacin	75 uM of CIP/LEV, 1000 mg/L of N and C co-doped TiO_2	300 W xenon lamp, visible light, RWW	68.7 95.7	120	[63]
tetracycline chlortetracycline	10 mg/L of TC/CTC, 300 mg/L of TiO_2-MOF	300 W xenon lamp, visible light, pH 7, UPW	87.03 78.91	60	[125]
ceftriaxone	100 mg/L of CTR, 1 g/L of activated carbon based TiO_2	50 W LED, visible light, RWW	99.6	240	[126]
enrofloxacin	10 mg/L of ENF, 1 g/L of MX-TiO_2 composite	UVA lamp, 2.1 mW/cm^2, pH 4.8, UPW	91.6	300	[127]
cefixime	20.5 mg/L of CFX, 0.012 g/L of α-Fe_2O_3@TiO_2	500 W halogen lamp, visible light, pH 4.76, SWW	98.8	103	[72]
tetracycline	20 mg/L of TC, 0.01 g/L of Ti^{3+} doped-TiO_2	500 W halogen lamp, visible light, pH 4.7, SWW	96	60	[75]

[a]RWW: real wastewater, SWW: synthetic wastewater, and UPW: ultrapure water

Table 2: Degradation of antibiotics by zinc-based photocatalysts.[a]

Antibiotic	Dosages of antibiotics and catalysts	Light source and other parameters	Removal efficiency (%)	Reaction time (min)	Ref.
erythromycin	10 mg/L of ERY, 50 mg/L of $ZnIn_2S_4$	100 W iodine gallium lamp, visible light, UPW	100	180	[77]
spiramycin	20 mg/L of spiramycin, 1000 mg/L g-C_3N_4/$ZnFe_2O_4$	300 W xenon lamp, visible light, UPW	95.0	240	[78]
tetracycline	40 mg/L of TC, 1000 mg/L of Ag_3PO_4/Zn-Al LDH	500 W xenon lamp, simulated sunlight, UPW	96	90	[128]
ciprofloxacin	10 mg/L of CIP, 500 mg/L of $ZnSnO_3$	350 W xenon lamp, simulated sunlight, pH 5.9, SWW	85.9	100	[129]
ciprofloxacin	10 mg/L of CIP, 1 g/L of Cr_2O_3@ZnO	300 W xenon lamp, visible light, pH 3.5, UPW	100	30	[79]
tetracycline	30 mg/L of TC, 1 g/L ZnO and N,O-containing biochar (ZnO/NOC)	350 W xenon lamp, sunlight, pH 6, UPW	97.08	140	[81]
ciprofloxacin	0.05 mg/L of CIP, 2 g/L of MoS_2/ZnO composites	250 W metal halide lamp, ultraviolet light, UPW	96.18	120	[76]
tetracycline	40 mg/L of TC, 200 mg/L of ZnO/TiO_2 composites	300 W xenon lamp, simulated sunlight, UPW	84.06	120	[80]

[a]SWW: synthetic wastewater and UPW: ultrapure water

Table 3: Degradation of antibiotics by bismuth-based photocatalysts.[a]

Antibiotic	Dosages of antibiotics and catalysts	Light source and other parameters	Removal efficiency (%)	Reaction time (min)	Ref.
tetracycline	20 mg/L of TC, 1 g/L of BiOBr	10 W LED, visible light, pH 6.35, DW	80.3	90	[93]
ofloxacin	10 mg/L of OFX/CIP/NOR, 250 mg/L of BiOCl	125 W mercury lamp, UV light, pH 7, UPW	93.0	80	[83]
ciprofloxacin			74.0	240	
norfloxacin			92.0	240	
tetracycline	20 mg/L of TC, 10 mg/L of CIP/NOR, 500 mg/L of BiOCl	250 W xenon lamp, visible light, pH 7, UPW	91.90	30	[91]
ciprofloxacin			82.11	120	
norfloxacin			74.52	120	
ciprofloxacin	10 mg/L of CIP, 500 mg/L of BiOCl/NGQDs	300 W xenon lamp, visible light, pH 7, DW	94.0	10	[130]
ciprofloxacin	20 mg/L of CIP, 1000 mg/L of Ti_3C_2-Bi/BiOCl	300 W xenon lamp, UPW	89.0	100	[131]
tetracycline	10 mg/L of TC, 667 mg/L BiOCl/CdS	300 W xenon lamp, visible light, UPW	95.9	60	[95]
oxytetracycline	10 mg/L of OTC, 250 mg/L g-C_3N_4/BiOCl/CdS	natural sun light, pH 7, DW	99.0	240	[132]
tetracycline	10 mg/L of TC, 200 mg/L Z-scheme BiOCl/Bi–Bi_2O_3	300 W xenon lamp, visible light, UPW	94.79	150	[69]
tetracycline	20 mg/L of TC, 400 mg/L $BiOCl_{0.9}I_{0.1}$/β-Bi_2O_3	350 W xenon lamp, simulated sunlight, pH 6, UPW	82.4	120	[133]
tetracycline	45 mg/L of TC, 200 mg/L MnO_2/Bi_2O_3, 300 mg/L of peroxymonosulfate (PMS)	300 W xenon lamp, visible light, pH 6.5, UPW	73.34	100	[86]
tetracycline	10 mg/L of TC/CTC/OTC/DOX, 1000 mg/L of $BiVO_4$/TiO_2/RGO	1000 W xenon lamp, visible light, UPW	96.2	120	[134]
chlortetracycline			97.5		
oxytetracycline			98.7		
doxycycline			99.6		
tetracycline	190 mg/L of TC, 500 mg/L of $BiVO_4$/MoO_3	300 W xenon lamp, solar light, pH 4.52, UPW	97.66	160	[135]

Table 3: Degradation of antibiotics by bismuth-based photocatalysts.[a] (continued)

tetracycline	10 mg/L of TC, 250 mg/L of $MnFe_2O_4/BiVO_4$	300 W xenon lamp, visible light, UPW	92.0	120	[136]
tetracycline	40 mg/L of TC, 1.5 g/L of $BiVO_4/MoS_2$	100 W xenon lamp, visible light, UPW	97.46	90	[96]
lomefloxacin	25 mg/L of LOM, 500 mg/L of $ZnFe_2O_4/BiVO_4/g\text{-}C_3N_4$	300 W xenon lamp, visible light, UPW	96.1	105	[137]
tetracycline ciprofloxacin	40 mg/L of TC, 10 mg/L of CIP, 1.0 g/L of $BiVO_4$@BiOCl	500 W xenon lamp, visible light, UPW	90.32 71.32	200	[138]
tetracycline	15 mg/L of TC, 500 g/L of $Bi_2WO_6/CuBi_2O_4$	300 W xenon lamp, visible light, UPW	91.0	60	[139]
ciprofloxacin norfloxacin	10 mg/L of CIP/ NOR, 1g/L of Mg/Bi_2WO_6	300 W xenon lamp, visible light, UPW	99.1 89.44	150	[98]
norfloxacin	10 mg/L of NOR, 600 mg/L of Ag_3PO_4/Bi_2WO_6/MWCNTs	1000 W xenon lamp, visible light, UPW	94.34	180	[140]
ciprofloxacin	10 mg/L of CIP, 500 mg/L of 5 wt % Co_3O_4/Bi_2WO_6/PMS, 0.2 g/L of PMS	300 W xenon lamp, visible light, pH 6.5, UPW	86.2	5	[141]
ciprofloxacin	10 mg/L of CIP, 5 mg/L of Bi_3TaO_7 QDs/g-C_3N_4	86 W blue LED, pH 7, UPW	91.0	120	[70]
sulfamethoxazole	5 mg/L of SMX, 500 mg/L of Ag/g-C_3N_4/Bi_3TaO_7	300 W xenon lamp, visible light, pH 6.5, UPW	98	25	[71]
ciprofloxacin	20 mg/L of CIP, 250 mg/L of CdS-Bi_2MoO_6/RGO	500 W xenon lamp, visible light, UPW	91.0	60	[142]
tetracycline	15 mg/L of TET, 600 mg/L of $CuInS_2/Bi_2MoO_6$	300 W xenon lamp, visible light, pH 7, UPW	84.7	120	[143]
ciprofloxacin tetracycline	10 mg/L of CIP, 20 mg/L of TC, 250 mg/L of $Bi_4O_5Br_2$/CdS	350 W xenon lamp, visible light, UPW	85 85	60 60	[144]
norfloxacin	10 mg/L of NOR, 250 mg/L of ZnO/Bi_2WO_6	natural sunlight, pH 6.6, UPW	99.7	120	[145]
levofloxacin	15 mg/L of LEV, 900 mg/L of Bi_2CrO_6/g–C_3N_4	100 W LED, visible light, pH 6, UPW	92.5	120	[146]
chlortetracycline	20 mg/L of CTC, 900 mg/L of Bi_2WO_6/g-C_3N_4/ACF	300 W xenon lamp, visible light, SWW	90.2	69	[147]
ciprofloxacin tetracycline	10 mg/L of CIP, 20 mg/L of TC, 500 mg/L of $BiVO_4/Bi_2WO_6/WO_3$	300 W xenon lamp, simulated sunlight, pH 6, UPW	67.5 33.2	100 75	[148]
tetracycline oxytetracycline	20 mg/L of TC/ OTC, 400 mg/L of In_2O_3/Bi_2WO_6	300 W xenon lamp, simulated sunlight, UPW	86 82	70	[149]
norfloxacin levofloxacin	10 mg/L of NOR/ LEV, 400 mg/L of g-C_3N_4/Bi_2WO_6	300 W xenon lamp, simulated sunlight, UPW	85.75 85.82	120	[150]
chloramphenicol	50 mg/L of CHL, 1 g/L of Ti-Bi_2WO_6@BC	500 W xenon lamp, visible light, pH 7, UPW	92.44	120	[97]

[a]SWW: synthetic wastewater, UPW: ultrapure water, and DW: distilled water

Table 4: Degradation of antibiotics by graphitic carbon nitride-based photocatalysts.[a]

Antibiotic	Dosages of antibiotics and catalysts	Light source and other parameters	Removal efficiency (%)	Reaction time (min)	Ref.
tetracycline	40 mg/L of TC, 400 mg/L of g-C_3N_4	300 W xenon lamp, visible light, pH 4.18, UPW	84.1	90	[101]
tetracycline	20 mg/L of TC, 1 g/L of Nb_2O_5/g-C_3N_4	250 W xenon lamp, simulated sunlight, pH 3, SWW	90.1	150	[151]
sulfamethazine	10 mg/L of SMT, 101 g/L of C doping g-C_3N_4	300 W xenon arc lamp, visible light, UPW	98.0	60	[152]
sulfamethazine	30 mg/L of SMT, 500 mg/L of g-C_3N_4	300 W xenon arc lamp, visible light, pH 3, UPW	99.7	60	[153]

Table 4: Degradation of antibiotics by graphitic carbon nitride-based photocatalysts.[a] (continued)

erythromycin	50 mg/L of ERY, 500 mg/L of CdS/g-C_3N_4	35 W xenon lamp, visible light, pH 5, UPW	81.02	60	[106]
tetracycline	150 mg/L of TC, 400 mg/L of CoO/g-C_3N_4	300 W xenon lamp, visible light, UPW	73.12	300	[107]
metronidazole	10 mg/L of MTZ, 1000 mg/L of P-doped g-C_3N_4/Co_3O_4	250 W xenon lamp, visible light, UPW	70	180	[58]
sulfamethoxazole	5 mg/L of SMX, 1000 mg/L Ag-P-codoped g-C_3N_4	350 W xenon lamp, visible light, pH 9, SWW	99	30	[62]
sulfamethazine	5 mg/L of SMT, 200 mg/L 2D/1D g-C_3N_4/TNTs	450 W xenon lamp, pH 7, UWW	100	300	[154]
tylosin	25 mg/L of TYL, 500 g/L of Sm-doped gC_3N_4	35 W xenon lamp, simulated sunlight, pH 3–11, UPW	78.4	90	[59]
tetracycline	50 mg/L of TC, 11 g/L of ZnO/g-C_3N_4	500 W mercury lamp, UV light, RWW	93.4	120	[105]
tetracycline	10 mg/L of TC, 10 mg/L of pyridazine doped g-C_3N_4	300 W xenon lamp, visible light, pH 6, UPW	95	60	[103]
pefloxacin	10 mg/L of PEF/ENR/CIP, 50 mg/L of g-C_3N_4/TCNQ-X	300 W xenon lamp, visible light, UPW	91.6	180	[102]
tetracycline	8×10^{-5} M of TC/DOX, 60 mg/L of K,P-co-doped g-C_3N_4/GO/$CoFe_2O_4$	500 W halogen lamp, visible light, pH 7, UPW	85	60	[64]

[a]RWW: real wastewater, SWW: synthetic wastewater, and UPW: ultrapure water

Table 5: Degradation of antibiotics by graphene oxide-based photocatalysts.[a]

Antibiotic	Dosages of antibiotics and catalysts	Light source and other parameters	Removal efficiency (%)	Reaction time (min)	Ref.
amoxicillin	50 mg/L of AMX, 400 mg/L of GO/TiO_2	36 W UV lamp, UV light, pH 6, UPW	99	60	[155]
tetracycline	50 mg/L of TC, 50 mg/L of GO/ZnO	300 W xenon lamp, visible light, pH 11, UPW	74	100	[156]
tetracycline	20 mg/L of TC, 30 mg/L of g-C_3N_4/Ag_2CO_3/GO	300 W xenon lamp, visible light, UPW	97.6	100	[108]
ciprofloxacin	10 mg/L of CIP, 20 mg/L of $BiPO_4$@GO-MMIPs	300 W xenon lamp, visible light, UPW	100	80	[157]
tetracycline	20 mg/L of TC, 25 mg/L of BiOBr/MoS_2/GO	300 W xenon lamp, visible light, pH 11, UPW	98	40	[111]
trimethoprim	20 mg/L of TMP, 2.5 mg/L of CuFe-LDH/GO	18 W Philips TL-D, UV light, pH 8.8, UPW	90.8	120	[158]
sulfamethoxazole	0.10 mg/L of SMX, 100 mg/L of TiO_2-rGO	1000 W xenon lamp, simulated sunlight, pH 5.2–6.2, RWW	87.0	60	[112]
sulfamethoxazole	20 mg/L of SMX, 200 mg/L of Ag_3PO_4/N-doped rGO	250 W xenon arc lamp, visible light, pH 5.8, UPW	93.8	60	[113]
ciprofloxacin	10 mg/L of CIP, 300 mg/L of rGO-$BiVO_4$-ZnO	tungsten lamp (150 mW·cm^{-2}), visible light, pH 7, UPW	98.4	60	[159]
ciprofloxacin	10 mg/L of CIP, 20 mg/L of NOR/TC, 50 mg/L of rGO/$Bi_4O_5Br_2$	500 W of xenon lamp, visible light, UPW	97.6	60	[160]
norfloxacin			80.7		
tetracycline			98.7		
chloramphenicol	1000 mg/L of CAP, 500 mg/L of rGO-ZnO	4 W of UVP compact lamp, UV light, pH 2, UPW	90.8	40	[161]
oxytetracycline	10 mg/L of OTC, 300 mg/L of cobalt ferrite/rGO	300 W xenon lamp, visible light, pH 7.36, UPW	84.7	40	[162]
tetracycline	25 mg/L of TC, 25 mg/L of rGO/MoO_3/TiO_2	300 W xenon lamp, visible light, UPW	94	80	[163]
ciprofloxacin	10 mg/L of CIP/SMX, 25 mg/L of Fc@rGO-ZnO	10 W UV lamp, UV light, pH 4, UPW	97.09	180	[82]

Table 5: Degradation of antibiotics by graphene oxide-based photocatalysts.[a] (continued)

ofloxacin	40 mM of OFX, 20 mg/L of rGO-ZnS-CuS	tungsten lamp (300 mW·cm^{-2}), visible light, UPW	86.65	135	[164]
oxytetracycline	20 mg/L of OTC, 370 mg/L of rGO/α-Fe_2O_3/ZnO, 2.06 mM of PS	24 W LED, visible light, pH 4, UPW	98	90	[110]
norfloxacin	10 mg/L of NOR, 0.75 mg/L of rGO–SnSe	300 W xenon lamp, visible light, pH 7, UPW	90.7	70	[165]

[a]RWW: real wastewater and UPW: ultrapure water

Table 6: Degradation of antibiotics by tungsten oxide-based photocatalysts.[a]

Antibiotic	Dosages of antibiotics and catalysts	Light source and other parameters	Removal efficiency (%)	Reaction time (min)	Ref.
sulfanilamide	10 mg/L of SAM, 500 mg/L of Ag doped WO_3	200 W xenon arc lamp, visible light, pH 5, UPW	96.2	300	[166]
tetracycline	35 mg/L of TC, 1000 mg/L of AgI/WO_3	300 W xenon lamp, visible light, pH 6.62, UPW	75.0	60	[119]
tetracycline	10 mg/L of TC, 500 mg/L of Ag_3VO_4/WO_3	300 W xenon lamp, visible light, UPW	71.2	30	[117]
sulfamethoxazole	10 mg/L of SMX, 1 g/L of WO_3/g-C_3N_4	300 W xenon lamp, simulated sunlight, UPW	91.7	240	[115]
sulfamethoxazole	10 mg/L of SMX, 2 g/L of WO_3/rGO	200 W xenon arc lamp, simulated sunlight, pH 7, RWW	98.0	80	[116]
sulfamethoxazole	10 mg/L of SMX, 2 g/L of WO_3-MWCNTs (WO_3-CNT)	300 W xenon arc lamp, simulated sunlight, UPW	88.5	180	[118]
tetracycline	50 mg/L of TC, 50 mg/L of Cu-doped WO_3	300 W xenon lamp, visible light, pH 10, UPW	93.7	60	[167]
levofloxacin	20 mg/L of LVX, 50 mg/L of WO_4	300 W xenon lamp, visible light, pH 7, UPW	84.3	120	[168]

[a]RWW: real wastewater and UPW: ultrapure water

gies have shown significant improvements in the efficiency of antibiotic degradation by either narrowing the bandgap of the photocatalyst or improving the migration of photogenerated charge carriers and promoting efficient charge separation, contributing to the development of sustainable and highly effective photocatalytic systems. However, despite remarkable results, several challenges need to be addressed, such as the presence of multiple sources of pollutants in wastewater, the complex nature of antibiotics, the necessity to understand the mechanism of photocatalytic degradation at the atomic level, and the development of catalysts that can withstand negative influences from environmental matrices.

To further advance the field of photocatalysis, future research should delve into new and innovative approaches, including developing novel materials, optimizing catalyst preparation methods, enhancing photocatalyst recycling capabilities, and exploring synergistic treatments. The focus should be on designing photocatalysts with quasi-identical photoactivity and ease of separation to minimize waste and reduce operating costs. It is also suggested to perform cost-efficiency analyses, comparing the energy requirements for conventional treatment methods such as AOPs with photocatalysis process for large-scale wastewater treatment.

Extensive research on sustainable and recyclable photocatalysts is urgently needed to tackle environmental concerns related to antibiotic degradation effectively. Strong political support, adequate funding, and effective interdisciplinary collaboration are crucial for advancing progress in this field and successfully applying laboratory findings to real-world solutions. Through careful consideration of these challenges and utilization of cutting-edge technologies, semiconductor-based photocatalytic active nanomaterials offer a promising opportunity to mitigate antibiotic pollution and protect the well-being of our environment.

Applications involving the use of semiconductor-based nanoscale photocatalysts for environmental remediation relate directly to several sustainable development goals (SDGs), specifically SDG 3 (Good Health and Well-Being), SDG 6 (Clean Water and Sanitation), and SDG 12 (Responsible Consumption and Production). Nanoscale photocatalysts contribute to SDG 3 by reducing waterborne diseases and health risks through the effective degradation of toxic pollutants, antibiotics, antibiotic-resistant bacteria, and emerging contaminants in wastewater. Additionally, these advanced materials contribute to SDG 6 by offering environmentally friendly and energy-efficient solutions for water management. Furthermore, their integration into resource-efficient systems supports SDG 12 by minimizing chemical usage and production of waste through a circular approach to environmental management.

Acknowledgements

The authors express their appreciation for the invaluable support of all the students and staff at the Water and Environmental Lab of the Department of Chemistry, Chittagong University of Engineering and Technology (CUET).

Funding

This research was carried out with the support of the Advanced Research in Education Grants Program (ET20221947), funded by the Bangladesh Bureau of Educational Information and Statistics (BANBEIS) under the Ministry of Education, Government of the People's Republic of Bangladesh. The authors would also like to acknowledge the DRE research grant (CUET/DRE/2022-23/CHEM/022) received from CUET, Chattogram, Bangladesh.

Conflict of Interest

The authors declare that there are no conflicting financial interests or personal relationships that could have potentially influenced the findings presented in this paper.

Author Contributions

Yunus Ahmed: conceptualization; funding acquisition; investigation; project administration; supervision; validation; visualization; writing – review & editing. Keya Rani Dutta: conceptualization; data curation; investigation; methodology; validation; writing – original draft. Parul Akhtar: conceptualization; formal analysis; validation; visualization; writing – original draft. Md. Arif Hossen: conceptualization; formal analysis; investigation; validation; visualization; writing – review & editing. Md. Jahangir Alam: conceptualization; supervision; visualization; writing – review & editing. Obaid A. Alharbi: conceptualization; validation; visualization; writing – review & editing. Hamad AlMohamadi: conceptualization; validation; visualization; writing – review & editing. Abdul Wahab Mohammad: conceptualization; supervision; visualization; writing – review & editing.

ORCID® iDs

Yunus Ahmed - https://orcid.org/0000-0002-8556-1944

Data Availability Statement

Data sharing is not applicable as no new data was generated or analyzed in this study.

References

1. Manzetti, S.; Ghisi, R. *Mar. Pollut. Bull.* **2014,** *79,* 7–15. doi:10.1016/j.marpolbul.2014.01.005
2. Omuferen, L. O.; Maseko, B.; Olowoyo, J. O. *Environ. Monit. Assess.* **2022,** *194,* 306. doi:10.1007/s10661-022-09846-4
3. Alhaji, N. B.; Odetokun, I. A.; Adamu, A. M.; Hassan, A.; Lawan, M. K.; Fasina, F. O. *Vet. Res. Commun.* **2023,** *47,* 233–245. doi:10.1007/s11259-022-09944-1
4. Adebowale, O. 18 - Antimicrobial therapy and the risk for antimicrobial resistance in milk-borne diseases. In *The Microbiology, Pathogenesis and Zoonosis of Milk Borne Diseases;* Rana, T., Ed.; Academic Press, 2024; pp 333–356. doi:10.1016/b978-0-443-13805-8.00021-1
5. Focazio, M. J.; Kolpin, D. W.; Barnes, K. K.; Furlong, E. T.; Meyer, M. T.; Zaugg, S. D.; Barber, L. B.; Thurman, M. E. *Sci. Total Environ.* **2008,** *402,* 201–216. doi:10.1016/j.scitotenv.2008.02.021
6. Bilal, M.; Mehmood, S.; Rasheed, T.; Iqbal, H. M. N. *Curr. Opin. Environ. Sci. Health* **2020,** *13,* 68–74. doi:10.1016/j.coesh.2019.11.005
7. Ahmed, Y.; Siddiqua Maya, A. A.; Akhtar, P.; Alam, M. S.; AlMohamadi, H.; Islam, M. N.; Alharbi, O. A.; Rahman, S. M. *J. Environ. Manage.* **2024,** *370,* 122614. doi:10.1016/j.jenvman.2024.122614
8. Ahmed, Y.; Rahman, M. M.; Alam, M. S.; Miah, M. I.; Choudhury, M. S. H.; Alharbi, O. A.; Akhtar, P.; Rahman, S. M. *J. Water Process Eng.* **2024,** *65,* 105724. doi:10.1016/j.jwpe.2024.105724
9. Guo, J.; Wang, Y.; Ahmed, Y.; Jin, M.; Li, J. Control strategies to combat dissemination of antibiotic resistance in urban water systems. In *Antibiotic Resistance in the Environment : A Worldwide Overview;* Manaia, C. M.; Donner, E.; Vaz-Moreira, I.; Hong, P., Eds.; The Handbook of Environmental Chemistry, Vol. 91; Springer International Publishing: Cham, Switzerland, 2020; pp 147–187. doi:10.1007/698_2020_474
10. Ahmed, Y.; Zhong, J.; Wang, Z.; Wang, L.; Yuan, Z.; Guo, J. *Environ. Sci. Technol.* **2022,** *56,* 15156–15166. doi:10.1021/acs.est.2c03334
11. Ahmed, Y.; Zhong, J.; Yuan, Z.; Guo, J. *Water Res.* **2021,** *197,* 117075. doi:10.1016/j.watres.2021.117075
12. Ahmed, Y.; Lu, J.; Yuan, Z.; Bond, P. L.; Guo, J. *Water Res.* **2020,** *179,* 115878. doi:10.1016/j.watres.2020.115878
13. Zhong, J.; Ahmed, Y.; Carvalho, G.; Wang, Z.; Wang, L.; Mueller, J. F.; Guo, J. *Chem. Eng. J.* **2022,** *433,* 133839. doi:10.1016/j.cej.2021.133839
14. Zhong, J.; Ahmed, Y.; Yu, Z.; Mueller, J. F.; Guo, J. *ACS ES&T Water* **2023,** *3,* 6–15. doi:10.1021/acsestwater.2c00237

15. Ahmed, Y.; Akter, T.; Prima, M.; Dutta, K. R.; Mukut, S.; Ahsan, M.; Rahman, M. M.; Hyder, M. K. M. Z. *J. Environ. Chem. Eng.* **2025,** 115094. doi:10.1016/j.jece.2024.115094
16. Kümmerer, K. *Chemosphere* **2009,** *75,* 435–441. doi:10.1016/j.chemosphere.2008.12.006
17. Dadgostar, P. *Infect. Drug Resist.* **2019,** *12,* 3903–3910. doi:10.2147/idr.s234610
18. Akhtar, P.; Ahmed, Y.; Islam, F.; Alam, K.; Mary, M.; Islam, M. Z.; Bhuiyan, M. M. H.; Yaakob, Z. *Asian J. Chem.* **2016,** *28,* 60–68. doi:10.14233/ajchem.2016.19230
19. Ahmed, Y.; Zhong, J.; Yuan, Z.; Guo, J. *J. Hazard. Mater.* **2022,** *430,* 128408. doi:10.1016/j.jhazmat.2022.128408
20. Choi, K.-J.; Kim, S.-G.; Kim, S.-H. *J. Hazard. Mater.* **2008,** *151,* 38–43. doi:10.1016/j.jhazmat.2007.05.059
21. Zhu, Y.-M.; Chen, Y.; Lu, H.; Jin, K.; Lin, Y.; Ren, H.; Xu, K. *Water Res.* **2024,** *262,* 122107. doi:10.1016/j.watres.2024.122107
22. Lu, Z.; Liu, G.; Xie, H.; Zhai, Y.; Li, X. *J. Environ. Manage.* **2024,** *368,* 122115. doi:10.1016/j.jenvman.2024.122115
23. Mdluli, N. S.; Nomngongo, P. N.; Mketo, N. The occurrence, effect and biodegradation of antibiotics using metallic biogenic nanomaterials in water. In *Biogenic Nanomaterials for Environmental Sustainability: Principles, Practices, and Opportunities;* Shah, M. P.; Bharadvaja, N.; Kumar, L., Eds.; Environmental Science and Engineering; Springer International Publishing: Cham, Switzerland, 2024; pp 473–495. doi:10.1007/978-3-031-45956-6_19
24. Li, S.; Hofstra, N.; van de Schans, M. G. M.; Yang, J.; Li, Y.; Zhang, Q.; Ma, L.; Strokal, M.; Kroeze, C.; Chen, X.; Chen, X.; Zhang, F. *Environ. Sci. Technol. Lett.* **2023,** *10,* 1059–1067. doi:10.1021/acs.estlett.3c00536
25. Jeong, J.; Song, W.; Cooper, W. J.; Jung, J.; Greaves, J. *Chemosphere* **2010,** *78,* 533–540. doi:10.1016/j.chemosphere.2009.11.024
26. Garrido-Cardenas, J. A.; Esteban-García, B.; Agüera, A.; Sánchez-Pérez, J. A.; Manzano-Agugliaro, F. *Int. J. Environ. Res. Public Health* **2019,** *17,* 170. doi:10.3390/ijerph17010170
27. Boxi, S. S.; Paria, S. *RSC Adv.* **2015,** *5,* 37657–37668. doi:10.1039/c5ra03421c
28. Li, Z.; Wang, J.; Chang, J.; Fu, B.; Wang, H. *Sci. Total Environ.* **2023,** *857,* 159172. doi:10.1016/j.scitotenv.2022.159172
29. Wang, X.; Jing, J.; Zhou, M.; Dewil, R. *Chin. Chem. Lett.* **2023,** *34,* 107621. doi:10.1016/j.cclet.2022.06.044
30. Honarmandrad, Z.; Sun, X.; Wang, Z.; Naushad, M.; Boczkaj, G. *Water Resour. Ind.* **2023,** *29,* 100194. doi:10.1016/j.wri.2022.100194
31. Ahmed, Y.; Maya, A. A. S.; Akhtar, P.; AlMohamadi, H.; Mohammad, A. W.; Ashekuzzaman, S. M.; Olbert, A. I.; Uddin, M. G. *J. Environ. Chem. Eng.* **2025,** *13,* 115068. doi:10.1016/j.jece.2024.115068
32. Zhang, Y.; Zhao, Y.-G.; Maqbool, F.; Hu, Y. *J. Water Process Eng.* **2022,** *45,* 102496. doi:10.1016/j.jwpe.2021.102496
33. Lu, Z.; Ling, Y.; Sun, W.; Liu, C.; Mao, T.; Ao, X.; Huang, T. *Environ. Pollut.* **2022,** *308,* 119673. doi:10.1016/j.envpol.2022.119673
34. dos Santos, A. J.; Kronka, M. S.; Fortunato, G. V.; Lanza, M. R. V. *Curr. Opin. Electrochem.* **2021,** *26,* 100674. doi:10.1016/j.coelec.2020.100674
35. Bai, X.; Chen, W.; Wang, B.; Sun, T.; Wu, B.; Wang, Y. *Int. J. Mol. Sci.* **2022,** *23,* 8130. doi:10.3390/ijms23158130
36. Wang, X.; Yin, R.; Zeng, L.; Zhu, M. *Environ. Pollut.* **2019,** *253,* 100–110. doi:10.1016/j.envpol.2019.06.067
37. Li, M.-f.; Liu, Y.-g.; Zeng, G.-m.; Liu, N.; Liu, S.-b. *Chemosphere* **2019,** *226,* 360–380. doi:10.1016/j.chemosphere.2019.03.117
38. Zeng, H.; Li, J.; Zhao, W.; Xu, J.; Xu, H.; Li, D.; Zhang, J. *Int. J. Environ. Res. Public Health* **2022,** *19,* 11256. doi:10.3390/ijerph191811256
39. Galarza, J. A.; Murphy, L.; Mappes, J. *Proc. R. Soc. B* **2021,** *288,* 20211819. doi:10.1098/rspb.2021.1819
40. Leung, K. C.; Huang, Q.; St-Hilaire, S.; Liu, H.; Zheng, X.; Cheung, K. B.; Zwetsloot, I. M. *Prev. Vet. Med.* **2020,** *181,* 105052. doi:10.1016/j.prevetmed.2020.105052
41. Wang, K.; Zhuang, T.; Su, Z.; Chi, M.; Wang, H. *Sci. Total Environ.* **2021,** *788,* 147811. doi:10.1016/j.scitotenv.2021.147811
42. Polianciuc, S. I.; Gurzău, A. E.; Kiss, B.; Ştefan, M. G.; Loghin, F. *Med. Pharm. Rep.* **2020,** *93,* 231. doi:10.15386/mpr-1742
43. Wang, R.; Ji, M.; Zhai, H.; Guo, Y.; Liu, Y. *Sci. Total Environ.* **2021,** *796,* 148919. doi:10.1016/j.scitotenv.2021.148919
44. Xue, J.; Lei, D.; Zhao, X.; Hu, Y.; Yao, S.; Lin, K.; Wang, Z.; Cui, C. *Chemosphere* **2022,** *291,* 132837. doi:10.1016/j.chemosphere.2021.132837
45. Hassoun-Kheir, N.; Stabholz, Y.; Kreft, J.-U.; de la Cruz, R.; Romalde, J. L.; Nesme, J.; Sørensen, S. J.; Smets, B. F.; Graham, D.; Paul, M. *Sci. Total Environ.* **2020,** *743,* 140804. doi:10.1016/j.scitotenv.2020.140804
46. Bhagat, C.; Kumar, M.; Tyagi, V. K.; Mohapatra, P. K. *npj Clean Water* **2020,** *3,* 42. doi:10.1038/s41545-020-00087-x
47. Fatta-Kassinos, D.; Vasquez, M. I.; Kümmerer, K. *Chemosphere* **2011,** *85,* 693–709. doi:10.1016/j.chemosphere.2011.06.082
48. Corredor, M.; Muñoz-Gómez, A. Pharmaceutical antibiotics at a significant level in nature: From hospitals, livestock, and plants to soil, water, and sea. In *Emerging Contaminants;* Nuro, A., Ed.; IntechOpen: Rijeka, 2021. doi:10.5772/intechopen.95368
49. Singh, A.; Saluja, S. Microbial Degradation of Antibiotics from Effluents. In *Recent Advances in Microbial Degradation;* Inamuddin; Ahamed, M. I.; Prasad, R., Eds.; Environmental and Microbial Biotechnology; Springer Singapore:: Singapore, 2021; pp 389–404. doi:10.1007/978-981-16-0518-5_15
50. Chaturvedi, P.; Shukla, P.; Giri, B. S.; Chowdhary, P.; Chandra, R.; Gupta, P.; Pandey, A. *Environ. Res.* **2021,** *194,* 110664. doi:10.1016/j.envres.2020.110664
51. Lulijwa, R.; Rupia, E. J.; Alfaro, A. C. *Rev. Aquacult.* **2020,** *12,* 640–663. doi:10.1111/raq.12344
52. Krishnan, A.; Swarnalal, A.; Das, D.; Krishnan, M.; Saji, V. S.; Shibli, S. M. A. *J. Environ. Sci.* **2024,** *139,* 389–417. doi:10.1016/j.jes.2023.02.051
53. Kaur, A.; Bajaj, B.; Kaushik, A.; Saini, A.; Sud, D. *Mater. Sci. Eng., B* **2022,** *286,* 116005. doi:10.1016/j.mseb.2022.116005
54. Qin, K.; Zhao, Q.; Yu, H.; Xia, X.; Li, J.; He, S.; Wei, L.; An, T. *Environ. Res.* **2021,** *199,* 111360. doi:10.1016/j.envres.2021.111360
55. Velempini, T.; Prabakaran, E.; Pillay, K. *Mater. Today Chem.* **2021,** *19,* 100380. doi:10.1016/j.mtchem.2020.100380
56. El-Khawaga, A. M.; Zidan, A.; El-Mageed, A. I. A. A. *J. Mol. Struct.* **2023,** *1281,* 135148. doi:10.1016/j.molstruc.2023.135148
57. Suwannaruang, T.; Kidkhunthod, P.; Butburee, T.; Shivaraju, H. P.; Shahmoradi, B.; Wantala, K. *Surf. Interfaces* **2021,** *23,* 101013. doi:10.1016/j.surfin.2021.101013
58. Zhao, Z.; Fan, J.; Deng, X.; Liu, J. *Chem. Eng. J.* **2019,** *360,* 1517–1529. doi:10.1016/j.cej.2018.10.239
59. Li, G.; Wang, R.; Wang, B.; Zhang, J. *Appl. Surf. Sci.* **2020,** *517,* 146212. doi:10.1016/j.apsusc.2020.146212

60. Shen, J.-H.; Tang, Y.-H.; Jiang, Z.-W.; Liao, D.-Q.; Horng, J.-J. *J. Alloys Compd.* **2021,** *862,* 158697. doi:10.1016/j.jallcom.2021.158697
61. Rahman, M. S.; Suvo, M. A. H.; Islam, M. M. T.; Noor, A. R.; Yeachin, N.; Bhuiyan, M. A. *Colloids Surf., A* **2024,** *690,* 133660. doi:10.1016/j.colsurfa.2024.133660
62. Nguyen, T.-B.; Huang, C. P.; Doong, R.-a.; Chen, C.-W.; Dong, C.-D. *Chem. Eng. J.* **2020,** *384,* 123383. doi:10.1016/j.cej.2019.123383
63. Huang, X.; Yang, W.; Zhang, G.; Yan, L.; Zhang, Y.; Jiang, A.; Xu, H.; Zhou, M.; Liu, Z.; Tang, H.; Dionysiou, D. D. *Catal. Today* **2021,** *361,* 11–16. doi:10.1016/j.cattod.2019.10.034
64. Kumar, R.; Sudhaik, A.; Sonu; Nguyen, V.-H.; Van Le, Q.; Ahamad, T.; Thakur, S.; Kumar, N.; Hussain, C. M.; Singh, P.; Raizada, P. *J. Taiwan Inst. Chem. Eng.* **2023,** *150,* 105077. doi:10.1016/j.jtice.2023.105077
65. Chen, D.; Cheng, Y.; Zhou, N.; Chen, P.; Wang, Y.; Li, K.; Huo, S.; Cheng, P.; Peng, P.; Zhang, R.; Wang, L.; Liu, H.; Liu, Y.; Ruan, R. *J. Cleaner Prod.* **2020,** *268,* 121725. doi:10.1016/j.jclepro.2020.121725
66. Yu, W.; Zhang, J.; Peng, T. *Appl. Catal., B* **2016,** *181,* 220–227. doi:10.1016/j.apcatb.2015.07.031
67. Ren, Y.; Zeng, D.; Ong, W.-J. *Chin. J. Catal.* **2019,** *40,* 289–319. doi:10.1016/s1872-2067(19)63293-6
68. Nguyen, T. D.; Lee, T.; Van Tran, T.; Nguyen, V. H.; Nong, L. X.; Bach, L. G.; Vo, D.-V. N. *Environ. Chem. Lett.* **2023,** *21,* 935–980. doi:10.1007/s10311-022-01533-7
69. Wu, K.; Qin, Z.; Zhang, X.; Guo, R.; Ren, X.; Pu, X. *J. Mater. Sci.* **2020,** *55,* 4017–4029. doi:10.1007/s10853-019-04300-2
70. Wang, K.; Zhang, G.; Li, J.; Li, Y.; Wu, X. *ACS Appl. Mater. Interfaces* **2017,** *9,* 43704–43715. doi:10.1021/acsami.7b14275
71. Ren, M.; Ao, Y.; Wang, P.; Wang, C. *Chem. Eng. J.* **2019,** *378,* 122122. doi:10.1016/j.cej.2019.122122
72. Rasouli, K.; Alamdari, A.; Sabbaghi, S. *Sep. Purif. Technol.* **2023,** *307,* 122799. doi:10.1016/j.seppur.2022.122799
73. Erim, B.; Ciğeroğlu, Z.; Bayramoğlu, M. *J. Mol. Struct.* **2021,** *1234,* 130194. doi:10.1016/j.molstruc.2021.130194
74. Erim, B.; Ciğeroğlu, Z.; Şahin, S.; Vasseghian, Y. *Chemosphere* **2022,** *291,* 132929. doi:10.1016/j.chemosphere.2021.132929
75. Jeyaprakash, J. S.; Rajamani, M.; Mani, P.; Yazhini, C.; Sonawane, S. H.; Neppolian, B. *Ind. Eng. Chem. Res.* **2024,** *63,* 5135–5147. doi:10.1021/acs.iecr.3c04429
76. Hunge, Y. M.; Yadav, A. A.; Kang, S.-W.; Jun Lim, S.; Kim, H. *J. Photochem. Photobiol., A* **2023,** *434,* 114250. doi:10.1016/j.jphotochem.2022.114250
77. Gao, B.; Dong, S.; Liu, J.; Liu, L.; Feng, Q.; Tan, N.; Liu, T.; Bo, L.; Wang, L. *Chem. Eng. J.* **2016,** *304,* 826–840. doi:10.1016/j.cej.2016.07.029
78. Chen, L.; Ma, W.; Dai, J.; Zhao, J.; Li, C.; Yan, Y. *J. Photochem. Photobiol., A* **2016,** *328,* 24–32. doi:10.1016/j.jphotochem.2016.04.026
79. Mohamed, R. M.; Ismail, A. A.; Alhaddad, M. *Sep. Purif. Technol.* **2021,** *266,* 118588. doi:10.1016/j.seppur.2021.118588
80. Hu, L.; Xing, M.; He, X.; Yang, K.; Zhu, J.; Wang, J.; He, J.; Shi, J. *J. Mater. Sci.: Mater. Electron.* **2023,** *34,* 2273. doi:10.1007/s10854-023-11690-2
81. Yu, S.; Zhou, J.; Ren, Y.; Yang, Z.; Zhong, M.; Feng, X.; Su, B.; Lei, Z. *Chem. Eng. J.* **2023,** *451,* 138959. doi:10.1016/j.cej.2022.138959
82. Roy, N.; Kannabiran, K.; Mukherjee, A. *Chemosphere* **2023,** *333,* 138912. doi:10.1016/j.chemosphere.2023.138912
83. Senasu, T.; Narenuch, T.; Wannakam, K.; Chankhanittha, T.; Nanan, S. *J. Mater. Sci.: Mater. Electron.* **2020,** *31,* 9685–9694. doi:10.1007/s10854-020-03514-4
84. Wang, G.; Zhang, S.; Lu, H.; Lu, C.; Yang, M.; Tang, K.; Tang, A. *Environ. Sci.: Nano* **2023,** *10,* 3423–3438. doi:10.1039/d3en00582h
85. Subhiksha, V.; Kokilavani, S.; Sudheer Khan, S. *Chemosphere* **2022,** *290,* 133228. doi:10.1016/j.chemosphere.2021.133228
86. Chen, L.; Li, Y.; Zhang, J.; Li, M.; Yin, W.; Chen, X. *Inorg. Chem. Commun.* **2022,** *140,* 109414. doi:10.1016/j.inoche.2022.109414
87. Ren, A.; Liu, C.; Hong, Y.; Shi, W.; Lin, S.; Li, P. *Chem. Eng. J.* **2014,** *258,* 301–308. doi:10.1016/j.cej.2014.07.071
88. Zhu, Y.; Xue, J.; Xu, T.; He, G.; Chen, H. *J. Mater. Sci.: Mater. Electron.* **2017,** *28,* 8519–8528. doi:10.1007/s10854-017-6574-6
89. Chen, M.; Yao, J.; Huang, Y.; Gong, H.; Chu, W. *Chem. Eng. J.* **2018,** *334,* 453–461. doi:10.1016/j.cej.2017.10.064
90. Thakur, V.; Singh, S.; Kumar, P.; Rawat, S.; Chandra Srivastava, V.; Lo, S.-L.; Lavrenčič Štangar, U. *Chem. Eng. J.* **2023,** *475,* 146100. doi:10.1016/j.cej.2023.146100
91. Wang, M.; Lu, G.; Jiang, R.; Dang, T.; Liu, J. *J. Colloid Interface Sci.* **2022,** *622,* 995–1007. doi:10.1016/j.jcis.2022.04.179
92. Hao, R.; Xiao, X.; Zuo, X.; Nan, J.; Zhang, W. *J. Hazard. Mater.* **2012,** *209-210,* 137–145. doi:10.1016/j.jhazmat.2012.01.006
93. He, Q.; Ge, M.; Yu, Q. *J. Chem. Sci.* **2021,** *133,* 98. doi:10.1007/s12039-021-01955-w
94. Chen, F.; Huang, H.; Guo, L.; Zhang, Y.; Ma, T. *Angew. Chem., Int. Ed.* **2019,** *58,* 10061–10073. doi:10.1002/anie.201901361
95. Yang, L.; Wang, J.; Zhang, Y.; Zhou, B.; Tan, P.; Pan, J. *J. Mater. Sci.: Mater. Electron.* **2022,** *33,* 13303–13315. doi:10.1007/s10854-022-08269-8
96. Koutavarapu, R.; Jang, W. Y.; Rao, M. C.; Arumugam, M.; Shim, J. *Chemosphere* **2022,** *305,* 135465. doi:10.1016/j.chemosphere.2022.135465
97. Wang, T.; Shi, H.; Kumar, A.; Zhang, D.; Wang, H.; Wang, S.; Zheng, J. *Sep. Purif. Technol.* **2024,** *332,* 125780. doi:10.1016/j.seppur.2023.125780
98. Zhu, F.; Lv, Y.; Li, J.; Ding, J.; Xia, X.; Wei, L.; Jiang, J.; Zhang, G.; Zhao, Q. *Chemosphere* **2020,** *252,* 126577. doi:10.1016/j.chemosphere.2020.126577
99. Huang, R.; Wu, J.; Zhang, M.; Liu, B.; Zheng, Z.; Luo, D. *Mater. Des.* **2021,** *210,* 110040. doi:10.1016/j.matdes.2021.110040
100. Balakrishnan, A.; Chinthala, M. *Chemosphere* **2022,** *297,* 134190. doi:10.1016/j.chemosphere.2022.134190
101. Chen, J.; Yan, Z.; Chen, Y.; Yao, K.; Xu, Z. *Appl. Surf. Sci.* **2023,** *634,* 157637. doi:10.1016/j.apsusc.2023.157637
102. Li, Q.; Wen, N.; Zhang, W.; Yu, L.; Shen, J.; Li, S.; Lv, Y. *Micromachines* **2023,** *14,* 941. doi:10.3390/mi14050941
103. Zhan, X.; Zhao, Y.; Sun, Y.; Lei, C.; Wang, H.; Shi, H. *Chemosphere* **2022,** *307,* 136087. doi:10.1016/j.chemosphere.2022.136087
104. Xing, J.; Wang, N.; Li, X.; Wang, J.; Taiwaikuli, M.; Huang, X.; Wang, T.; Zhou, L.; Hao, H. *J. Environ. Chem. Eng.* **2022,** *10,* 108782. doi:10.1016/j.jece.2022.108782
105. Wang, X.; Zhang, P.; Li, L.; Li, N.; Su, X.; Wei, X.; Han, L. *Mater. Today Commun.* **2023,** *36,* 106732. doi:10.1016/j.mtcomm.2023.106732
106. Li, G.; Wang, B.; Zhang, J.; Wang, R.; Liu, H. *Appl. Surf. Sci.* **2019,** *478,* 1056–1064. doi:10.1016/j.apsusc.2019.02.035

107. Niu, J.; Xie, Y.; Luo, H.; Wang, Q.; Zhang, Y.; Wang, Y. *Chemosphere* **2019,** *218,* 169–178. doi:10.1016/j.chemosphere.2018.11.111
108. Liu, H.-Y.; Liang, C.; Niu, C.-G.; Huang, D.-W.; Du, Y.-B.; Guo, H.; Zhang, L.; Yang, Y.-Y.; Zeng, G.-M. *Appl. Surf. Sci.* **2019,** *475,* 421–434. doi:10.1016/j.apsusc.2019.01.018
109. Samsudin, M. F. R.; Frebillot, C.; Kaddoury, Y.; Sufian, S.; Ong, W.-J. *J. Environ. Manage.* **2020,** *270,* 110803. doi:10.1016/j.jenvman.2020.110803
110. Sanei, A.; Dashtian, K.; Yousefi Seyf, J.; Seidi, F.; Kolvari, E. *J. Environ. Manage.* **2023,** *332,* 117377. doi:10.1016/j.jenvman.2023.117377
111. Li, Y.; Lai, Z.; Huang, Z.; Wang, H.; Zhao, C.; Ruan, G.; Du, F. *Appl. Surf. Sci.* **2021,** *550,* 149342. doi:10.1016/j.apsusc.2021.149342
112. Karaolia, P.; Michael-Kordatou, I.; Hapeshi, E.; Drosou, C.; Bertakis, Y.; Christofilos, D.; Armatas, G. S.; Sygellou, L.; Schwartz, T.; Xekoukoulotakis, N. P.; Fatta-Kassinos, D. *Appl. Catal., B* **2018,** *224,* 810–824. doi:10.1016/j.apcatb.2017.11.020
113. Naraginti, S.; Yu, Y.-Y.; Fang, Z.; Yong, Y.-C. *Chem. Eng. J.* **2019,** *375,* 122035. doi:10.1016/j.cej.2019.122035
114. Nguyen, T. T.; Nam, S.-N.; Son, J.; Oh, J. *Sci. Rep.* **2019,** *9,* 9349. doi:10.1038/s41598-019-45644-8
115. Zhu, W.; Sun, F.; Goei, R.; Zhou, Y. *Catal. Sci. Technol.* **2017,** *7,* 2591–2600. doi:10.1039/c7cy00529f
116. Zhu, W.; Sun, F.; Goei, R.; Zhou, Y. *Appl. Catal., B* **2017,** *207,* 93–102. doi:10.1016/j.apcatb.2017.02.012
117. Yan, M.; Wu, Y.; Zhu, F.; Hua, Y.; Shi, W. *Phys. Chem. Chem. Phys.* **2016,** *18,* 3308–3315. doi:10.1039/c5cp05599g
118. Zhu, W.; Li, Z.; He, C.; Faqian, S.; Zhou, Y. *J. Alloys Compd.* **2018,** *754,* 153–162. doi:10.1016/j.jallcom.2018.04.286
119. Wang, T.; Quan, W.; Jiang, D.; Chen, L.; Li, D.; Meng, S.; Chen, M. *Chem. Eng. J.* **2016,** *300,* 280–290. doi:10.1016/j.cej.2016.04.128
120. Zhou, L.; Zhang, W.; Chen, L.; Deng, H.; Wan, J. *Catal. Commun.* **2017,** *100,* 191–195. doi:10.1016/j.catcom.2017.06.049
121. Zhang, H.; Wang, Z.; Li, R.; Guo, J.; Li, Y.; Zhu, J.; Xie, X. *Chemosphere* **2017,** *185,* 351–360. doi:10.1016/j.chemosphere.2017.07.025
122. Xie, X.; Li, S.; Zhang, H.; Wang, Z.; Huang, H. *Sci. Total Environ.* **2019,** *659,* 529–539. doi:10.1016/j.scitotenv.2018.12.401
123. Jahdi, M.; Mishra, S. B.; Nxumalo, E. N.; Mhlanga, S. D.; Mishra, A. K. *Appl. Catal., B* **2020,** *267,* 118716. doi:10.1016/j.apcatb.2020.118716
124. Sarafraz, M.; Sadeghi, M.; Yazdanbakhsh, A.; Amini, M. M.; Sadani, M.; Eslami, A. *Process Saf. Environ. Prot.* **2020,** *137,* 261–272. doi:10.1016/j.psep.2020.02.030
125. Chen, X.; Peng, X.; Jiang, L.; Yuan, X.; Fei, J.; Zhang, W. *Chem. Eng. J.* **2022,** *427,* 130945. doi:10.1016/j.cej.2021.130945
126. Abdullah, M.; Iqbal, J.; Ur Rehman, M. S.; Khalid, U.; Mateen, F.; Arshad, S. N.; Al-Sehemi, A. G.; Algarni, H.; Al-Hartomy, O. A.; Fazal, T. *Chemosphere* **2023,** *317,* 137834. doi:10.1016/j.chemosphere.2023.137834
127. Sukidpaneenid, S.; Chawengkijwanich, C.; Pokhum, C.; Isobe, T.; Opaprakasit, P.; Sreearunothai, P. *J. Environ. Sci.* **2023,** *124,* 414–428. doi:10.1016/j.jes.2021.09.042
128. Chen, C.; Zeng, H.; Yi, M.; Xiao, G.; Xu, S.; Shen, S.; Feng, B. *Appl. Catal., B* **2019,** *252,* 47–54. doi:10.1016/j.apcatb.2019.03.083
129. Dong, S.; Cui, L.; Zhang, W.; Xia, L.; Zhou, S.; Russell, C. K.; Fan, M.; Feng, J.; Sun, J. *Chem. Eng. J.* **2020,** *384,* 123279. doi:10.1016/j.cej.2019.123279
130. Jia, Z.; Li, T.; Zheng, Z.; Zhang, J.; Liu, J.; Li, R.; Wang, Y.; Zhang, X.; Wang, Y.; Fan, C. *Chem. Eng. J.* **2020,** *380,* 122422. doi:10.1016/j.cej.2019.122422
131. Wu, S.; Su, Y.; Zhu, Y.; Zhang, Y.; Zhu, M. *Appl. Surf. Sci.* **2020,** *520,* 146339. doi:10.1016/j.apsusc.2020.146339
132. senasu, T.; Lorwanishpaisarn, N.; Hemavibool, K.; Nijpanich, S.; Chanlek, N.; Nanan, S. *Sep. Purif. Technol.* **2023,** *306,* 122735. doi:10.1016/j.seppur.2022.122735
133. Ma, X.; Chen, K.; Niu, B.; Li, Y.; Wang, L.; Huang, J.; She, H.; Wang, Q. *Chin. J. Catal.* **2020,** *41,* 1535–1543. doi:10.1016/s1872-2067(19)63486-8
134. Wang, W.; Han, Q.; Zhu, Z.; Zhang, L.; Zhong, S.; Liu, B. *Adv. Powder Technol.* **2019,** *30,* 1882–1896. doi:10.1016/j.apt.2019.06.006
135. Zheng, X.; Li, Y.; Peng, H.; Huang, Z.; Wang, H.; Wen, J. *Colloids Surf., A* **2021,** *621,* 126599. doi:10.1016/j.colsurfa.2021.126599
136. Dieu Cam, N. T.; Pham, H.-D.; Pham, T.-D.; Thu Phuong, T. T.; Van Hoang, C.; Thanh Tung, M. H.; Trung, N. T.; Huong, N. T.; Thu Hien, T. T. *Ceram. Int.* **2021,** *47,* 1686–1692. doi:10.1016/j.ceramint.2020.08.285
137. Truong, H. B.; Huy, B. T.; Ray, S. K.; Gyawali, G.; Lee, Y.-I.; Cho, J.; Hur, J. *Chemosphere* **2022,** *299,* 134320. doi:10.1016/j.chemosphere.2022.134320
138. Yang, Q.; Tan, G.; Yin, L.; Liu, W.; Zhang, B.; Feng, S.; Bi, Y.; Liu, Y.; Liu, T.; Wang, Z.; Ren, H.; Xia, A. *Chem. Eng. J.* **2023,** *467,* 143450. doi:10.1016/j.cej.2023.143450
139. Yuan, X.; Shen, D.; Zhang, Q.; Zou, H.; Liu, Z.; Peng, F. *Chem. Eng. J.* **2019,** *369,* 292–301. doi:10.1016/j.cej.2019.03.082
140. Zhu, Z.; Wang, C.; Liang, L.; Yu, D.; Sun, J.; Zhang, L.; Zhong, S.; Liu, B. *J. Nanosci. Nanotechnol.* **2020,** *20,* 2247–2258. doi:10.1166/jnn.2020.17368
141. Sun, J.; Shen, C.-H.; Guo, J.; Guo, H.; Yin, Y.-F.; Xu, X.-J.; Fei, Z.-H.; Liu, Z.-T.; Wen, X.-J. *J. Colloid Interface Sci.* **2021,** *588,* 19–30. doi:10.1016/j.jcis.2020.12.043
142. Chen, Z.; Liang, J.; Xu, X.; He, G.; Chen, H. *J. Mater. Sci.* **2020,** *55,* 6065–6077. doi:10.1007/s10853-020-04413-z
143. Guo, J.; Wang, L.; Wei, X.; Alothman, Z. A.; Albaqami, M. D.; Malgras, V.; Yamauchi, Y.; Kang, Y.; Wang, M.; Guan, W.; Xu, X. *J. Hazard. Mater.* **2021,** *415,* 125591. doi:10.1016/j.jhazmat.2021.125591
144. Cao, W.; Jiang, C.; Chen, C.; Zhou, H.; Wang, Y. *J. Alloys Compd.* **2021,** *861,* 158554. doi:10.1016/j.jallcom.2020.158554
145. Chankhanittha, T.; Somaudon, V.; Photiwat, T.; Youngme, S.; Hemavibool, K.; Nanan, S. *J. Phys. Chem. Solids* **2021,** *153,* 109995. doi:10.1016/j.jpcs.2021.109995
146. Hasanvandian, F.; Moradi, M.; Aghaebrahimi Samani, S.; Kakavandi, B.; Rahman Setayesh, S.; Noorisepehr, M. *Chemosphere* **2022,** *287,* 132273. doi:10.1016/j.chemosphere.2021.132273
147. Zhang, R.; Jiang, J.; Zeng, K. *Inorg. Chem. Commun.* **2022,** *140,* 109418. doi:10.1016/j.inoche.2022.109418
148. Cho, E.-C.; Hsiao, Y.-S.; Huang, J.-H.; Sung, M.-Y.; Chen, Y.-L.; Wu, N.-J.; Hsu, S.-C.; Weng, H. C.; Lee, K.-C. *J. Taiwan Inst. Chem. Eng.* **2023,** *149,* 104991. doi:10.1016/j.jtice.2023.104991
149. Yan, Q.; Guo, Z.; Wang, P.; Cheng, Y.; Wu, C.; Zuo, H. *J. Alloys Compd.* **2023,** *937,* 168362. doi:10.1016/j.jallcom.2022.168362
150. Ma, B.; Zha, Y.; Yu, P.; Chen, G.; Guo, Y.; Lan, Y.; Li, J.; Xia, W.; Zhao, B. *J. Alloys Compd.* **2023,** *952,* 170061. doi:10.1016/j.jallcom.2023.170061
151. Hong, Y.; Li, C.; Zhang, G.; Meng, Y.; Yin, B.; Zhao, Y.; Shi, W. *Chem. Eng. J.* **2016,** *299,* 74–84. doi:10.1016/j.cej.2016.04.092

152. Zhou, C.; Lai, C.; Huang, D.; Zeng, G.; Zhang, C.; Cheng, M.; Hu, L.; Wan, J.; Xiong, W.; Wen, M.; Wen, X.; Qin, L. *Appl. Catal., B* **2018,** *220,* 202–210. doi:10.1016/j.apcatb.2017.08.055
153. Zhou, C.; Zeng, Z.; Zeng, G.; Huang, D.; Xiao, R.; Cheng, M.; Zhang, C.; Xiong, W.; Lai, C.; Yang, Y.; Wang, W.; Yi, H.; Li, B. *J. Hazard. Mater.* **2019,** *380,* 120815. doi:10.1016/j.jhazmat.2019.120815
154. Ji, H.; Du, P.; Zhao, D.; Li, S.; Sun, F.; Duin, E. C.; Liu, W. *Appl. Catal., B* **2020,** *263,* 118357. doi:10.1016/j.apcatb.2019.118357
155. Balarak, D.; Mengelizadeh, N.; Rajiv, P.; Chandrika, K. *Environ. Sci. Pollut. Res.* **2021,** *28,* 49743–49754. doi:10.1007/s11356-021-13525-1
156. Qiao, D.; Li, Z.; Duan, J.; He, X. *Chem. Eng. J.* **2020,** *400,* 125952. doi:10.1016/j.cej.2020.125952
157. Kumar, S.; Karfa, P.; Majhi, K. C.; Madhuri, R. *Mater. Sci. Eng., C* **2020,** *111,* 110777. doi:10.1016/j.msec.2020.110777
158. Vasseghian, Y.; Sezgin, D.; Nguyen, D. C.; Hoang, H. Y.; Yilmaz, M. S. *Chemosphere* **2023,** *322,* 138243. doi:10.1016/j.chemosphere.2023.138243
159. Raja, A.; Rajasekaran, P.; Selvakumar, K.; Arunpandian, M.; Kaviyarasu, K.; Asath Bahadur, S.; Swaminathan, M. *Sep. Purif. Technol.* **2020,** *233,* 115996. doi:10.1016/j.seppur.2019.115996
160. Xu, M.; Wang, Y.; Ha, E.; Zhang, H.; Li, C. *Chemosphere* **2021,** *265,* 129013. doi:10.1016/j.chemosphere.2020.129013
161. Sodeinde, K. O.; Olusanya, S. O.; Lawal, O. S.; Sriariyanun, M.; Adediran, A. A. *Sci. Rep.* **2022,** *12,* 17054. doi:10.1038/s41598-022-21266-5
162. Wang, J.; Zang, L.; Wang, L.; Tian, Y.; Yang, Z.; Yue, Y.; Sun, L. *J. Environ. Chem. Eng.* **2022,** *10,* 108259. doi:10.1016/j.jece.2022.108259
163. Dal Conti-Lampert, A.; Testolin, R. C.; Somensi, C. A.; Almerindo, G. I.; Wagner, T. M.; Gerlach, O. M. S.; Sanches-Simões, E.; Ariente-Neto, R.; González, S. Y. G.; Radetski, C. M. *J. Environ. Sci. Health, Part A: Toxic/Hazard. Subst. Environ. Eng.* **2022,** *57,* 987–996. doi:10.1080/10934529.2022.2135343
164. Mahalingam, S.; Neelan, Y. D.; Bakthavatchalam, S.; Al-Humaid, L. A.; Al- Dahmash, N. D.; Santhanam, H.; Yang, T.-Y.; Hossain, N.; Park, S. H.; Kim, J. *ACS Omega* **2023,** *8,* 32817–32827. doi:10.1021/acsomega.3c03883
165. Kar, S.; Pal, T.; Ghosh, S. *ACS Appl. Nano Mater.* **2024,** *7,* 6516–6524. doi:10.1021/acsanm.4c00282
166. Zhu, W.; Liu, J.; Yu, S.; Zhou, Y.; Yan, X. *J. Hazard. Mater.* **2016,** *318,* 407–416. doi:10.1016/j.jhazmat.2016.06.066
167. Quyen, V. T.; Kim, J.; Park, P.-M.; Huong, P. T.; Viet, N. M.; Thang, P. Q. *J. Environ. Chem. Eng.* **2021,** *9,* 104737. doi:10.1016/j.jece.2020.104737
168. Hu, L.; Wang, Z.; Shi, Y.; Liu, C.; Hou, Y.; Bi, J.; Wu, L. *J. Environ. Chem. Eng.* **2022,** *10,* 108738. doi:10.1016/j.jece.2022.108738

License and Terms

This is an open access article licensed under the terms of the Beilstein-Institut Open Access License Agreement (https://www.beilstein-journals.org/bjnano/terms), which is identical to the Creative Commons Attribution 4.0 International License (https://creativecommons.org/licenses/by/4.0). The reuse of material under this license requires that the author(s), source and license are credited. Third-party material in this article could be subject to other licenses (typically indicated in the credit line), and in this case, users are required to obtain permission from the license holder to reuse the material.

The definitive version of this article is the electronic one which can be found at:
https://doi.org/10.3762/bjnano.16.21